

TALLINN UNIVERSITY OF TECHNOLOGY
DOCTORAL THESIS
4/2020

Solid-State Electrolytes for Fluoride-ion Batteries

PALANIVEL MOLAIYAN



TALLINN UNIVERSITY OF TECHNOLOGY

School of Science

School of Information Technologies

Department of Health Technologies

This dissertation was accepted for the defense of the degree 11/07/2019

Supervisor: Dr. Raiker Witter, PhD

Co-Supervisor: Lead Research Scientist Ago Samoson
Department of Health Technologies
Tallinn University of Technology
Tallinn, Estonia

Opponents: Docent Tao Hu
Faculty of Technology
University of Oulu
Oulu, Finland

Associate Professor Martin Kirkengen
Faculty of Mathematics and Natural Sciences
University of Oslo
Oslo, Norway

Defense of the thesis: 02/03/2020, Tallinn

Declaration:

Hereby I declare that this doctoral thesis, my original investigation, and achievement, submitted for the doctoral degree at Tallinn University of Technology has not been submitted for doctoral or equivalent academic degree.

Palanivel Molaiyan

.....
signature



Copyright: Palanivel Molaiyan, 2020

ISSN 2585-6898 (publication)

ISBN 978-9949-83-529-4 (publication)

ISSN 2585-6901 (PDF)

ISBN 978-9949-83-530-0 (PDF)

TALLINNA TEHNIKAÜLIKOOL
DOKTORITÖÖ
4/2020

Tahked elektrolüüdid fluoriidioon akudele

PALANIVEL MOLAIYAN



Contents

List of Publications	6
Author's contribution to the publications	7
Abbreviations	8
Introduction	9
1 Literature Review	11
1.1 All-solid-state batteries – literature survey	11
1.1.1 Definitions and basic concepts.....	11
1.1.2 Cell reactions: theoretical cell potential thermodynamic considerations	11
1.1.3 Theoretical capacity	12
1.2 Secondary (rechargeable) batteries.....	13
1.2.1 Lithium-ion batteries (LIBs)	14
1.2.2 Chloride-ion batteries (CIBs)	14
1.2.3 Mg batteries (MIBs)	15
1.2.4 Sodium-ion batteries (SIBs).....	15
1.3 Developing the future battery	16
1.3.1 Fluoride-ion batteries (FIBs).....	16
1.4 Summary of literature overview and aim of the study	17
2 Experimental	19
2.1 Materials	19
2.2 Solid-state synthesis method	19
2.3 Characterization methods.....	20
2.4 Direct and <i>in-situ</i> testing	22
3 Results and Discussion	23
3.1 Solid-state fluoride-type electrolytes.....	23
3.2 Vapor pressure-treated and ball-milled CaF ₂ electrolyte [I]	25
3.2.1 Structural studies of CaF ₂	25
3.2.2 Morphology studies for CaF ₂	26
3.2.3 Ionic conductivity studies for CaF ₂	27
3.2.4 Cell preparation.....	28
3.3 High-energy ball-milling synthesis for Sm _{1-x} Ca _x F _{3-x} (0 ≤ x ≤ 0.15) [II]	28
3.3.1 Structural studies of Sm _{0.95} Ca _{0.05} F _{2.95}	28
3.3.2 Morphology studies for Sm _{0.95} Ca _{0.05} F _{2.95}	29
3.3.3 Ionic conductivity studies for Sm _{0.95} Ca _{0.05} F _{2.95}	30
3.4 Pb _{1-x} Sn _x F ₂ (0.4 ≤ x ≤ 0.6) solid-solutions [III].....	31
3.4.1 Structural studies for Pb _{1-x} Sn _x F ₂ (x = 0.40 - 0.60).....	32
3.4.2 Morphology and chemical composition for Pb _{1-x} Sn _x F ₂ (x = 0.45)	32
3.4.3 Ionic conductivities for ball-milled Pb _{1-x} Sn _x F ₂ (x = 0.40 - 0.60) electrolytes	33
3.5 Preparatory and unpublished experiments, theoretical considerations	35
3.5.1 Rare-earth solid-state electrolytes (La _{1-x} Ba _x F _{3-x})	35
3.5.2 Humidified CaF ₂ ball-milled electrolytes	36
3.5.3 Ca _x Sm _{1-x} F _{3-x} (0 ≤ x ≤ 0.15) solid-solutions	37
3.5.4 Usage of Pb in FIB.....	38

Conclusions	39
References	43
Acknowledgments.....	51
Abstract	52
Lühikokkuvõte	53
Appendix	55
Curriculum vitae.....	83
Elulookirjeldus.....	84
Original publications	85

List of Publications

The list of author's publications based on the thesis has been prepared:

- I **P. Molaiyan** and R. Witter; Surface defect-enhanced conductivity of calcium fluoride for electrochemical applications. *Material Design & Processing Communications*. 2019, vol. 1, Issue no. 4, August 2019. e44, <https://doi.org/10.1002/mdp2.44>.
- II **P. Molaiyan** and R. Witter; Mechanochemical synthesis of solid-state electrolyte $\text{Sm}_{1-x}\text{Ca}_x\text{F}_{3-x}$ for batteries and other electrochemical devices. *Materials Letters*. 2019, vol. 244, pp. 22–26, <https://doi.org/10.1016/j.jelechem.2019.04.063>.
- III **P. Molaiyan** and R. Witter; Crystal phase and surface defect driven synthesis of $\text{Pb}_{1-x}\text{Sn}_x\text{F}_2$ solid solution electrolyte for fluoride ion batteries. *Journal of Electroanalytical Chemistry*. 2019, vol. 845, pp. 154–159, <https://doi.org/10.1016/j.matlet.2019.02.034>.

The Copies of these articles (I-III) are included in Appendix.

Author's contribution to the publications

The author's contribution to the papers in this thesis has been as follows:

- I The preparation of CaF_2 samples via vapor pressure exposure and subsequent high-energy ball-milling. The samples were characterized by structural and morphological methods (XRD, NMR, EPR, XPS, & SEM), electrochemical impedance spectroscopy (EIS), and battery cycling. The author played a primary role in sample preparation, testing, writing, conducting discussions, and contributing to the project's core idea.
- II The preparation of $\text{Sm}_{1-x}\text{Ca}_x\text{F}_{3-x}$ ($0 \leq x \leq 0.15$) solid solutions with different stoichiometric ratios was carried out via high-energy ball-milling. Various analytical methods were applied to characterize the synthesized electrolytes. The author's role was essential in sample preparation and testing, writing, and result interpretation.
- III The samples of $\text{Pb}_{1-x}\text{Sn}_x\text{F}_2$ ($0.4 \leq x \leq 0.6$) solid electrolyte were synthesized using high-energy ball-milling. The samples were examined by structural, morphological, and electrochemical studies. A significant role in sample preparation and testing, writing, and data interpretation was conducted by the author.

Abbreviations

AIB	Aluminum-ion batteries
BSE	Backscattered electrons
BM	Ball-milled
CIB	Chloride-ion batteries & Calcium-ion batteries
CL	Cathodoluminescence
CPE	Constant phase element
EPR	Electron paramagnetic resonance
EIS	Electrochemical impedance spectroscopy
EBSD	Electron backscatter diffraction
EV	Electric vehicles
EAL	Effective attenuate lengths
emf	Electromotive force
FESEM	Field emission scanning electron microscopy
FWHM	Full-width half maximum
FIB	Fluoride-ion batteries
HT	High-temperature
HEV	Heavy electric vehicles
HRTEM	High-resolution transmission electron microscopy
KIB	Potassium-ion batteries
LIB	Lithium-ion batteries
MAS	Magic angle spinning
MIB	Magnesium-ion batteries
NIB	Sodium-ion batteries
NMR	Nuclear magnetic resonance
Ni-MH	Nickel-metal Hydride
Ni-Cd	Nickel-cadmium
OCV	Open circuit voltage
OCP	Open circuit potential
PVdF	Polyvinylidene fluoride
PXRD	Powder X-ray diffraction
rpm	Rotation per minute
RT	Room-temperature at 25 °C
SM	Sintered material
SEM	Scanning electron microscopy
SHE	Standard hydrogen electrode
XRD	X-ray diffraction
XPS	X-ray photon spectroscopy

Introduction

The cell, principal component of a battery, is designed to store electrical energy in the form of chemical energy conversion through the electrochemical reactions at the anode and cathode, separated by an electrolyte. The electrolyte has to block electrons, which then follow potential difference through external load while ions migrate within electrolyte from anode to cathode or vice versa, depending on the sign of the charge they carry. The performance of the electrodes, electrolyte, reversible reaction chemistry, and cell engineering all determine how well a battery can be used. Li-ion batteries have changed, if not revolutionized, our life already in many ways. Nevertheless, urgent demand for 'pollution-reduced energy,' cost considerations, and numerous high-performance applications, in both mobile and grid context, keep the improvement of batteries at the forefront of academic research. Although the present-day industrial agenda has set the focus on Li-technology, there is strong motivation to develop next-generation solid-state alternatives. Prevalent battery systems, characteristic to lithium-ion design, are called 'wet' batteries, since the ion carrier, or electrolyte, is a liquid, gel or polymer.

Solid-state batteries can be, in principle, considered superior as they may overcome several of the limitations that exist in today's wet batteries [1]. They are safer due to non-volatile and solid components replacing flammable liquids or gels. Most notably, the solid-state approach provides the possibility to increase the energy and power density of the cells that we can use our devices for a longer time and charge them faster. 'All-solid-state' components apply in multiple form factors from the ultra-small to the extensive applications. Presently ubiquitous Li-ion batteries present a compromise also in geopolitically. Since the start of Li-ion proliferation, considerable risks have evolved regarding the availability of necessary minerals and raw materials. Shifting towards the use of independent, much less risky, and more efficient natural resources is commendable in many contexts. Thus many battery researchers consider solid-state battery technology as a future of portable devices and electric vehicles. Numerous alternative battery approaches such as sodium [2], chlorine [3], magnesium [4], calcium [5], and aluminum-ion batteries [6] are currently under development. One little-studied alternative to "wet" Li technology is based on deployment of the fluoride ion as a charge carrier. Fluoride-ion battery (FIB) technology may possess high-energy densities over a wide range of operating temperatures [1]. Due to the number of possible materials' variations, they may offer improved safety features compared to Li-ion based battery (LIB) types.

Our assessment shows that fluoride-ion batteries (FIBs) possess an overall potential that merits investigations and testing [7]. There is principally a large variety of electrode combinations available for fluoride-ion battery incarnations; many offer higher gravimetric and volumetric densities than Li-ion, Zn-O, Li-S or Li-O. Materials can be selected for low-cost, their chemistry can be made robust, simpler, and less costly, with reduced-hazard, devices can be made biocompatible, can be designed with a low environmental footprint, and comply with higher safety standards. Despite considerable effort, the electrolyte conductivity has remained the main hurdle for the realization of F-ion energy storage [8].

Recent advances in nanotechnology have opened new perspectives when it comes to improving FIB-technology [7], in particular, ionic conductivity. In this research work, fluoride-ionic conductors were prepared extensively by means of high-energy ball-milling,

which is a cost-efficient, simple, and safe chemical syntheses technique. We aimed to extend the knowledge on fluorine-ionic conductors at higher conductivity levels and lower temperatures. For example, $\text{La}_{1-x}\text{Ba}_x\text{F}_{1-x}$ ($0 \leq x \leq 0.15$) electrolyte has been used for FIB [8]. Pure solid-state doping mechanisms have been in focus, as tysonite-type compounds (LaF_3 , SmF_3 , CeF_3 , etc.,) doped with fluorites (CaF_2 , BaF_2 , etc.,) or, vice versa, to introduce the vacancies/interstitials for increased F-ion mobility. In this work three basic types of solid solutions were investigated: CaF_2 [I], $\text{M}_{1-x}\text{X}_y\text{F}_{3-x}$ ($0 \leq x \leq 0.15$) X: Ca, M=Sm) [II], and $\text{Pb}_{1-x}\text{Sn}_x\text{F}_2$ ($0.4 \leq x \leq 0.6$) [III]. While the overall macroscopic conductivity (σ_{IS}) can be obtained from impedance spectroscopy (EIS), a significantly higher local bulk value $\sigma_{NMR} \gg \sigma_{IS}$, provided by NMR, indicates the domination of the resistance formed at a particle surface and grain boundary. Therefore, our focus was on crystallite surfaces and towards increasing their ion conductivity by means of the creation of additional defects in order to realize a principally high structural conduction. The influence of the morphological and surface chemical properties of the different fluoride-ionic conductors was investigated and optimized in order to find improved battery concoctions. The electrolytes were also validated *in situ*, in a working cell environment, partly in a joint Ph.D. research work [9-12].

This dissertation is based on three published articles and is composed of two main chapters. Chapter 1 contains a literature overview of secondary ion batteries, the basic working principles of a cell, and a description of advanced secondary ion battery systems. Towards the end, a summary of the literature, and the aim of this study is given. Chapter 2 describes the experimental details of the work, and the materials and characterization methods, and also discusses the results. Chapters 3, 4, & 5 present the results and discussion of the studied solid-state fluoride-ionic conductors such as humidified ball-milled CaF_2 , CaF_2 doped SmF_3 , and SnF_2 doped PbF_2 . Finally, the published works [I-III] are attached.

1 Literature Review

1.1 All-solid-state batteries – literature survey

Out of all currently available battery technologies that have been developed, low-temperature aqueous batteries have the most significant impact in terms of large-scale applications when maintenance, safety, reliability, and cost come together [13, 14]. The lead-acid batteries, which were invented in 1859 by French physicist Gaston Planté are still widely used due to the high surge current that is required by motor vehicle starters. However, any progress in performance, cost efficiency, safety, and environmental awareness creates new applications and propels further development [15-20]. The basic concepts and working principle of a typical battery will be discussed in the below section.

1.1.1 Definitions and basic concepts

Traditionally, an electrochemical cell is a chemical device that permits the conversion of chemical energy into electrical energy. A cell is composed of two half cells, each composed of electrodes that are separated by an electrolyte [21]. The conversion of the energy from chemical to electrical is made possible through electrochemical reactions called redox reactions, which take place simultaneously at both electrodes [22]. The cathode is the oxidizing electrode, which accepts the electrons from the external electric circuit and is reduced during the electrochemical discharge reaction. The anode is the reducing electrode, which supplies the electrons to the external circuit and is oxidized during the electrochemical reaction with a lower potential. The electrolyte is an ionic conductor shuttle between the ions from one electrode to the other electrode during the charging or discharging process. The typical electrolyte usually is a liquid solution or gel containing, e.g., salts. Solid-state batteries are solely composed of solid materials both for the electrolyte and the electrodes. Such a rigid configuration leads to meritable advantages if leakage or short-circuits of the cell could be avoided. However, severe challenges exist in their use, for instance, the lower ionic conductivity of the solid electrolyte and volumetric changes that are expected upon the cycling of the FIB, are a well-known impediment to all-solid-state battery systems [23, 24].

1.1.2 Cell reactions: theoretical cell potential thermodynamic considerations

The evaluation and calculation of the theoretical cell potential of a redox reaction is useful to assess and justify the choice of materials. The cell potential E is determined by the potential difference ΔE between the redox couples that are involved in each half-cell:

$$\Delta E = E_+ - E_- \quad (1)$$

where E_+ and E_- stand for the potentials of the positive and negative electrodes, respectively. The potential difference is referred to as electromotive force (emf), pertinent to a driving force and motion of electrons through the external circuit.

When the system is not in equilibrium (standard) state, the potential is given by the Nernst equation:

$$E = E_o - \frac{RT}{nF} \ln \frac{red}{ox} \quad (2)$$

where (ox) and (red) are the activities of the redox reactions, R stands for the gas constant, T is for the absolute temperature, and E_o the standard potential. n is the number of moles, and F stands for the Faraday constant ($F = 96,485 \text{ C}\cdot\text{mol}^{-1}$).

The standard potential of a cell, often referred to as Gibbs free energy ΔG , is related to the change of standard free energy ΔE :

$$\Delta G = -n F \Delta E \quad (3)$$

ΔG is representing the standard enthalpy change ΔH and standard entropy change ΔS via the equation:

$$\Delta G = \Delta H - T \Delta S \quad (4)$$

The values of ΔH and ΔS can be found in reference tables as provided by the thermodynamic data [25]. The experimental potentials sometimes differ from those that are calculated; the latter remains very useful when it comes to determining the highest number of perspective redox couples that could deliver the highest cell voltage. These thermodynamic considerations are also of interest when it comes to calculating the decomposition potential of some solid-state materials and their applications.

1.1.3 Theoretical capacity

The theoretical specific capacity (capacity per unit of mass, also referred to as gravimetric capacity) $Q_{th,m}$ ($\text{mA}\cdot\text{h}\cdot\text{g}^{-1}$) of active material can be calculated by the following equation:

$$Q_{Th,m} = \frac{n F}{3.6 \times M} \quad (5)$$

where n is the theoretical number of moles of the electron being exchanged, and M being the molar mass of the active material. The coefficient of 3.6 is used here to convert the capacity in Coulomb (C) to milliampere-hour ($\text{mA}\cdot\text{h}$). In a fluoride-ion battery, n is directly related to the expected change in the valence of the metal or metal fluoride. It is also possible to calculate the theoretical volumetric capacity $Q_{th,v}$ ($\text{mA}\cdot\text{h}\cdot\text{cm}^{-3}$) when knowing the volumetric mass density ρ ($\text{g}\cdot\text{cm}^{-3}$) of the active material:

$$Q_{Th,v} = Q_{Th,m} \times \rho \quad (6)$$

Materials comprising elements of low molar masses are naturally attractive candidates for FIBs. These calculations (involving specific energies) are useful to compare active materials and serve to demonstrate the attractiveness of FIBs, but they must be projected onto some degree of practical relevance for real-world devices. One of the crucial tasks is to optimize the amount of active material, and estimating the material costs can also be important.

The electrodes and electrolyte of the cell depend upon many factors:

- ❖ The anode and cathode (electrodes) need to be made of high capacity materials. The anode should release an electron at a fast rate, and the cathode should accept it at the highest rate possible.
- ❖ The anode and cathode should not corrode or chemically react with the electrolyte.
- ❖ The anode and cathode should have a high surface area to volume ratio in order to enable a large reaction surface, which involves a significant number of reacting sites for high currents.
- ❖ The solid-state electrolytes should be chemically stable during the operation of the cell and should have high ionic conductivity in order to minimize any energy loss.
- ❖ For a rechargeable battery, the reactions (charge/discharge) must be reversible. The energy storage and release cycles need to remain steady over many repetitions while providing high cell potential and current.

- ❖ The anode, electrolyte, and cathode materials should be affordable. The entire battery should have an acceptable ecological footprint.

Batteries can be divided into two major classes: primary and secondary batteries [22]. Primary batteries such as zinc-carbon, alkaline manganese, and lithium manganese dioxide cannot be recharged (fully charged) and must be replaced after reactants are depleted. Whereas the secondary batteries, for example, lead-acid, Ni-Cd, Ni-MH, and lithium-ion, are rechargeable and can bring reactants back to their charged state [26]. In the upcoming section, a detailed description of the chemistry and development of rechargeable secondary ion batteries will be presented [3][27].

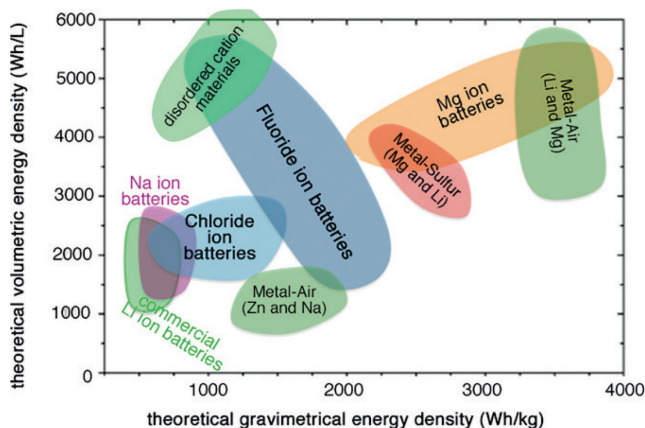


Figure 1. An overview of various future battery technologies is depicted. From bottom left to upper right these are: commercial Li-ion batteries, sodium-ion batteries, chloride-ion batteries, Zn-air batteries, Na-air batteries, fluoride-ion batteries, disordered cation materials (such as $\text{Li}_2\text{VO}_2\text{F}$), Metal-Sulphur batteries (with Mg and Li as the anode), magnesium-ion batteries, and (top right) lithium-air and magnesium-air batteries. Reproduced from ref. [3] with permission from John Wiley and Sons Publishing Group.

1.2 Secondary (rechargeable) batteries

Secondary batteries, simply known as rechargeable batteries, can be electrically recharged back to their original condition by means of a driving voltage inducing an electric current in the opposite direction of the discharge current [22]. The charge transfer ions can be distinguished into cationic shuttles (such as Li^+ , Na^+ , and Mg^{2+}), and anionic shuttles (such as Cl^- and F^-), providing a wide variety of different battery types [28]. Related to this, Na-ion batteries (NIBs) [29], Mg-ion batteries [30], chloride-ion batteries (CIBs) [31,32], fluoride-ion batteries (FIBs) [1][33], potassium-ion batteries (KIBs) [34], and aluminum-ion batteries (AIBs) [35] have been introduced. Currently, the most utilized battery systems are LIBs, as they provide a good overall compromise for various mobile and industrial applications.

The combination of highly reactive metals with high electronegative anions is a starting point in the search for a new kind of battery with the high energy power density and cell potential. Most of the high-voltage ionic shuttles that have been investigated (Li, Na, and Mg) are located at the negative end of the standard electrode potential series [36]. The positive end, which comprises elements such as fluorine and chlorine, has not been so thoroughly addressed.

1.2.1 Lithium-ion batteries (LIBs)

The first attempt to develop rechargeable lithium-ion batteries (LIBs) started in the 1970s. LIBs possess a high energy density, which comes from a high working potential and functional capacity [37],[38]. The early work of John Goodenough unveiled LiCoO₂ electrode materials, Rachid Yazami developed the graphite materials for higher energy density levels. LIB-s were first commercialized by Sony in the early 1990s, using organic liquid electrolytes [37]. Since then, researchers have undergone great efforts to improve performance and properties [39]. Notable initiators are TESLA Motors and the Joint Centre for Energy Storage Research hub, which was awarded \$120 million by the US Department of Energy in 2012. Companies like BOSCH decided to introduce annual investment into electro-mobility of several hundred million Euro per year [44]. Related importance has further increased; China is pushing for a target of 20% of all vehicle production and sales in new energy vehicles (NEV) by 2025, pushing the world market. It is predicted that by 2021, 65% of all Li-Ion batteries are being produced in China. Different forms of Li-ion batteries are available, which are based on various cathode, anode, and electrolyte materials [40]. At present, lithium-ion batteries are the most advanced batteries on the market for automotive (apart starters) and portable electronic devices [41, 42]. The improvement, both in gravimetric and volumetric densities of the various types of commercial and secondary ion battery systems, is shown in Figure 1.

For a lithium-ion battery (LIB), a practical energy density can be up to 200-400 W·h·kg⁻¹ [43-47]. Academic results from Japan show Li-air applicability up to 400-900 W·h·kg⁻¹. Today, commercial LIBs still rely on the reversible insertion of lithium ions into the layered structure of host electrodes, but LiCoO₂ is now replaced by the safer LiFePO₄ and other materials such as NMC [17][46]. During the charging of the cell, the Li-ion and electron flux is directed towards the negative electrode (anode), and during discharge, they are directed towards the positive electrode (cathode) [48]. For a typically layered oxide cathode and a carbon anode, the overall discharge exchange reaction can be written down as



where *M* is the transition metal; however, the main concern is the limited availability of lithium and transition metal resources. Indeed, lithium is only present at trace levels in the Earth's crust and in the sea, and its extraction is costly [42]. Transition metals like Co are even more critical related to costs and availability. Worldwide raw material reserves cannot meet the implementation of lithium-ion batteries for the automotive industry and portable electronics in forthcoming years; Lithium will last a maximum of three decades. In mitigation, though, it is believed that the establishment of proper recycling networks could provide a solution to demand-related problems [15]. One main concern in this area involves potential price increases in lithium-based materials. Therefore, it is crucial to develop an alternative – “Post-Lithium” – battery systems. During the last few years, the considerable worldwide effort has been undertaken to proceed beyond the present Li-ion level technology, both in the private and public sectors.

1.2.2 Chloride-ion batteries (CIBs)

Metal chloride systems show a substantial Gibbs free energy change, which yields a high electromotive force during phase transformation, i.e., a chloride-ion transfer [31]. The metal/chloride systems show theoretical energy densities, which are higher than can be achieved by the current Li-ion battery (LIB). Moreover, this battery type can be built from abundant material resources, including various types of metals (such as Li, Na, Mg,

Ca, and Ce) or their chlorides as active material in the electrode. The development of chloride electrolytes with high ion conductivity and stability remains a key challenge [31]. Some of the stable inorganic compounds such as PbCl_2 , SnCl_2 , and LaOCl show rapid chloride transfer levels at very high temperatures [49], and even higher melting points than those of some metal chlorides [50]. The best metal chloride electrolyte - CsSnCl_3 (cubic) - has a high ionic conductivity of $1 \text{ m}\cdot\text{S}\cdot\text{cm}^{-1}$ at about $100 \text{ }^\circ\text{C}$ [51], but its electrochemical stability needs to be investigated and improved [52].

1.2.3 Mg batteries (MIBs)

Magnesium-ion batteries have a higher potential and higher energy densities due to the ability of each Mg^{2+} ion to store two electrons [53]. However, there is a significant issue in terms of finding a suitable cathode due to the sizeable electrostatic interaction between the host anions and Mg^{2+} . It limits the diffusion rate critically and lowers electrochemical performance [54]. Mg as an anode material has a high theoretical volumetric capacity of $3,832 \text{ mA}\cdot\text{h}\cdot\text{cm}^{-3}$ when compared to lithium (Li : $2,062 \text{ mA}\cdot\text{h}\cdot\text{cm}^{-3}$), and its electrochemical potential is -2.37 V versus SHE (Standard Hydrogen Electrode) [54]. Mg is environmentally benign, safe to handle, and in comparison with lithium comes at a lower cost. Sulfur or its composites can be used as the cathode [55]. Attractively, Mg does not form dendrites when electrodeposited [56]. The significant challenges of an Mg battery: (a) the need to develop Mg^{2+} ion-containing non-aqueous liquid electrolytes with high ionic conductivity levels at room temperature; and (b) a dielectric constant for reversible deposition and the dissolution of magnesium. Bian et al. [57] reported the development of thiolate based electrolytes, which showed oxidative stability and a voltage of 2.5 V on the platinum electrode with a reversible Mg^{2+} -ion insertion/extraction from/into a Mo_6S_8 -electrode. This system delivered a specific capacity of $40 \text{ mA}\cdot\text{h}\cdot\text{g}^{-1}$ when tested at 0.38 C and $45 \text{ mA}\cdot\text{h}\cdot\text{g}^{-1}$ at a 0.095 C current rate respectively.

1.2.4 Sodium-ion batteries (SIBs)

Sodium-ion batteries (Na-ion) are considered as possibly being a much cheaper, safer, and more sustainable alternative to Li-ion technology [58]. There is over a thousand times more sodium than lithium in the Earth's crust. Additionally, sodium can be readily extracted from seawater [59]. Aluminum can be used as the current collector at the anode, unlike Li-ion batteries, which require more expensive copper foils. Another considerable advantage derives from the Sodium as a monovalent-ion-forming alkali metal with very similar chemistry to Li-ion. SIBs have a high specific capacity of $1,165 \text{ mA}\cdot\text{h}\cdot\text{g}^{-1}$ with a negative reduction potential of -2.71 V versus SHE. The size of Na^+ (with a radius of $\sim 1.02 \text{ \AA}$) is considerably larger than for Li^+ (with a radius of $\sim 0.76 \text{ \AA}$), and most materials do not have a sufficiently sizeable interstitial space to host Na^+ ions within the electrodes [59]. It is observed that it is a considerable challenge when it comes to the development of appropriate electrode materials being able to host Na^+ with high levels of capacity and rapid diffusion kinetics. For anode materials of SIBs, various carbon materials can be used with different structures [60, 61], and morphologies [62]. A reversible capacity of $250\text{-}300 \text{ mA}\cdot\text{h}\cdot\text{g}^{-1}$ at a voltage range of $0\text{-}3 \text{ V}$ has usually been achieved. Alloy based anodes for SIBs, such as Sn ($\text{Na}_{15}\text{Sn}_4$, $847 \text{ mA}\cdot\text{h}\cdot\text{g}^{-1}$) [63], and Sb (Na_3Sb , $660 \text{ mA}\cdot\text{h}\cdot\text{g}^{-1}$) have attracted considerable interest due to their appropriate potential regarding Na^+ insertion and high theoretical capacities [64]. In terms of the cathode material, usage of $\text{Na}_{1.25}\text{V}_3\text{O}_8$ nano-wires [65, 66] provides an increased electrode-electrolyte contact area and a shorter Na-ion diffusion path, also preventing self-aggregation. Sulfates have been considered as cathode candidates for SIBs:

$\text{Na}_2\text{M}(\text{SO}_4)\cdot 4\text{H}_2\text{O}$ (M = Mg, Fe, Co, or Ni) and their dehydrated derivatives, $\text{Na}_2\text{M}(\text{SO}_4)_2$ (M = Co or Fe) which showed electrochemical activity at a potential of 3.3-3.4 V versus Na/Na^+ [67]. Overall, SIBs are a strong contender as an alternative to LIB. Even so, the higher-rated energy cathode materials need to be optimized before they can rightly be considered [68].

Apart from that, other rechargeable secondary-ion batteries such as potassium-ion batteries [69], calcium-ion batteries [70], aluminum-ion batteries (AIBs) [71] and zinc-ion batteries [72] also have high theoretical energy density levels and are under investigation. However, the development of these batteries is demanding due to problems in finding suitable electrode and electrolyte materials.

1.3 Developing the future battery

Many future rechargeable secondary ion battery options are presented graphically in Figure 1. Any research and development strategy should consider the following aspects:

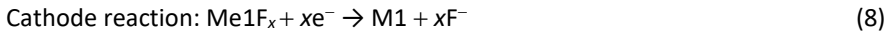
- ❖ For a rechargeable battery, energy storage and cycles need to be repeated many times, and the reactions must be reversible. Any reversible electrochemical reaction with a proper cell potential may be used as a rechargeable battery. The synthesis of high energetic inexpensive electrode materials should be developed.
- ❖ Establishment of suitably stable electrolytes, with suitable solubility for the salt of the shuttling ion with high ionic conductivity at ambient temperature, is one of the most significant challenges for current battery systems.
- ❖ The electrodes should not corrode by dissociating electrode and electrolyte compositions.
- ❖ The design of practical cells should ensure that the electrode reactions are separated so that an electron that is released/absorbed from the anode/cathode can quickly jump to/from the current collectors to feed an external load efficiently.

1.3.1 Fluoride-ion batteries (FIBs)

In this section, we shall briefly characterize considerations which have led to the particular selection of the present dissertation work. In the periodic table, fluorine is the most electronegative element. It is very stable and has a sizeable electrochemical stability window. The chemistry of FIBs relies on the shuttle of the fluoride-ion (F^-) between metal and metal fluoride electrode through a fluoride-ion conducting electrolyte, as seen in Figure 2 [1]. These reactions are conversion reactions and do not rely on the insertion of F^- . Coupled with the massive change in free energy that is featured by the high electronegativity of the fluoride-ion, they offer outstanding theoretical energy densities. Values more than $1,500 \text{ W}\cdot\text{h}\cdot\text{kg}^{-1}$ or $5,000 \text{ W}\cdot\text{h}\cdot\text{L}^{-1}$ can be estimated for some suitable electrode material combinations [73]. The study of these electrochemical systems first started in the 1970s upon the development of fast fluoride conducting electrolytes. After that, in 2011, scientific publications demonstrated a proof of concept in terms of reversible fluoride cells [1], followed up by various publications [74-76]. Subsequently, the French National Research Agency (ANR) decided to support this system and focused on possible alternatives to Li-ion batteries [73]. The theoretical working principle of a FIB is illustrated as an example of a BiF_3/Mg system, see Figure 2. The discharge is accompanied by the oxidation of the anode, e.g., $\text{Mg} \rightarrow \text{MgF}_2$, which releases two electrons into the electric circuit. The electrons reduce the cathode

(consisting of a metal fluoride) into the corresponding metal, like $\text{BiF}_3 \rightarrow \text{Bi}$. Charge neutrality is assured by F^- . In theory, no fundamental property renders fluoride-ion batteries inherently more dangerous than other state-of-the-art batteries if appropriate safety measures are applied. However, such design principles remain to be established by future development, and therefore, no general statement can presently be made regarding the safety levels. Some fluorides are extraordinarily stable and even biocompatible like CaF_2 .

The electrochemical reactions of a FIB (discharging):



In this, Me_1F_x is the metal fluoride being used as a cathode, M_1 is the metal being used as an anode, and n is the number of fluoride ions. It has been reported that the FIB battery was operated at 150°C by using a solid-state electrolyte of a $\text{LaF}_3/\text{BaF}_2$ composite [76, 77], with a fluoride conductivity of $0.2 \text{ m}\cdot\text{S}\cdot\text{cm}^{-1}$ at $\sim 150^\circ\text{C}$. The improvement of ionic conductivity, as well as the electrochemical stability of the electrolyte, are the most critical challenges for the development of any fluoride-ion battery.

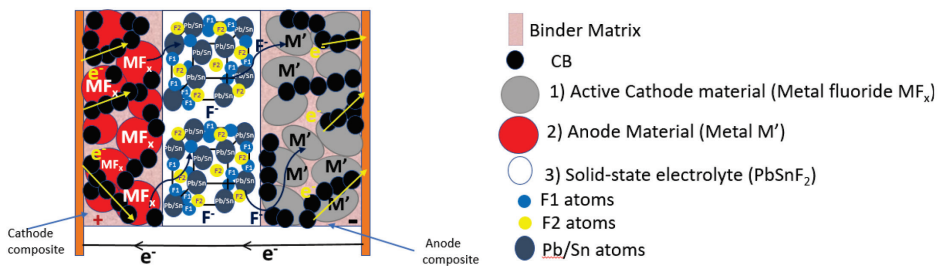


Figure 2. The schematic of the fluoride-ion battery is shown in discharging process. 1) red color – Active cathode material (consists of metal fluoride, partially mixed with CB and binder), 2) light grey color– anode material (consists of metal, CB, binder), e^- – electron, pink color – binder matrix, and black color – carbon black (CB). 3) white color represents F^- fluoride ion (solid-state fluoride electrolyte ex. PbSnF_2), grey color – Pb/Sn atoms, yellow color – F2 atoms, blue color – F1 atoms, and orange color – current collector.

1.4 Summary of literature overview and aim of the study

Presently, the functional capacity of tested FIB compositions is considerably lower than their theoretical values, and it fades rapidly during cycling. The main reasons for this may be the limited ionic conductivity of the solid electrolyte and not an appropriate choice of electrodes. However, the synthesis of solid electrolytes is facing a significant degree of challenge when it comes to finding proper materials [18]. New solid electrolytes such as LaF_3 -mixed with BaF_2 have recently been reported [78, 79], exhibiting high levels of ionic conductivity at higher temperatures; more recently a new secondary battery based on a fluoride shuttle has been reported with $\text{La}_{0.9}\text{Ba}_{0.1}\text{F}_{2.9}$ as a solid-state electrolyte [80][77]. The fluoride-ion conductor combinations of rare-earth ($\text{R} = \text{La-Lu, Sm}$) and alkaline-earth

(M = Ca, Sr, Ba) metal fluorides have been explored to form $R_{1-x}M_xF_{3-x}$ with the stabilization of fluoride vacancies [81, 82]. The different ionic radii of the alkaline earth cations ($Ba^{2+} > Sr^{2+} > Ca^{2+}$), as well as the rare earth cations ($La^{3+} > Lu^{3+}$) influence the local environments of fluoride ions and, consequently, their mobility [83, 84]. Further, a recent report describes a high-temperature synthesis of SmF_3 , showing a conductivity jump at a temperature of 500 °C, which corresponds to the orthorhombic (YF_3) or trigonal (LaF_3) phase transition [85] with a tysonite-type network providing a higher level of conductivity. At room temperature, the ionic conductivity ($Sm_{0.94}Ca_{0.06}F_{2.94}$) for the best samples that have been reported is around $10^{-4} \text{ S}\cdot\text{cm}^{-1}$ [86].

The objectives behind the present doctoral thesis were settled basing them on a literature overview of advanced battery systems, augmented by future needs and potential constraints. The overall goal is to develop fluoride-ionic conductors that exhibit higher conductivities, which are mechanically rigid to the extent of self-supporting design and suppression of dendrite growth.

We aimed to gain a fundamental understanding of the ion transportation in select, yet representative solid-state fluoride-ionic conductors and shall explore the structure-property relationships for FIB applications. Stable synthesis routes needed to be identified for the fabrication of the fluoride materials which feature both, high cation mobility (at least good enough to initiate systematic studies on working configurations) and mechanically self-sustained assembly behavior. A literature survey led to the conclusion that fluorides which can be used as solid electrolytes are either alkaline-earth fluorides (with a fluorite-type structure, e.g., CaF_2), rare-earth fluorides (with a tysonite-type structure, e.g., LaF_3 , SmF_3) or lead-based fluorides (e.g., PbF_2 or $PbSnF_4$). The latter have very high F^- conductivity but, unfortunately, are not compatible with many battery applications due to their limited electrochemical stability. The solid-state electrolyte combinations of rare-earth metal fluorides ($R = La-Lu, Sm$) and alkaline-earth metal fluorides ($M = Ca, Sr, Ba$) have been explored to form $R_{1-x}M_xF_{3-x}$ with the stabilization of fluoride vacancies [34]. The different ionic radii of the alkaline earth cations ($Ba^{2+} > Sr^{2+} > Ca^{2+}$) as well as the rare earth cations ($La^{3+} > Lu^{3+}$) serve to influence the local environments of fluoride ions and, consequently, their mobility. Capitalizing on these considerations, we synthesized and investigated different classes of solid-state fluoride electrolytes.

2 Experimental

The conducted experiments and general procedures with applied materials, being used for the preparation of solid-state battery components, their characterization (analytical methods), cell assembly, etc., are listed and explained here.

2.1 Materials

In this work, we have used various chemicals supplied by Sigma Aldrich and Alfa Aesar; details are given in Table 1.

Table 1. Description of materials and chemicals.

Chemicals	Formula	Purity	Supplier
Bismuth fluoride	BiF ₃	99.5%	Sigma Aldrich
Calcium fluoride	CaF ₂	99.5%	Alfa Aesar
Cerium (III) fluoride	CeF ₃	99.9%	Alfa Aesar
Lead (II) fluoride	PbF ₂	99%	Sigma Aldrich
Lead (II) fluoride	PbF ₂	99%	Sigma Aldrich
Magnesium fluoride	MgF ₂	99%	Sigma Aldrich
Sodium fluoride	NaF	99.5%	Sigma Aldrich
Samarium fluoride	SmF ₃	99.9%	Alfa Aesar
Tin (II) fluoride	SnF ₂	97.5%	Alfa Aesar
Bismuth powder	Bi	99%	Alfa Aesar
Copper powder	Cu	99.7%	Alfa Aesar
Iron powder	Fe	99.5%	Alfa Aesar
Lead powder	Pb	99%	Alfa Aesar
Magnesium powder	Mg	99%	Alfa Aesar
Potassium chloride	KCl	99.5%	Sigma Aldrich
Carbon black	CB	99.9%	Alfa Aesar
Poly (vinylidene fluoride)	(-CH ₂ CF ₂ -) _n	99%	Alfa Aesar

2.2 Solid-state synthesis method

In this thesis, the high-energy ball-milling (BM) method was selected for the preparation of solid-state electrode composites and electrolytes. Generally, solid-state reactions may be more natural and chemically reactive in terms of the starting materials, which may contain ions that can diffuse quickly [87]. The critical factors promoting a solid-state reaction are these: choice of precursors, mixing method, container, heat conditions, ball-to-powder ratio, rotation speed, and time.

Solid-state reactions generally occur at high temperatures, but in favorable cases, reactions can be carried out merely by grinding together the reagents [88]. High-energy milling is possible in planetary-type ball mills, which are rotated at very high speeds. The reagents are reduced to nanometer size with the introduction of mechanically-induced crystal defects. Nevertheless, mechano-chemical synthesis may become an essential method for the synthesis of new nano-materials and nano-composite materials as it is a relatively inexpensive and energy-efficient method, which, as a rule, allows to avoid high temperatures. Importantly, it is also easily scaled-up to industrial relevance and is rapidly gaining popularity [89]. The ball-milling process is illustrated in Figure 3.

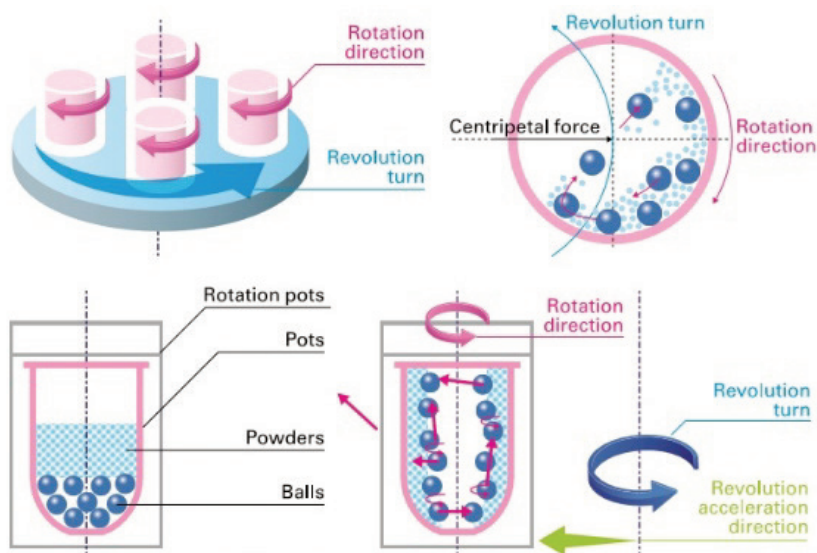


Figure 3. The kinetics of planetary ball-milling is sketched. The milling vial is rotated around itself, and the supporting disc, on which the vial is placed, also rotates, exerting a centrifugal force on the vial and its contents. The balls (shown as blue spheres in the figure) follow approximately the path as shown by the dashed lines before hitting the walls of the vial and shocking the powder (shown as cyan dots). The vials have to be chosen appropriately and cleaned to avoid any contamination. The schematics by Nagao System, Inc.

The advantages for the mechanochemical synthesis of materials are as follows: (i) the large-scale synthesis of homogeneous materials can be quickly realized, which is essential for the consistency of the battery materials; (ii) reliable operation to ensure reproducible results; and (iii) it is suitable for a variety of synthesis systems and for appealing to many practical areas of application due to its economy and easy replicability [90]. Based on this, we have prepared all of our samples with the use of a high-energy planetary-type device from the company of Tanchen powder, China [I-III]. It has a maximum speed of 800 rpm with four jars delivering an impact of between 100-125 g. Detailed syntheses and results are discussed in section 3.

2.3 Characterization methods

The analytical methods that were used for the characterization of fluoride-ionic conductors and FIB testing are summarized in Table 2. A detailed description of each method can be found in the section below and the experimental sections of [I-III].

X-ray diffraction (XRD) measurements were performed to identify the phase composition and crystal structure of synthesized electrolytes [I-III]. The cell parameters and average crystallite sizes were determined by performing profile matching refinements of the XRD patterns [I]. The refinement was done using Le Bail method with the FullProf software. In this work, all XRD measurements were carried out using Advance instrumentation (AXS Bruker D5005) with Cu K α radiation (λ_1 -1.54056 Å, λ_2 -1.54439 Å) with a variable slit. The measurements were carried out at the Centre for Materials Research, Tallinn University of Technology, Estonia. The morphology and particle size (SEM & FESEM) analysis was performed on ball-milled electrolytes [I-III]. The cross-section of the pellet was determined by FESEM analysis [I]. The EDX analysis

was carried on different electrolytes to identify the material compositions [II-III]. The microstructure of all samples was observed using a Field emissions scanning electron microscope (Ultra 55 FESEM from Carl Zeiss), which featured the GEMINI In-lens SE detector with an EDX detector. The measurements were carried out at the materials science department, Tallinn University of Technology, Estonia. High-resolution transmission electron microscope imaging (HRTEM) is useful for visualizing the crystallinity of samples in real space rather than in diffraction mode. FEI probe TitanG2 80-200 (HRTEM) was used for morphology and particle size distribution studies of fluoride electrolytes [II-III].

Table 2. Various methods used for the characterization of electrolytes and FIB.

Properties	Analytical method	Apparatus	Reference
Crystallite size, phase composition, crystal structure	XRD	AXS Bruker D5005	[I-III]
Morphology; cross-sectional images, elemental analysis	FESEM + EDS	Zeiss HR FESEM Ultra 55 with EDS	[I-III]
Chemical composition of the surface	XPS	XPS spectrometer - Thermo Fisher Scientific, East Grinstead, England	[I]
Morphology; crystallinity, particle size distribution	HRTEM	FEI Probe Titan G2 80-200 (HRTEM)	[II] & [III]
Local and defect structure, the diffusion coefficient	NMR	MAS NMR- 40KHz with Bruker spectrometer	[I-III]
The ionic conductivity, activation energy	EIS	Agilent 4192A LF impedance analyzer 5 Hz to 13 MHz	[I-III]
Charging and discharging, cycles, efficiency, specific capacity, etc.	Battery tester	Agilent Keysight N6705B DC power analyzer	[I-III]

X-ray photon spectroscopy (XPS) measurements were carried out using a K-Alpha+ XPS spectrometer (Thermo Fisher Scientific, East Grinstead, England), for data acquisition and processing the Thermo Advantage software was used [91]. All samples were analyzed applying a micro-focused, monochromatic Al K α X-ray source (30-400 μ m spot size). The spectra were fitted with one or more Voigt profiles. For sharp peaks and peaks that were evidenced by the peak shape, the binding energy uncertainty was around \pm 0.1 eV. In the case of weak peaks and no direct justification by the peak shape, the uncertainty was set to \pm 0.2 eV. The analyzer transmission function, Scofield sensitivity factors, and effective attenuation lengths (EALs) for photoelectrons were applied for quantification for the compounds that were analyzed. EALs were calculated using the standard TPP-2M formalism [92]. All spectra were referred to the C1s peak of hydrocarbon at 285.0 eV binding energy which was controlled using the well-known photoelectron peaks of metallic Cu, Ag, and Au [I].

All of the ionic conductivities of the electrolytes were determined by means of EIS measurement. Electrochemical impedance spectroscopy (EIS) is a technique for the characterization of electrochemical systems, applied for the study of coatings, batteries, fuel cells, and corrosion phenomena [93]. The experimental procedure involves a broad range of frequencies and can isolate influences of the governing physical and chemical phenomena at an applied potential. EIS can separate and quantify the sources of polarization by applying physically-sound equivalent circuit models wherein physiochemical processes occurring within the cell are represented by a network of resistors, capacitors, and inductors [93]. EIS measurements were carried out by using an Agilent 4192A LF impedance spectrum analyzer. The frequency range was between 13 MHz to 5 Hz, and the voltage amplitude was 10 mV.

2.4 Direct and *in-situ* testing

The electrolytes can be used and should perform in two contexts. The primary role is a blockage of electron flow from the cathode to the anode while transporting ions; secondary is an ion transport within the electrode matrix. The electrodes were composites of either metal powder (anode) or metal fluoride (cathode) and carbon black for electron conduction. PVdF was used to bind composites before compression. 10 mm diameter solid pellets were fabricated by pressing together layers of electrodes and an electrolyte in between. A 2-5 tons load to press the pellet using a desktop press (Across International), placed inside an argon-filled glove box, was used for compaction. The pressed pellet was positioned and sealed using a CR2032 coin cell case for electrochemical studies. The coin cell was tested using Agilent keysight technologies for battery charging and discharge cycling performance. Impedance measurements were performed on solid-state electrolyte pellets pressed with a 1-5 tons force for one minute and coated with gold which was sputtered on both sides to block ions from leaving electrodes. The thickness and diameter of the pellets were approximately 1 mm and 10 mm, respectively. The impedance spectra were recorded at different temperatures ranging from 25 °C to 100 °C [I-III].

3 Results and Discussion

3.1 Solid-state fluoride-type electrolytes

Inspired by previous studies and literature overview, we synthesized and investigated a range of three solid-state fluoride-ionic conductors for FIBs, each representing a different class of crystal structure. Firstly, we used alkaline earth CaF_2 , treated by vapor pressure before BM [I]. Secondly, we BM-synthesized two solid-solution varieties of electrolytes without any prior treatment of the samples, but at varied stoichiometric ratios: rare earth $\text{Sm}_{1-x}\text{Ca}_x\text{F}_{3-x}$ ($0 \leq x \leq 0.15$) [II] and lead-based $\text{Pb}_{1-x}\text{Sn}_x\text{F}_2$ ($x = 0.40 - 0.60$) [III].

For BM, the materials were placed into a silicon nitride vial (with an internal volume of 50 mL) which was sealed into vacuum-tight containers together with silicon nitride balls, keeping a ball-to-powder ratio of 18:1, and processed at 600 rpm for around eighteen hours (Table 3). The cells were fabricated by pressing together an anode composite (Metal powder) consists of binder (PVdF) and CB, a solid-state electrolyte, and a composite cathode material consists of binder (PVdF) and CB, solid-state electrolyte, respectively. The pressed battery pellet diameter was around 10 mm, which was sealed within an air-tight CR2032 coin cell case. The electrochemical *in-situ* cycling tests of the coin cells were carried out at RT using an Agilent Keysight N6705B DC power analyzer.

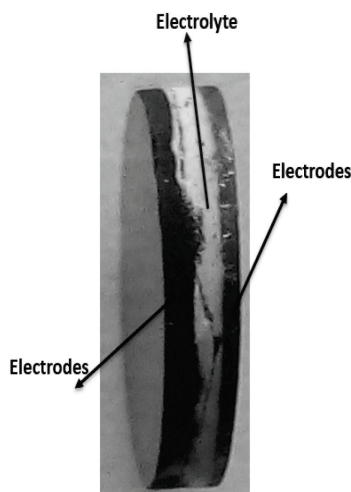


Figure 4. An optical view of solid FIB in the form of a pressed pellet.

The prepared electrolytes were examined by structural, morphological, and electrochemical studies, and the compounds were tested for fluoride-ion based battery application (Figure 4). The results have been published in peer-reviewed journals [I-III].

Table 3. A list of solid-state fluoride-ionic conductors and the results of ionic conductivity tests at ambient and higher temperatures are provided.

Solid Electrolytes	Process	Ionic Conductivity ($S \cdot cm^{-1}$) at RT	Ionic Conductivity ($S \cdot cm^{-1}$) at 100 °C
CaF ₂ [I]	A period of 24 hrs under humidity with a KCl salt solution bath - ball-milling time 18 hrs, speed: 600 rpm, with a ball-to-powder ratio of 18:1	1.880×10^{-5}	-
Sm_{1-x}Ca_xF_{3-x} (0 ≤ x ≤ 0.15) solid-solutions [II]			
SmF ₃	Ball-milling time: 18 hrs, speed: 600 rpm, with a ball-to-powder ratio of 18:1	1.140×10^{-6}	4.930×10^{-4}
Sm _{0.95} Ca _{0.05} F _{2.95}	Ball-milling time: 18 hrs, speed: 600 rpm, with a ball-to-powder ratio of 18:1	2.80×10^{-5}	5.810×10^{-4}
Sm _{0.90} Ca _{0.10} F _{2.90}	Ball-milling time: 18 hrs, speed: 600 rpm, with a ball-to-powder ratio of 18:1	1.60×10^{-5}	3.490×10^{-4}
Sm _{0.85} Ca _{0.15} F _{2.85}	Ball-milling time: 18 hrs, speed: 600 rpm, with a ball-to-powder ratio of 18:1	4.010×10^{-6}	2.410×10^{-4}
Pb_{1-x}Sn_xF₂ (x = 0.4 - 0.6) solid-solutions [III]			
x=0.40	Ball-milling time: 18 hrs, speed: 600 rpm, with a ball-to-powder ratio of 18:1	1.080×10^{-3}	1.160×10^{-2}
x=0.45	Ball-milling time: 18 hrs, speed: 600 rpm, with a ball-to-powder ratio of 18:1	2.53×10^{-3}	1.840×10^{-2}
x=0.50	Ball-milling time: 18 hrs, speed: 600 rpm, with a ball-to-powder ratio of 18:1	2.420×10^{-3}	4.730×10^{-3}
x=0.55	Ball-milling time: 18 hrs, speed: 600 rpm, with a ball-to-powder ratio of 18:1	1.840×10^{-3}	1.520×10^{-2}
x=0.60	Ball-milling time: 18 hrs, speed: 600 rpm, with a ball-to-powder ratio of 18:1	1.230×10^{-3}	4.560×10^{-3}

3.2 Vapor pressure-treated and ball-milled CaF_2 electrolyte [I]

Calcium fluoride has been a widely-investigated material that is known to be a promising host for solid-state materials for batteries but is also used for applications in electronics and optics. We aspired to prepare calcium fluoride with an abundant defect structure, see Figure 5, in order to enhance ion conductivity.

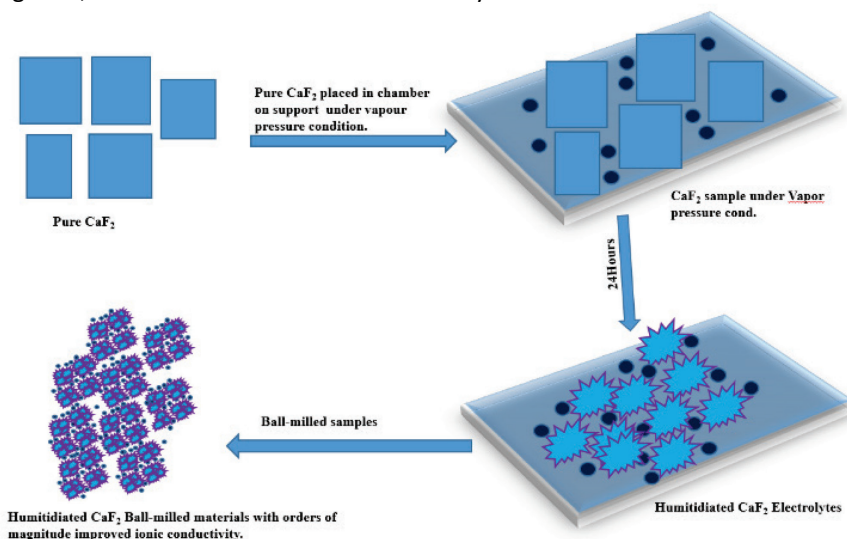


Figure 5. The process of surface stabilization due to vapor-pressure/ball-milling attaching the humidity onto CaF_2 nano-particles is depicted.

3.2.1 Structural studies of CaF_2

The XRD patterns of pure CaF_2 and treated samples were identified as being fluorite-type structures with a space group of Fm-3m (225), i.e., the basic cubic structure for the core of the particles remained stable. The dimensions of the unit cell are changing slightly related to the ionic radii of Ca^{2+} (5.4690 Å, 5.4673 Å, and 5.4626 Å) of pure, ball-milled and fully-treated CaF_2 samples, respectively. Rietveld refinement was carried out (Figure 6a) [94] to extract crystal parameters ($a = b = c = 5.46670$ Å). Particle sizes were mostly observed to change from 7.3 μm to 30 nm and the crystallite size from (D) 107 nm to 12.5 nm. Earlier reports indicated that ball-milling durations affect the crystallite size: processing times of four, eight, and sixteen hours introduced a change in the range of 30 nm. We obtained nano-particles with full size of 35–40 nm, as reported [95]. The results are listed in Table 4. With the aid of XPS measurements (Figure 6b), different sites in the CaF_2 electrolyte had been identified. F1s bulk and defect signals of the nano-material and O1s peaks could be deconvolution into four peaks, which are related to hydroxide, ionic oxygen, and oxygen bonded to carbon: OH^- (534.4 eV), C-O (533.0 eV), O^{2-} (531.8 eV), and C=O (530.5 eV). Related C1s spectra (not shown) provided two relative peaks at 284.4 and 288.9 eV, which are known to originate from the background source that has been applied for referencing [96].

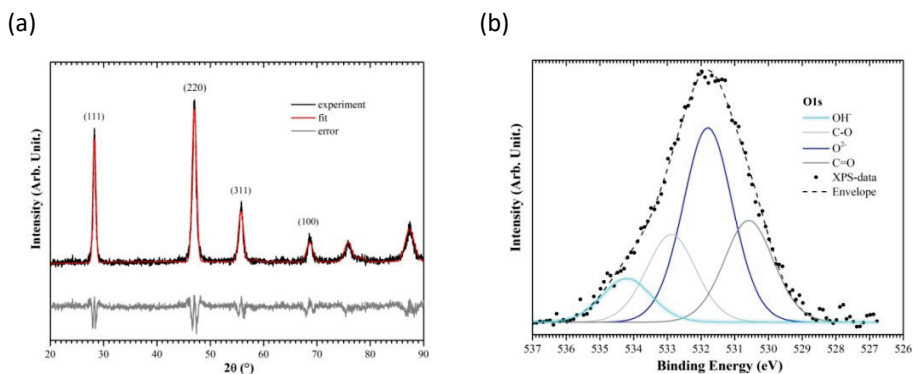


Figure 6. Crystallographic refinement for the fluorite-type structure of the electrolyte is shown in (a). High-resolution XPS spectra for the CaF_2 electrolyte are shown in (b): O1s peaks for C-O, C=O, OH, and O_2^- (a modified version of figure 1 in paper [1]).

3.2.2 Morphology studies for CaF_2

Scanning electron microscopy (SEM) and field emission scanning electron microscopy (FESEM) studies were carried out, illustrated in Figure 7. The pure CaF_2 sample provided particle sizes of 7-8 μm (Figure 7a), whilst the electrolyte gave 30 nm (Figure 7b). Agglomerates of CaF_2 of sizes ranging from a few dozens to several tens of nanometers are typically being observed as well. Cubic particles are usually related to pristine materials and are recognized in the product of ball-milled samples.

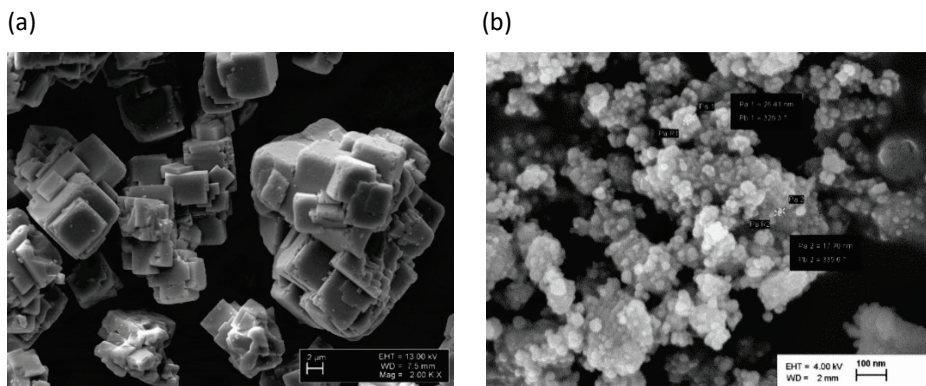


Figure 7. Morphology investigations of CaF_2 materials are depicted: pure sample image obtained at a resolution of 2 μm (a), and humidified/ball-milled CaF_2 electrolyte (b).

Table 4. A summary of XRD, SEM, FESEM, and EIS results.

Parameters	Pure CaF ₂	Ball-milled CaF ₂	Humidified and BM CaF ₂
Source of vapor pressure	-	-	Saturated KCl solution
Condition	-	-	24 hrs at 50 °C
Ball-milling time (h)	-	18	18
Cell parameter <i>a</i> (Å)	5.4690	5.4673	5.4626
Space group	Fm-3m (225)		
Crystallite size (nm)	106.7	15.6	12.5
Particle size (nm)	7320	50	30
Resistance (k·Ω)		439.65	4.633
Pellet diameter (mm)	-	10 (d)	10 (d)
Pellet thickness (mm)		1(t)	1(t)
Ionic conductivity at RT (S·cm ⁻¹)	7×10^{-11} [97]	1.98×10^{-7} 1.6×10^{-11} [94]	1.88×10^{-5}
Activation energy (eV)	-	0.56 (0.78 [94])	0.35

3.2.3 Ionic conductivity studies for CaF₂

The impedances within a critical frequency range were obtained for the pure CaF₂ and the electrolyte at various temperatures of up to +100 °C - see Figure 8a for details. Fitting of the measured Nyquist plots provided relevant material parameters [80][98][99]. The applied equivalent circuits model for the electrolyte (inset in Figure 8a) was composed of two constant phase elements (CPE1 & CPE2) and an ohmic resistor (R1) [85]. The capacitance values which corresponded to the semicircle (CPE1) were identified as being roughly about 10⁻⁸ F. Fluorite-type compounds are known to display only one such semicircle which represents a combined bulk/grain boundary phenomenon [94], and the second capacitance corresponded to the straight line (CPE2), this being within the range of 10⁻⁶ F, reflecting the electrode interface phenomena [100, 101]. Finally, the resistor is related to macroscopic ionic resistance [78][85]. The related ionic conductivity of fluoride ions in solid electrolytes can be determined from the resistance (*R*), the pellet thickness (*t*), and the surface area (*A*): $\sigma = [t/(R \cdot A)]$ [7][78]. It can be seen that the ionic conductivity considerably improves from -10 °C to room temperature. The change amounts to an order of magnitude, and further increases at higher temperatures of up to +40 °C. At an even higher temperature, the defect structure which promotes conductivity tends to decompose, and the ionic conductivity decreases.

For the electrolyte, the activation energy turned out to be 0.35 eV within the temperature range of -10 °C and +40 °C. For the untreated but ball-milled CaF₂ powder, 0.56 eV was extracted, which is in the order of reported values (0.78 eV) [78]. The conductivity decreases with the crystallite size, suggesting a conduction mechanism along the grain boundaries. While there are numerous reports on the enhancement of the ionic conductivity of nano-crystalline materials [102], the exact mechanism of conduction, its defect chemistry, and the nature of the disorder is still relatively unknown. We succeeded in showing that defects at the crystal's surface strongly influence the overall level of conductivity.

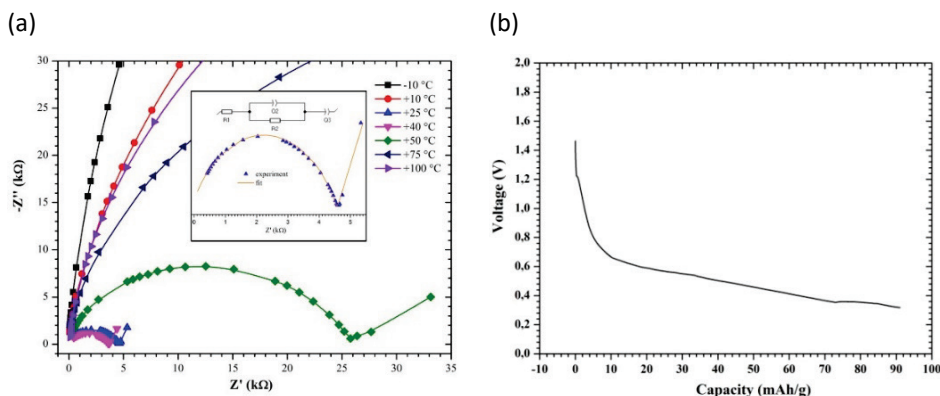


Figure 8. Nyquist plots for the Au/CaF₂ (humidified-bm)/Au pellet at temperatures between -10 °C and +100 °C. The discharge curve of an Mg/CaF₂/BiF₃ electrochemical cell using the superionic electrolyte operated at RT is shown in (b) (a modified version of figure 4 in paper [I]).

3.2.4 Cell preparation

For cathode material, a BiF₃ composite was selected [103], and for the anode, an Mg composite had been prepared. The anode composite was prepared by milling Mg (40%), as-prepared electrolyte CaF₂ (50%), and carbon black (10%). For the preparation of the cathode composite, BiF₃ (30%), as-prepared electrolyte CaF₂ (60%), and carbon black (10%) were used. For the preparation of the electrodes, a ball-to-powder weight was selected at a ratio of 12:1. The galvanic discharge profile for an Mg/CaF₂/BiF₃ cell which was operated at RT is shown in Figure 8b. The capacity of the battery was estimated by the weight of the active material. The BiF₃ composite electrode shows an achieved discharge capacity of 90 mA·h·g⁻¹, which is around 30% of the theoretical capacity (302 mA·h·g⁻¹). When discharging by applying a current load, the voltage drops from 1.5 V to 0.6 V initially, and then to 0.4 V at a much slower rate. Despite delivering a significant amount of discharge capacity, new charging was not possible due to a declining electronic and ionic conductivity for the production of the discharge electrode (MgF₂ or Bi). Nevertheless, the feasibility of CaF₂ as an electrolyte had successfully been proven in the fluoride-ion battery context.

3.3 High-energy ball-milling synthesis for Sm_{1-x}Ca_xF_{3-x} (0 ≤ x ≤ 0.15) [II]

3.3.1 Structural studies of Sm_{0.95}Ca_{0.05}F_{2.95}

Previous reports demonstrated a temperature-driven solid-state synthesis of Sm_{1-x}Ca_xF_{3-x} (0.05 ≤ x ≤ 0.17) from binary fluorides at 1000 °C followed by water quenching [85][104]. The best ionic conductivity ($\sigma_{RT} = 10^{-4} \text{ S}\cdot\text{cm}^{-1}$) was reported at room temperature for the composition of Sm_{0.95}Ca_{0.05}F_{2.95} [86]. We tested this concept over a range of 0 ≤ x ≤ 0.15 by robust BM synthesis [II]. The Sm_{0.95}Ca_{0.05}F_{2.95} diffraction patterns (Figure 9) indicate that the sample exhibits a tysonite-type trigonal structure (SmF₃) with space group P-3c1. For the SmF₃ system, two structural types – depending upon the synthesis method – are known: an orthorhombic YF₃-type structure (SG Pnma, Z = 4) or a LaF₃ tysonite-type structure (SG P-3c1, Z = 6) [85][80]. Average crystallite size of (D) = 10-18 nm, increasing with Ca²⁺ content, was identified from XRD [105]. The unit cell parameter, a, decreased monotonously, whereas the c parameter mostly increases with Ca²⁺ mixing (x) and related anionic vacancies [106, 107]. Already a minor introduction of Schottky defects

during high-energy ball-milling stabilizes the tysonite-structure and provides a consistent parameter change dependent on doping levels. The resulting volume change of the unit cell is mostly dependent upon the ionic radii of Sm^{3+} and Ca^{2+} (1.27 and 1.32 Å), implying an expansion of the unit cell parameters [85]. Even so, at a specific level of anionic vacancies, i.e., when a preferential stabilization of fluoride vacancies within the vicinity of Ca^{2+} ions can be reached, the net volume decreases.

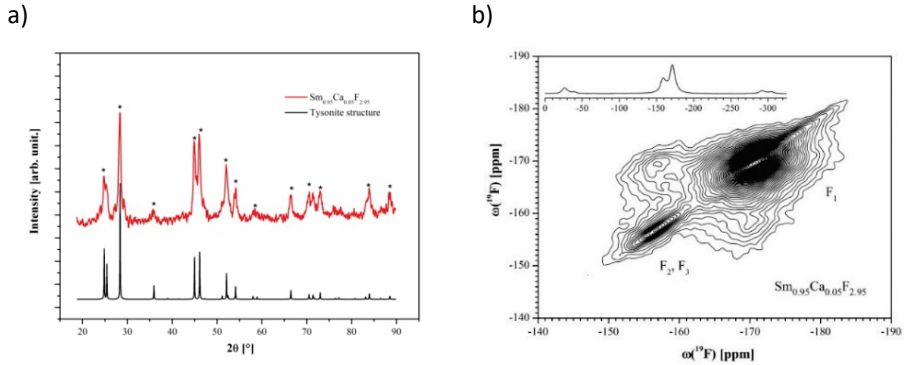


Figure 9. The x-ray diffraction pattern for $\text{Sm}_{0.95}\text{Ca}_{0.05}\text{F}_{2.95}$, which provides evidence of a tysonite-type structure (trigonal, as shown by the simulated black line) is shown in a). In b) ^{19}F high-resolution MAS 1D and 2D exchange experiments (measured at RT) also support the presence of a trigonal structure, indicating three lattice sites (F_1 , F_2 , and F_3) which is consistent with the literature (a modified version of figure 1 in paper [11]).

Fluorine nuclear magnetic resonance experiments (^{19}F -NMR) were carried out on a Bruker spectrometer, using a fast MAS probe. Experiments were carried out at room temperature. The decrease in the ionic conductivity and the linear increase of the activation energy versus Ca concentration can be explained by the vacancies around the calcium sites. The results are seen in Figure 9 and listed in Table 5.

3.3.2 Morphology studies for $\text{Sm}_{0.95}\text{Ca}_{0.05}\text{F}_{2.95}$

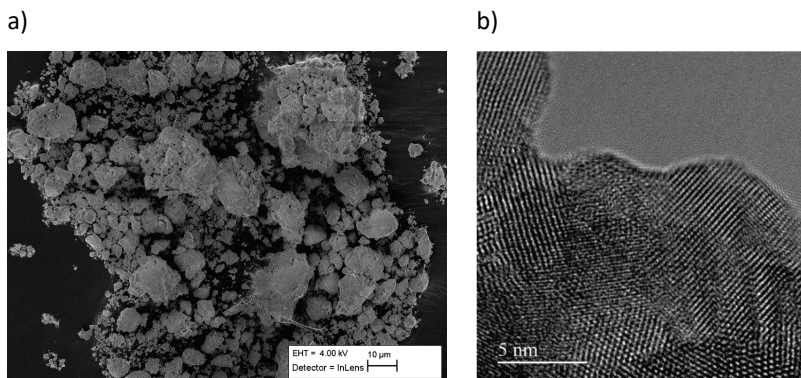


Figure 10. The FESEM morphology for $\text{Sm}_{0.95}\text{Ca}_{0.05}\text{F}_{2.95}$ is provided in a) showing resolutions (the scale bars of 10 µm). HRTEM images of the same material are given in b) with resolution scale of 5 nm.

High-resolution transmission electron microscopy (HRTEM) and SEM were applied in order to be able to investigate the morphology of $\text{Sm}_{0.95}\text{Ca}_{0.05}\text{F}_{2.95}$ as illustrated in Figure 10. The average particle size of around 50 nm had been extracted from the SEM image. The sample consists of an agglomeration of nano-particles as seen from the electron microscope images [108].

Table 5. Data for the $\text{Sm}_{1-x}\text{Ca}_x\text{F}_{3-x}$ ($0 \leq x \leq 0.15$) solid electrolytes are collected.

Parameters	$\text{Sm}_{1-x}\text{Ca}_x\text{F}_{3-x}$ ($0 \leq x \leq 0.15$)			
	$x=0$	$x=0.05$	$x=0.10$	$x=0.15$
Cell dimension a (Å)	6.96	6.95	6.95	6.95
Cell dimension c (Å)	7.12	7.13	7.14	7.13
Crystallite size (nm)	10.4	12.9	13.9	18.0
Ionic conductivity at RT ($\text{S}\cdot\text{cm}^{-1}$)	1.1×10^{-6} (0.1)	2.8×10^{-5} (0.1)	1.6×10^{-5} (0.1)	4.0×10^{-6} (0.1)
Ionic conductivity at 100 °C ($\text{S}\cdot\text{cm}^{-1}$)	4.9×10^{-4}	5.8×10^{-4}	3.5×10^{-4}	2.4×10^{-4}
E_a (eV)	0.55 (0.04)	0.40 (0.05)	0.42 (0.04)	0.53 (0.07)

3.3.3 Ionic conductivity studies for $\text{Sm}_{0.95}\text{Ca}_{0.05}\text{F}_{2.95}$

The ionic conductivities of the electrolytes at temperatures between 25 °C and 100 °C are shown in Figure 11. The spectra consist of a semi-circle at high frequency (MHz), and a straight line at low frequency (Hz), which represents the charging of ionic species at the electrolyte-electrode interface [101][109][110]. The total resistance of the system corresponds to the real part of the complex impedance and is determined at the intercept point of the measured spectra with the x-axis at low frequency [111]. An estimated ionic conductivity of $2.8 \times 10^{-5} \text{ S}\cdot\text{cm}^{-1}$ at RT has been obtained. The activation energy, E_a , can be extracted from the temperature dependence of the ionic conductivity, assuming Arrhenius-type behavior, being $\sigma_T = \sigma_0 \times \exp(-E_a/k \cdot T)$, where σ_0 is the ionic conductivity, T is the temperature. The highest conductivities were obtained at $2.8 \times 10^{-5} \text{ S}\cdot\text{cm}^{-1}$ at room temperature and $5.8 \times 10^{-4} \text{ S}\cdot\text{cm}^{-1}$ at 100 °C, for $x = 0.05$ ($\text{Sm}_{0.95}\text{Ca}_{0.05}\text{F}_{2.95}$). At room temperature, the conductivity decreases exponentially as a function of the calcium concentration. Interestingly, the activation energy increases with (x). The value of E_a for $\text{Sm}_{0.95}\text{Ca}_{0.05}\text{F}_{2.95}$ seems to be lower than or equivalent to other solid solutions with a tysonite-type structure (0.40 eV). For higher (x), the activation energy increases up to 0.53 eV, and the conductivity decreases at RT.

Considering a relatively high ionic conductivity, $\text{Sm}_{0.95}\text{Ca}_{0.05}\text{F}_{2.95}$ seems a suitable candidate for FIB development [1]. In comparison, solid electrolytes such as $\text{La}_{0.9}\text{Ba}_{0.1}\text{F}_{2.9}$ have been proposed despite lower rates of conductivity, $\sim 5 \times 10^{-6} \text{ S}\cdot\text{cm}^{-1}$ at RT and $3 \times 10^{-4} \text{ S}\cdot\text{cm}^{-1}$ at 150 °C [77][112].

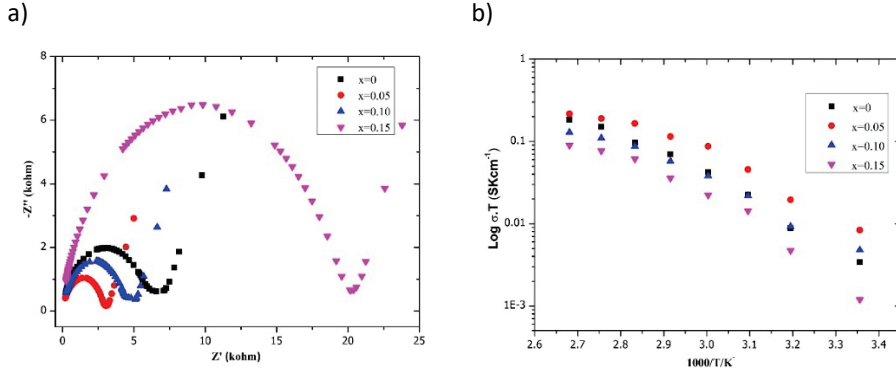


Figure 11. In a), impedance measurements for $Sm_{1-x}Ca_xF_{3-x}$ ($0 \leq x \leq 0.15$) are shown, while in b), related ionic conductivities from RT to 100 °C are represented (a modified version of figure 3 in paper [III]).

We validated the $Sm_{0.95}Ca_{0.05}F_{2.95}$ as a solid-state electrolyte also in *in situ*, as an electrochemical cell $CeF_3/Sm_{0.95}Ca_{0.05}F_{2.95}/Bi$ [113]. The cells were fabricated by pressing together a CeF_3 anode composite, electrolyte ($Sm_{0.95}Ca_{0.05}F_{2.95}$), and a Bi composite cathode into a 10 mm diameter battery pellet which was sealed within an air-tight CR2032 coin cell case. Electrochemical testing of the cell was carried out at 75 °C. The electrochemical cell was charged/discharged with a current density of $1 \mu A \cdot cm^{-2}$ within a voltage interval between 0.01 V and 0.90 V. The overall Coulomb efficiency of the active material was initially almost 50%, this reduced during cycling as the fraction of the active material constantly decreased.

3.4 $Pb_{1-x}Sn_xF_2$ ($0.4 \leq x \leq 0.6$) solid-solutions [III]

As-synthesized fluorite-type electrolytes were based on SnF_2 and PbF_2 materials via the BM method [III]. SnF_2 forms both simple and complex fluorides, among which the most attention have gained compounds of the $MeSnF_4$ ($Me = Pb, Ba, Sr$) composition, due to high ionic conductivity even at room temperature [14]. The structural role was considered in terms of Sn^{2+} cations with lone electron pairs in anionic conductors: $MSnF_4$ ($M = Pb, Ba, Sr$). Several investigations have been devoted to this material studying electrical properties, phase transitions, ionic mobility, ionic transport mechanisms, ionic conductivity, but most for the first case: $PbSnF_4$ [15]. It has been observed that the ionic conductivity of β - PbF_2 has enhanced by the addition of aliovalent cations due to the formation of charge-compensating vacancies or interstitials within the anion sublattice. $PbSnF_4$ so far has the highest known fluoride-ion conductivity in the range of $10^{-3} S \cdot cm^{-1}$ at room temperature.

We investigated the synthesis of $Pb_{1-x}Sn_xF_2$ ($x = 0.4 - 0.6$) solid solutions by means of room temperature mechano-chemical BM without prior processing of the original materials. Ball-milling was observed to drive the crystalline structure of $Pb_{1-x}Sn_xF_2$ mainly cubic γ - $Pb_{1-x}Sn_xF_2$ while some peaks of the tetragonal α - $PbSnF_4$ -like structure were identified.

3.4.1 Structural studies for $\text{Pb}_{1-x}\text{Sn}_x\text{F}_2$ ($x = 0.40 - 0.60$)

The investigation of the material with XRD and NMR revealed that the formation of a β -type structure with three magnetically independent lattice-sites is achieved from the α -type by simple ball-milling. XRD data, shown in Figure 12a, indicate crystal phases α -, β - orthorhombic and cubic γ - $\text{Pb}_{1-x}\text{Sn}_x\text{F}_2$, and compositions properties which depend strongly upon the preparation method or process parameters. ^{19}F -NMR shows that obtained PbF_2 and SnF_2 were mostly nano-crystalline, and not a mixture of microcrystalline/amorphous PbF_2 and SnF_2 (Figure 12b). Consequently, ball-milling results in a phase transition to a nano-crystalline phase: cubic fluorite-type γ - PbSnF_4 -like structure has been found. From ^{19}F -NMR MAS results, we can also deduce that mechano-chemical high-energy synthesis is introducing surface defects which are naturally exchanging with the nano-particle core [114]. This interaction also promotes conductivities at the crystallite and particle boundaries to make ion mobility more accessible at the macroscopic material level, which is evidenced by the low activation energies and high ionic conductivities at room-temperature, see Table 6. Such activation energies had previously been reported, but these were attributed to internal fluoride-ion mobility not accessible to the bulk conductivity [115].

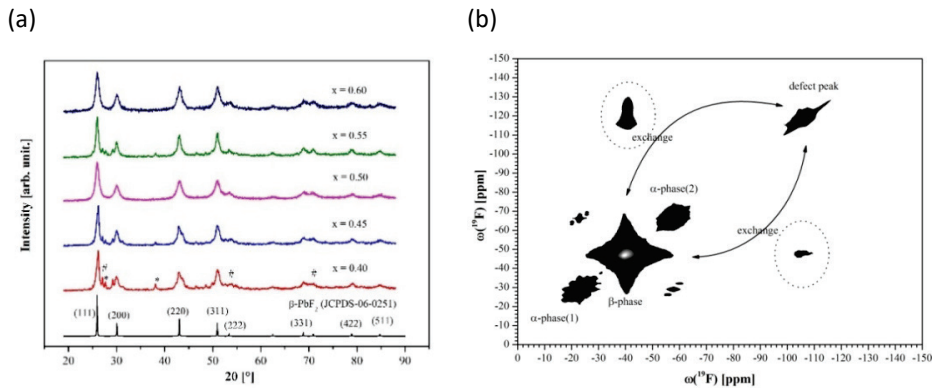


Figure 12. In (a) the XRD patterns of $\text{Pb}_{1-x}\text{Sn}_x\text{F}_2$ ($x = 0.40 - 0.60$) are shown which indicate mostly a cubic fluorite-type γ - PbSnF_4 -like structure. The hash symbols (#) present reflexes from a tetragonal α - PbSnF_4 -like structure. (b) ^{19}F -NMR 2D exchange spectra. The dominant beta-phase is along with a remaining α -phase and surface defects, and all phases spin-exchange (a modified version of figure 1 in paper [111]).

3.4.2 Morphology and chemical composition for $\text{Pb}_{1-x}\text{Sn}_x\text{F}_2$ ($x = 0.45$)

Field emission scanning electron microscopy (FESEM) was used to illustrate the morphology of $\text{Pb}_{1-x}\text{Sn}_x\text{F}_2$ ($x = 0.45$) with a resolution scale of $20 \mu\text{m}$ (see Figure 13a). When analyzing samples of the powder, grain sizes were estimated to be between 75-100 nm. It also became evident that the high-energy ball-milling leads to an agglomeration in the nano/micro-range [114]. The HRTEM of PbF_2 nano-particles can be seen in Figure 13b at a resolution scale of 5 nm. The dominating β -phase at (111) directions [98][108], can be observed. When carrying out an EDX element analysis on the electrolyte ($x = 0.45$), we obtained readings for a lead that were 55 %, and for tin 45 %, thereby confirming the purity of the synthesis.

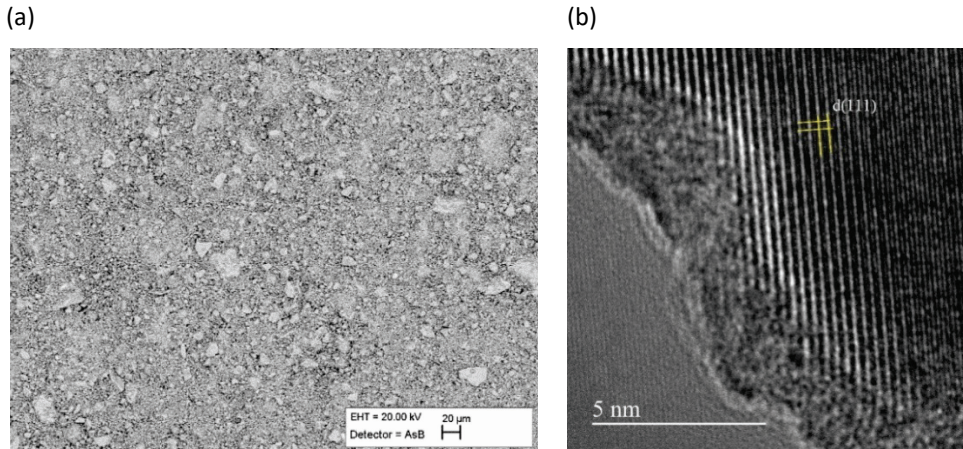


Figure 13. In (a) the FESEM morphology is shown for the synthesized $Pb_{1-x}Sn_xF_2$ sample ($x = 0.45$) with a resolution scale of $20 \mu m$. A considerable level of agglomeration can be observed due to high-energy ball-milling. In (b) HRTEM picture is given (5 nm resolution scale) for a sample of ($x=0$). PbF_2 nano-particles with a dominating beta-phase are visible. (a modified version of figure 2 in paper [III]).

Table 6. Summarized results of $Pb_{1-x}Sn_xF_2$ ($x = 0.40 - 0.60$) ball-milled samples.

Parameters	$Pb_{1-x}Sn_xF_2$ ($x=0.40-0.60$)				
	$x=0.40$	$x=0.45$	$x=0.50$	$x=0.55$	$x=0.60$
Cell parameters ($a \gamma\text{-PbSnF}_4$) (\AA)	5.93910	5.93940	5.94674	5.94589	5.94065
Crystallite size (nm)	17.36	17.27	17.50	17.46	17.38
Ionic conductivity at RT ($S \cdot cm^{-1}$)	1.08×10^{-3}	2.53×10^{-3}	2.42×10^{-3}	1.84×10^{-3}	1.23×10^{-3}
Ionic conductivity at $100^\circ C$ ($S \cdot cm^{-1}$)	1.16×10^{-2}	1.83×10^{-2}	4.73×10^{-3}	1.52×10^{-2}	4.56×10^{-3}
E_a (eV)	0.32 (0.05)	0.30 (0.05)	0.38 (0.04)	0.31(0.07)	0.42(0.04)

3.4.3 Ionic conductivities for ball-milled $Pb_{1-x}Sn_xF_2$ ($x = 0.40 - 0.60$) electrolytes

The ionic conductivities of solid electrolytes were investigated by impedance spectroscopy with two copper-blocking electrodes. Typical impedance spectra of the ball-milled $Pb_{1-x}Sn_xF_2$ ($x = 0.40 - 0.60$) electrolytes were measured from room temperature to $100^\circ C$ (see Figure 14a). The highest ionic conductivity of $2.5 \times 10^{-3} S \cdot cm^{-1}$ at RT and $1.9 \times 10^{-2} S \cdot cm^{-1}$ at $100^\circ C$ with an activation energy of 0.30 eV were obtained for $x = 0.45$. The results allowed us to prove the creation of crystal surface defects, as claimed in our patent [116]. $Pb_{1-x}Sn_xF_2$ as a solid-electrolyte for FIB applications. This electrolyte was also used for *in situ* testing. We tested an electrochemical cell which was assembled from a bismuth metal composite cathode (40% Bi-metal powder,

10% carbon black, 10% PVdF, and 40% $\text{Pb}_{0.55}\text{Sn}_{0.45}\text{F}_2$), and Cerium(III)-fluoride composite anode (80% CeF_3 , 10% CB, 10% PVdF), and the solid electrolyte $\text{Pb}_{0.55}\text{Sn}_{0.45}\text{F}_2$ as a separator.

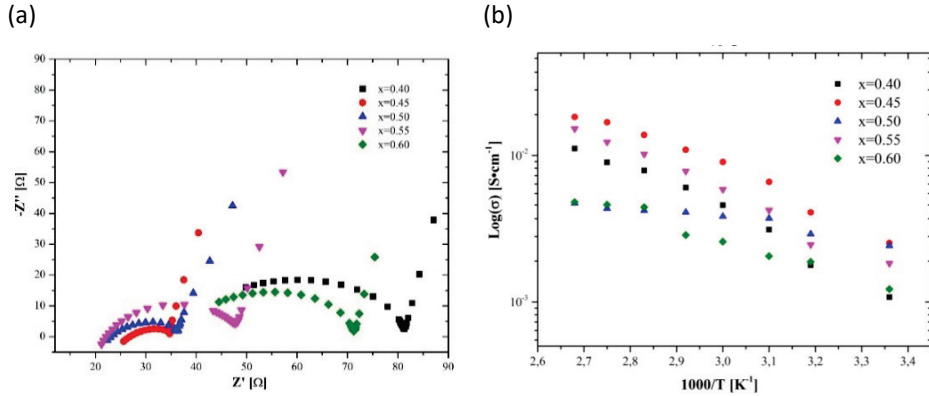


Figure 14. EIS measurement of $\text{Pb}_{1-x}\text{Sn}_x\text{F}_2$ ($x = 0.40 - 0.60$): in (a) the Nyquist plots are depicted for the electrolytes at room temperature; while (b) provides the ionic conductivities (RT to 100 °C) that were used for fitting the Arrhenius equation (a modified version of figure 3 in paper [III]).

The pressed pellet was inserted into the coin cell under the argon atmosphere. The cell was charged/discharged within a voltage range of 0.01 and 1.5 V with a current density of $1 \mu\text{A}\cdot\text{cm}^{-2}$. The obtained cycling behavior and coulomb efficiency are shown in Figure 15. After the few cycles, the cell capacity drops down to 40% of the cell capacity of the active material. Such a problem may be overcome by using a composite electrode of active material with a different ratio of binders and conductive additives. The loss of interparticle contact and the effect on capacity fading is a well-known phenomenon of conversion materials. The electrolyte/electrode contact may be further weakened during the charge and discharge process if the electrode materials experience large volume changes. Therefore, using more appropriate electrode materials, or using appropriate binders for stabilization of the electrode/electrolyte interface are possible approaches to improve the electrochemical performance of FIB.

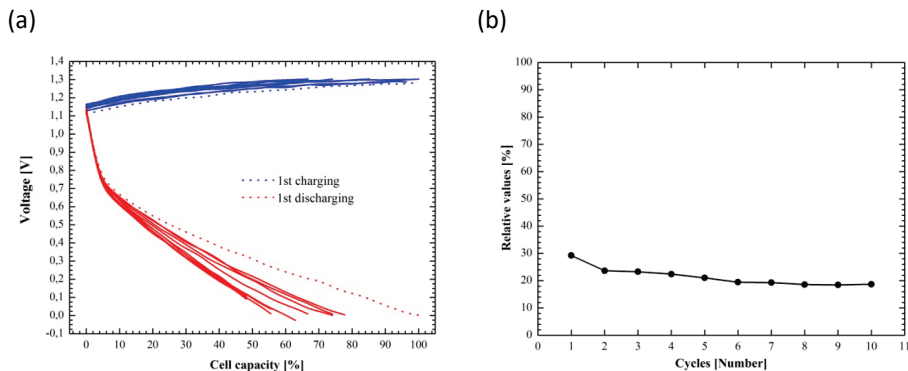


Figure 15. Electrochemical charge/discharge performance of $\text{CeF}_3/\text{Pb}_{0.55}\text{Sn}_{0.45}\text{F}_2/\text{Bi}$ at room temperature RT for ten cycles (a). Related coulomb efficiency is depicted in (b). Cell capacity is related to the active material. (a modified version of figure 5 in paper [III]).

3.5 Preparatory and unpublished experiments, theoretical considerations

At the start of the process, a collection of solid solution compounds was tested in order to screen promising ionic conductivities for RT performance. Three different systems were pursued: (a) rare-earth solid-state electrolytes ($\text{La}_{1-x}\text{Ba}_x\text{F}_{3-x}$); (b) humidified CaF_2 electrolytes; and (c) CaF_2 -mixed with SmF_3 . Our target value was about ($10^{-3} - 10^{-4} \text{ S}\cdot\text{cm}^{-1}$).

3.5.1 Rare-earth solid-state electrolytes ($\text{La}_{1-x}\text{Ba}_x\text{F}_{3-x}$)

We tested LaF_3 & BaF_2 in different stoichiometric ratios $\text{La}_{1-x}\text{Ba}_x\text{F}_{3-x}$, $x = 0.05$ & 0.15 . The ball-to-powder material ratio was 18:1, with the process being carried out at 600 rpm for a period of eighteen hours with silicon nitride jars and various sizes of silicon nitride balls (5 mm, 10 mm, and 3 mm). The structure and conductivity studies for the samples were carried out by means of XRD and EIS techniques. Crystallite size of $\text{La}_{0.95}\text{Ba}_{0.05}\text{F}_{2.95}$ of around 10 nm was extracted, and the highest conductivity obtained at $9 \times 10^{-5} \text{ S}\cdot\text{cm}^{-1}$ at 150°C .

Table 7. The results of ball-milled and sintered samples of $\text{La}_{0.95}\text{Ba}_{0.05}\text{F}_{2.95}$ are given.

Compound ($\text{La}_{0.95}\text{Ba}_{0.05}\text{F}_{2.95}$)	Ball-milled	Sintered
Time (h)	Ball-milling 18 hrs	Sintering time 2 hrs
Cell parameters (Å)	a = 7.1945, c = 7.36	a = 7.1875, c = 7.363
Crystallite size (nm)	8.5	118.5
σ at 150°C ($\text{S}\cdot\text{cm}^{-1}$)	9×10^{-5}	8×10^{-4}
Particle size	100 nm	50 nm

The ball-milled $\text{La}_{0.95}\text{Ba}_{0.15}\text{F}_{2.95}$ powder was dried in a vacuum for one hour before being sealed in a quartz tube. The tube was heated to 800°C at $20^\circ\text{C}\cdot\text{min}^{-1}$ and the temperature was maintained for two hours, cooling down to $20^\circ\text{C}\cdot\text{min}^{-1}$ using a muffle furnace. Following the sintering treatment, the electrolyte powder was pressed using a pellet press under an air atmosphere. The pressed sintered powder pellet (with a diameter of 10 mm and a thickness of 0.59 mm) was coated on both sides with gold in order to ensure ion blockage. The pellet delivered an ionic conductivity of around $8 \times 10^{-4} \text{ S}\cdot\text{cm}^{-1}$ at 150°C (see Table 7). In comparison, $\text{Ba}_{0.06}\text{La}_{0.04}\text{F}_{2.94}$ and $\text{La}_{0.90}\text{Ba}_{0.10}\text{F}_{2.90}$ ionic conductivities at room temperature are within the range of 10^{-7} to 10^{-8} and 10^{-4} to 10^{-5} at 160°C .

The number of other compounds, synthesized with different media, milling time, and speed is shown in Table 8. Most of the samples revealed RT ionic conductivity levels at 10^{-7} to 10^{-9} .

Table 8. Collection of various compounds which were synthesized by means of ball-milling.

Compound	Ball-milling speed (rpm)	Ball-milling time(h)	σ at RT ($S\cdot cm^{-1}$)
$La_{0.95}Ba_{0.05}F_{2.95}$	600	12, 14, 18, 24, 30	6.30×10^{-7}
$La_{0.85}Ba_{0.15}F_{2.85}$	600	12, 14, 18, 30	7.00×10^{-8}
$La_{0.85}Ba_{0.15}F_{2.85}$ with water	600	12, 18	6.51×10^{-9}
$La_{0.90}Ba_{0.10}F_{2.90}$	600	12, 18	4.52×10^{-7}
$La_{0.70}Ba_{0.30}F_{2.70}$	600	18	
CaF_2 under NaCl	600, 400	18, 24	4.38×10^{-8}
CaF_2 with water	600	18	5.18×10^{-8}
CaF_2 with CaO	600	18	3.15×10^{-7}
SmF_3 (pre-treated 1000 °C)	600	18	-
CaF_2 with DEG	300	12	-
CaF_2 with oleylamine	300	12	-
90% CaF_2 doped 10% CaO	600	18	7.38×10^{-7}
80% CaF_2 doped 20% CaO	600	18	-
75% CaF_2 doped 25% CaO	600	18	-
25% CaF_2 doped 75% CaO	600	18	-
alpha PbF_2	300, 600	12	3.26×10^{-7}
beta PbF_2	300, 600	12	-
$Ba_{0.80}Sn_{0.20}F_{2.80}$	600	18	7.45×10^{-7}

3.5.2 Humidified CaF_2 ball-milled electrolytes

The CaF_2 material was prepared by means of two different processes (see Figure 16). In process [I], pure CaF_2 material was exposed to salt solution bath of a saturated NaCl aqueous solution, for a period of twenty-four hours at 50 °C, and the samples were kept on a glass substrate within a closed container. The vaporized sample was ball-milled for a period of eighteen hours at 600 rpm. The ball-milled sample had a conductivity of only $4.7 \times 10^{-6} S\cdot cm^{-1}$ at RT [128] whilst a fluorite-type cubic structure was verified. Other ways were tried to improve the conductivities like subjecting the sample to a preparatory ball-milling before vapor exposure. Contrary to our expectations, the conductivity levels were even lower, at around $5.7 \times 10^{-7} S\cdot cm^{-1}$.

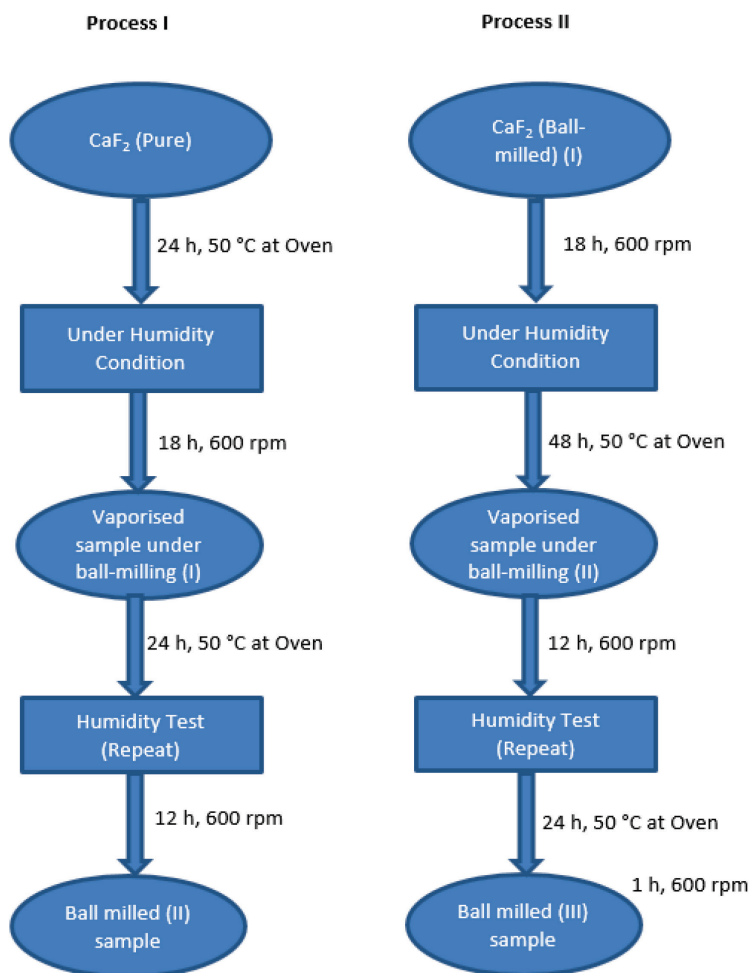


Figure 16. The flow chart for two different processes involving CaF_2 electrolytes as prepared under vapor pressure condition. Ball-milling time (of 18 hrs & 12 hrs, at 600 & 400 rpm) and humidifying conditions (24 hrs & 48 hrs at 50 °C) were used.

Further extension of the water exposure did not improve conductivity; it remained around $3 \times 10^{-7} \text{ S}\cdot\text{cm}^{-1}$ at RT. The repeated humidifying-and-milling cycles increased the conductivity levels to $7 \times 10^{-6} \text{ S}\cdot\text{cm}^{-1}$.

3.5.3 $\text{Ca}_x\text{Sm}_{1-x}\text{F}_{3-x}$ ($0 \leq x \leq 0.15$) solid-solutions

A $\text{Ca}_{0.95}\text{Sm}_{0.05}\text{F}_{2.95}$ sample was ball-milled at 600 rpm, for eighteen hours under vacuum conditions. The best ionic conductivity level was achieved in $\text{Ca}_{0.95}\text{Sm}_{0.05}\text{F}_{2.95}$ at around $2.8 \times 10^{-6} \text{ S}\cdot\text{cm}^{-1}$ at RT, other compositions were screened for conductivities ($10^{-7} - 10^{-8} \text{ S}\cdot\text{cm}^{-1}$) at RT as can be seen in Table 9.

Table 9. The list of compounds is ball-milled under different conditions.

Solid electrolytes	Process		Impedance resistance (k $\cdot\Omega$) at RT	Ionic conductivity (S $\cdot\text{cm}^{-1}$) at RT
Ca _{0.95} Sm _{0.05} F _{2.95}	Vacuum	18hrs, BM (600 rpm)	27.38	2.80 $\times 10^{-6}$
Ca _{0.90} Sm _{0.10} F _{2.90}	Vacuum	18 hrs, BM (600 rpm)	82.97	9.23 $\times 10^{-7}$
Ca _{0.85} Sm _{0.15} F _{2.85}	Vacuum	18 hrs, BM (600 rpm)	259.84	2.95 $\times 10^{-7}$
Ca _{0.95} Sm _{0.05} F _{2.95}	Pre-heating at 150 °C for around 24 hrs	18 hrs, BM (600 rpm)	1179.87	6.49 $\times 10^{-8}$
Ca _{0.95} Sm _{0.05} F _{2.95}	CaF ₂ BM separately for 12 hrs & SmF ₃ BM 12 hrs	18 hrs, BM (600 rpm)	959.87	7.98 $\times 10^{-8}$
Ca _{0.95} Sm _{0.05} F _{2.95}	Zirconia balls	18 hrs, BM (600 rpm)	169.5	4.52 $\times 10^{-7}$
Ca _{0.95} Sm _{0.05} F _{2.95}	N ₂ gas	18 hrs, BM (600 rpm)	1244.5	3.55 $\times 10^{-8}$
Ca _{0.95} Sm _{0.05} F _{2.95}	Air media	18 hrs, BM (600 rpm)	Straight line	-
Ca _{0.95} Sm _{0.05} F _{2.95}	CaF ₂ humidity (NaCl & KCl)	18 hrs, BM (600 rpm)	Straight line	-

All conductivities presented here provided low values; we speculate that the quality of solid solutions and the lack of a well-controlled environment during the preparation may have been a culprit, along with pre-processing and post-processing. A more systematic approach, one which comprises a hand-in-hand structural and morphological analysis, along with continuous parameter variations in terms of chemical composition, would be commendable, but not compatible with our resources and infrastructure during this Ph.D. course.

3.5.4 Usage of Pb in FIB

This topic merits special attention in the context of predictable transition to electric vehicles, making all lead-acid batteries redundant and environmental problem. In the case of 1:1 substitution, about 10 kg of lead will be available for each new car battery, of ca 100 kWh capacity. There are several composite materials available to use in fluoride-ion batteries. At the moment, a solid electrolyte PbSnF promising candidate and it is a big challenge to identify for the electrodes of this electrolyte. CuF₂/Pb (0.7 V, 1,050 Wh.L⁻¹), AgF₂/Pb (1.3 V, ~1,500 Wh.L⁻¹), and Bi/PbF₂ (0.3 V, ~425 Wh.L⁻¹) are examples of systems that have been already studied but unfortunately failed to deliver the capacity after few cycles. But CuF₂/Pb based systems doesn't able to rechargeable with PbSnF solid electrolyte. Future work is very likely improving the efficiency of Pb or PbF₂ use.

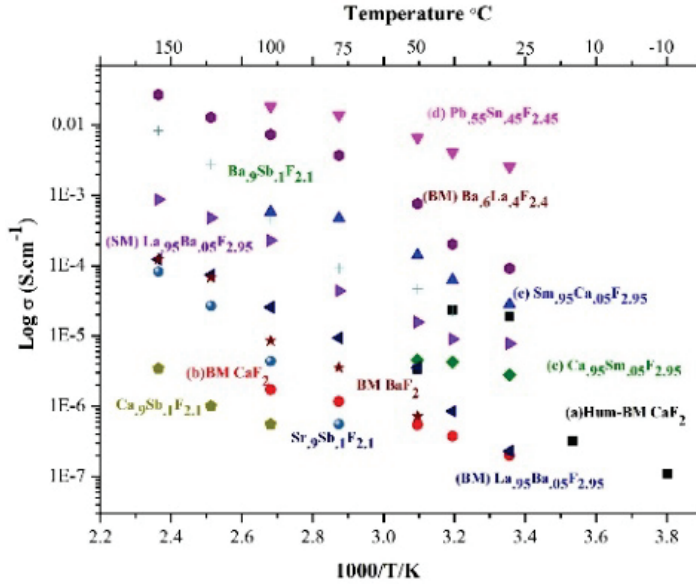
Conclusions

At present, investigations and improvements of ionic conductivities of solid electrolytes are attracting considerable attention. In this thesis, we have reviewed the literature on solid-state fluoride-ion conductors. As per published data, the $\text{La}_{1-x}\text{Ba}_x\text{F}_{3-x}$ (LBF) electrolytes provided conductivities of 10^{-5} - 10^{-6} $\text{S}\cdot\text{cm}^{-1}$ at room temperature. Due to enhanced ionic mobility at higher temperatures, the conductivity increases to 10^{-4} - 10^{-5} $\text{S}\cdot\text{cm}^{-1}$. Recently reported electrolytes like $\text{Sm}_{1-x}\text{Ca}_x\text{F}_{3-x}$ and $\text{Ce}_{1-x}\text{Sr}_x\text{F}_{3-x}$ (10^{-4} $\text{S}\cdot\text{cm}^{-1}$) are plausible candidates for RT-FIB applications. However, so far, no results have been presented in actual FIB usage. We have identified the most promising solid fluoride-ion conductors [I-III] and also performed *in-situ* testing in the solid-state fluoride-ion battery cell environment.

- ❖ Calcium fluoride conductivity was increased by two orders of magnitude, to 1.9×10^{-5} $\text{S}\cdot\text{cm}^{-1}$ at RT, with enhanced defect structure by the application of vapor-pressure exposure followed by high-energy ball-milling. The calcium fluoride electrolyte remains in its basic cubic structure, crystallite/particle sizes of 12/30 nm were obtained by XRD and SEM analyses. The synthesized material provides a sufficient ionic conductivity for electrochemical testing and refinement of FIBs [I].
- ❖ CaF_2 as a dopant can alter significantly properties of SmF_3 ($\text{Sm}_{1-x}\text{Ca}_x\text{F}_{3-x}$) within the stoichiometric ratio range $0 \leq x \leq 0.15$. From XRD and FESEM, it was revealed that the solid electrolytes constitute in a tysonite-type structure with an average crystallite/particle size of 10-20 / 50 nm. The best ionic conductivity of 2.8×10^{-5} $\text{S}\cdot\text{cm}^{-1}$ at RT was achieved for $\text{Sm}_{0.95}\text{Ca}_{0.05}\text{F}_{2.95}$. Finally, a proof-of-principle fluoride-ion solid-state battery cell was tested based on a $\text{CeF}_3/\text{Sm}_{0.95}\text{Ca}_{0.05}\text{F}_{2.95}/\text{Bi}$ electrochemical system [II].
- ❖ Higher conductivities were obtained with $\text{Pb}_{1-x}\text{Sn}_x\text{F}_2$ over a studied solid solution range of $x = 0.4 - 0.6$. From XRD, a dominant γ -phase (β - PbF_2 -type) cubic structure and crystallite sizes of around 17 nm were observed. The ionic conductivity was optimized to 2.3×10^{-3} $\text{S}\cdot\text{cm}^{-1}$ at RT, with an activation energy of 0.30 eV, for $x = 0.45$. This electrolyte was applied for *in-situ* testing in a FIB assembly which consisted of a Bi-cathode and CeF_3 -anode [III]. With a preparation process improvement and more suitable electrode materials, PbSnF_2 may find an important application as a solid electrolyte.

The overall ionic conductivities are shown in Figure 17a. Also, represented are the other existing solid fluoride electrolytes and, for comparison, Li-ion electrolytes as reported in other published work (Figure 17b)

(a)



(b)

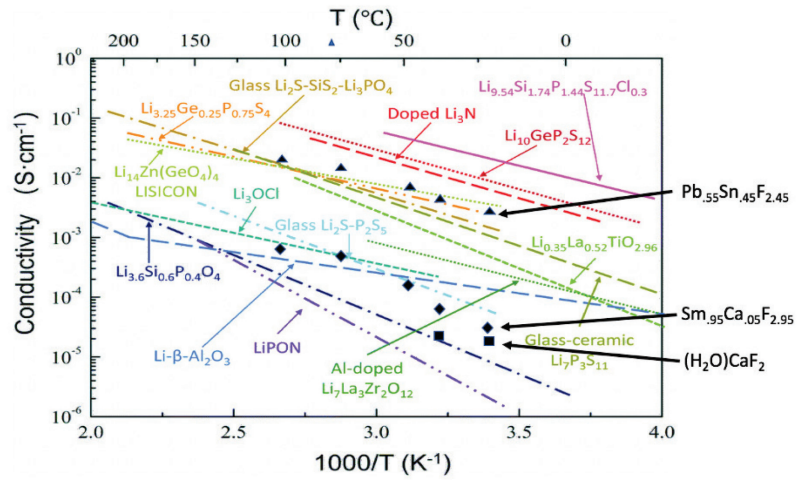


Figure 17. (a) Overall ionic conductivities for different solid-state fluoride-type electrolytes as a function of temperature (with a-e indicated in this report); while (b) shows ionic conductivities for Li-ion electrolytes as available in the literature, overlaid with our best results in each class. Solid ceramic and glass Li-ion electrolytes are compared with fluoride solid ion conductors. Part of the figure reproduced from ref. [117] with permission from Science publisher.

The fluoride-ionic conductivities (Table 10) of the studied materials were in the range between 10^{-3} to 10^{-6} S·cm⁻¹, an outcome that is not much inferior to that for gel electrolytes as used in LIB. The solid electrolytes, as-synthesized and characterized here, constitute a new and promising platform for all-solid FIB development.

Table 10. List of solid-state fluoride-ionic conductors and the best ionic conductivities at RT as reported in the available literature.

Solid-state electrolyte	Mobility ion	Ionic conduct.: (σ) at RT ($S \cdot cm^{-1}$)	Method	Ref.
La _{0.95} Ba _{0.05} F _{2.95}	F ⁻	4.50×10^{-6}	Annealing + high-energy ball-milling + sintering	[78]
La _{0.90} Ba _{0.10} F _{2.90}	F ⁻	2.75×10^{-6}	High-energy ball-milling + sintering	[78][107]
La _{0.90} Ba _{0.10} F _{2.90}	F ⁻	1.20×10^{-6}	High-energy ball-milling + sintering	[118]
La _{0.95} Ca _{0.05} F _{2.95}	F ⁻	2.0×10^{-6}	Single crystal	[119]
La _{0.8} Ca _{0.2} F _{2.8}	F ⁻	1.0×10^{-6}	Ball-milling + annealing	[120]
La _{0.95} Sr _{0.05} F _{2.95}	F ⁻	3.0×10^{-5}	Single crystal + high-energy ball-milling + sintering	[121]
β -PbSnF ₄	F ⁻	1.20×10^{-3}	Sintering + mixing	[122, 123]
Sm _{0.95} Ca _{0.05} F _{2.95}	F ⁻	1.0×10^{-4}	Sintering + solid state synthesis + mixing	[85]
Ce _{0.975} Sr _{0.025} F _{2.975}	F ⁻	3.0×10^{-4}	Sintering + solid state synthesis + mixing	[86]
Ba _{0.6} La _{0.4} F _{2.4}	F ⁻	5.0×10^{-6}	Annealing + solid-state synthesis + mixing	[124][101]
CaF ₂ (humidified)	F ⁻	1.88×10^{-5}	Humidifying + ball-milling	[125][I]
Sm _{0.95} Ca _{0.05} F _{2.95}	F ⁻	1.0×10^{-4}	Solid-state synthesis (high-energy ball-milling)	[126][II]
Pb _{0.55} Sn _{0.45} F ₂	F ⁻	2.53×10^{-3}	High-energy ball-milling method	[127][III]

According to our data, more effort should be addressed to the following issues:

- ❖ The electrolyte was often not sufficiently in contact with the electrode material in our battery assembly trials, leading to short circuits or detachments from the electrodes. Improvement of the mechanical manufacturing mechanism is needed.
- ❖ The electrode/electrolyte contact was further weakened during the cycling process if the electrode materials experience significant volume changes. In order to resolve this problem, an electrode may need suitable additives like binders or flexible

electrolytes and separators. Another big challenge is the conductivity of the cathode composite. An improved solid fluoride-ion conductor within the range of $10^{-3} - 10^{-4} \text{ S}\cdot\text{cm}^{-1}$ at RT would further improve the FIB capacity and cycling behavior.

This thesis opens up an unexplored and promising road of research within the field of solid electrolyte fluoride materials and entire battery cells. It means that new battery chemistries and battery systems could be well developed that will complement, if not revolutionize, the rechargeable battery field, providing reassuring levels of safety, moderate costs, high energy density levels, good static and dynamic stabilities, and long cycle lives with practically no self-discharge.

References

- [1] M. Anji Reddy and M. Fichtner, "Batteries based on fluoride shuttle," *J. Mater. Chem.*, vol. 21, no. 43, pp. 17059–17062, 2011.
- [2] N. Yabuuchi, K. Kubota, M. Dahbi, and S. Komaba, "Research Development on Sodium-Ion Batteries," *Chem. Rev.*, vol. 114, no. 23, pp. 11636–11682, 2014.
- [3] F. Gschwind, H. Euchner, and G. Rodriguez-Garcia, "Chloride Ion Battery Review: Theoretical Calculations, State of the Art, Safety, Toxicity, and an Outlook towards Future Developments," *European Journal of Inorganic Chemistry*, vol. 2017, no. 21, pp. 2784–2799, 2017.
- [4] Y. Shao et al., "Highly reversible Mg insertion in nanostructured Bi for Mg ion batteries," *Nano Lett.*, vol. 14, no. 1, pp. 255–260, 2014.
- [5] R. J. Gummow, G. Vamvounis, M. B. Kannan, and Y. He, "Calcium-Ion Batteries: Current State-of-the-Art and Future Perspectives," *Adv. Mater.*, vol. 30, no. 39, p. 1801702, Sep. 2018.
- [6] S. K. Das, S. Mahapatra, and H. Lahan, "Aluminium-ion batteries: developments and challenges," *Journal of Materials Chemistry A*, vol. 5, no. 14, pp. 6347–6367, 2017.
- [7] C. Rongeat, M. A. Reddy, R. Witter, and M. Fichtner, "Nanostructured fluoride-type fluorides as electrolytes for fluoride ion batteries," *J. Phys. Chem. C*, vol. 117, no. 10, pp. 4943–4950, 2013.
- [8] C. Rongeat, M. Anji Reddy, R. Witter, and M. Fichtner, "Solid electrolytes for fluoride ion batteries: Ionic conductivity in polycrystalline tysonite-type fluorides," *ACS Appl. Mater. Interfaces*, vol. 6, no. 3, pp. 2103–2110, 2014.
- [9] H. Konishi, T. Minato, T. Abe, and Z. Ogumi, "Electrochemical Performance of a Bismuth Fluoride Electrode in a Reserve-Type Fluoride Shuttle Battery," *J. Electrochem. Soc.*, vol. 164, no. 14, pp. A3702–A3708, 2017.
- [10] V. K. Davis et al., "Room-temperature cycling of metal fluoride electrodes: Liquid electrolytes for high-energy fluoride ion cells," *Science (80-.)*, vol. 362, no. 6419, pp. 1144–1148, 2018.
- [11] Zhang, Le (2017): Development of all solid state fluoride ion batteries based on thin film electrolytes. Open Access Repository der Universität Ulm. Dissertation. <http://dx.doi.org/10.18725/OPARU-4272>.
- [12] I. Mohammad, R. Witter, M. Fichtner, and M. Anji Reddy, "Room-Temperature, Rechargeable Solid-State Fluoride-Ion Batteries," *ACS Appl. Energy Mater.*, vol. 1, no. 9, pp. 4766–4775, 2018.
- [13] A. Malhotra, B. Battke, M. Beuse, A. Stephan, and T. Schmidt, "Use cases for stationary battery technologies: A review of the literature and existing projects," *Renewable and Sustainable Energy Reviews*, vol. 56, pp. 705–721, 2016.
- [14] C. Daniel and J. O. Besenhard, *Handbook of Battery Materials: Second Edition*. Wiley-VCH Verlag GmbH & Co. KGaA, DOI:10.1002/9783527637188, 2011.
- [15] M. Armand and J.-M. Tarascon, "Building better batteries," *Nature*, vol. 451, no. 7179, pp. 652–657, 2008.
- [16] X. Judez, G. G. Eshetu, C. Li, L. M. Rodriguez-Martinez, H. Zhang, and M. Armand, "Opportunities for Rechargeable Solid-State Batteries Based on Li-Intercalation Cathodes," *Joule*, vol. 2, no. 11, pp. 2208–2224, 2018.
- [17] J. M. Tarascon and M. Armand, "Issues and challenges facing rechargeable lithium batteries," *Nature*, vol. 414, no. 6861, pp. 359–67, 2001.

- [18] N. Kamaya et al., "A lithium superionic conductor," *Nat. Mater.*, vol. 10, no. 9, pp. 682–686, 2011.
- [19] A. Hayashi, K. Noi, A. Sakuda, and M. Tatsumisago, "Superionic glass-ceramic electrolytes for room-temperature rechargeable sodium batteries," *Nat. Commun.*, vol. 3, p. 856, 2012.
- [20] L. Zhang, M. Anji Reddy, and M. Fichtner, "Development of tysonite-type fluoride conducting thin film electrolytes for fluoride ion batteries," *Solid State Ionics*, vol. 272, pp. 39–44, 2015.
- [21] A. Hamnett, "The components of an electrochemical cell," in *Handbook of Fuel Cells*, (eds W. Vielstich, A. Lamm, H. A. Gasteiger and H. Yokokawa). John Wiley and Sons, doi:10.1002/9780470974001.f101001, 2010.
- [22] D. COLLINS, *Handbook of batteries and fuel cells* By David Linden, published by McGraw-Hill Book Company GmbH., Hamburg, F.R.G., 1984; 1024 pp.; price DM 258.80., vol. 17, no. 4. 1986.
- [23] Z. J. Zhang, P. Ramadass, and W. Fang, "Safety of Lithium-Ion Batteries," in *Lithium-Ion Batteries: Advances and Applications*, 2014, pp. 409–435.
- [24] M. M. Biswas, M. S. Azim, T. K. Saha, U. Zobayer, and M. C. Urmi, "Towards Implementation of Smart Grid: An Updated Review on Electrical Energy Storage Systems," *Smart Grid Renew. Energy*, vol. 04, no. 01, pp. 122–132, 2013.
- [25] "CRC handbook of thermophysical and thermochemical data," *Choice Rev. Online*, vol. 32, no. 09, pp. 32-5143-32–5143, 1995.
- [26] B. C. Tofield, R. M. Dell, and J. Jensen, "Advanced batteries," *Nature*, vol. 276, no. 5685. pp. 217–220, 1978.
- [27] R. A. Huggins, *Advanced batteries: Materials science aspects*. *Journal of Solid State Electrochemistry* 17(8), DOI: 10.1007/s10008-013-2093-4, 2009.
- [28] A. L. M. Reddy, S. R. Gowda, M. M. Shaijumon, and P. M. Ajayan, "Hybrid nanostructures for energy storage applications," *Advanced Materials*, vol. 24, no. 37. pp. 5045–5064, 2012.
- [29] H. Kim et al., "Recent Progress in Electrode Materials for Sodium-Ion Batteries," *Advanced Energy Materials*, vol. 6, no. 19. 2016.
- [30] R. Funahashi et al., "Development of thermoelectric technology from materials to generators," in *Advanced Materials for Clean Energy*, 2015, pp. 83–142.
- [31] X. Zhao, S. Ren, M. Bruns, and M. Fichtner, "Chloride ion battery: A new member in the rechargeable battery family," *J. Power Sources*, vol. 245, pp. 706–711, 2014.
- [32] X. Zhao, Z. Zhao-Karger, D. Wang, and M. Fichtner, "Metal oxychlorides as cathode materials for chloride ion batteries," *Angew. Chemie - Int. Ed.*, vol. 52, no. 51, pp. 13621–13624, 2013.
- [33] I. Mohammad, R. Witter, M. Fichtner, and M. A. Reddy, "Introducing Interlayer Electrolytes: Toward Room-Temperature High-Potential Solid-State Rechargeable Fluoride Ion Batteries," *ACS Appl. Energy Mater.*, vol. 2, no. 2, pp. 1553–1562, Jan. 2019.
- [34] A. Eftekhari, "Erratum: Potassium secondary cell based on Prussian blue cathode," *Journal of Power Sources*, vol. 136, no. 1. p. 201, 2004.
- [35] M. P. Paranthaman, H. Liu, X. G. Sun, S. Dai, and G. M. Brown, "Aluminum-ion batteries for medium-and large-scale energy storage," in *Advances in Batteries for Medium and Large-Scale Energy Storage: Types and Applications*, 2014, pp. 463–474.

- [36] J. Kim, D. J. Lee, H. G. Jung, Y. K. Sun, J. Hassoun, and B. Scrosati, "An advanced lithium-sulfur battery," *Adv. Funct. Mater.*, vol. 23, no. 8, pp. 1076–1080, 2013.
- [37] Y. Shao-Horn, L. Croguennec, C. Delmas, E. C. Nelson, and M. A. O'Keefe, "Atomic resolution of lithium ions in LiCoO_2 ," *Nat. Mater.*, vol. 2, no. 7, pp. 464–467, 2003.
- [38] J. B. Goodenough and Y. Kim, "Challenges for rechargeable batteries," *J. Power Sources*, vol. 196, no. 16, pp. 6688–6694, 2011.
- [39] V. Etacheri, R. Marom, R. Elazari, G. Salitra, and D. Aurbach, "Challenges in the development of advanced Li-ion batteries: A review," *Energy Environ. Sci.*, vol. 4, no. 9, pp. 3243–3262, 2011.
- [40] B. Scrosati and J. Garche, "Lithium batteries: Status, prospects and future," *Journal of Power Sources*, vol. 195, no. 9, pp. 2419–2430, 2010.
- [41] N. Nitta, F. Wu, J. T. Lee, and G. Yushin, "Li-ion battery materials: Present and future," *Mater. Today*, vol. 18, no. 5, pp. 252–264, 2015.
- [42] J. B. Goodenough and K. S. Park, "The Li-ion rechargeable battery: A perspective," *Journal of the American Chemical Society*, vol. 135, no. 4, pp. 1167–1176, 2013.
- [43] C. Liu, F. Li, M. Lai-Peng, and H. M. Cheng, "Advanced materials for energy storage," *Adv. Mater.*, vol. 22, no. 8, pp. E28–E62, 2010.
- [44] B. Nykvist and M. Nilsson, "Rapidly falling costs of battery packs for electric vehicles," *Nat. Clim. Chang.*, vol. 5, no. 4, pp. 329–332, 2015.
- [45] R. Van Noorden, "The rechargeable revolution: A better battery," *Nature*, vol. 507, no. 7490, pp. 26–28, 2014.
- [46] R. Yazami, "Surface chemistry and lithium storage capability of the graphite-lithium electrode," *Electrochim. Acta*, vol. 45, no. 1, pp. 87–97, 1999.
- [47] R. Hausbrand et al., "Fundamental degradation mechanisms of layered oxide Li-ion battery cathode materials: Methodology, insights and novel approaches," *Mater. Sci. Eng. B Solid-State Mater. Adv. Technol.*, vol. 192, no. C, pp. 3–25, 2015.
- [48] J. K. Park, *Principles and Applications of Lithium Secondary Batteries*. Wiley-VCH Verlag GmbH & Co. KGaA, DOI:10.1002/9783527650408, 2012.
- [49] X. Zhao et al., "Magnesium anode for chloride ion batteries," *ACS Appl. Mater. Interfaces*, vol. 6, no. 14, pp. 10997–11000, 2014.
- [50] P. Gao, X. Zhao, Z. Zhao-Karger, T. Diemant, R. J. Behm, and M. Fichtner, "Vanadium oxychloride/magnesium electrode systems for chloride ion batteries," *ACS Appl. Mater. Interfaces*, vol. 6, no. 24, pp. 22430–22435, 2014.
- [51] F. Chen, Z. Y. Leong, and H. Y. Yang, "An aqueous rechargeable chloride ion battery," *Energy Storage Mater.*, vol. 7, pp. 189–194, 2017.
- [52] X. Zhao, Z. Zhao, M. Yang, H. Xia, T. Yu, and X. Shen, "Developing polymer cathode material for the chloride ion battery," *ACS Appl. Mater. Interfaces*, vol. 9, no. 3, pp. 2535–2540, 2017.
- [53] D. Wang, G. Cao, R. Massé, E. Uchaker, and G. Cao, "Beyond Li Ion: Electrode Materials for Sodium and Magnesium-Ion Batteries," *Nanomater. Energy Convers. Storage*, pp. 639–755, 2017.
- [54] N. Singh, T. S. Arthur, C. Ling, M. Matsui, and F. Mizuno, "A high energy-density tin anode for rechargeable magnesium-ion batteries," *Chem. Commun.*, vol. 49, no. 2, pp. 149–151, 2013.
- [55] P. J. S. Foot, "Principles and prospects of high-energy magnesium-ion batteries," *Sci. Prog.*, vol. 98, no. 3, pp. 264–275, 2015.

- [56] R. Mohtadi and F. Mizuno, "Magnesium batteries: Current state of the art, issues and future perspectives," *Beilstein Journal of Nanotechnology*, vol. 5, no. 1. pp. 1291–1311, 2014.
- [57] P. Bian, Y. Nuli, Z. Abudoureyimu, J. Yang, and J. Wang, "A novel thiolate-based electrolyte system for rechargeable magnesium batteries," *Electrochim. Acta*, vol. 121, pp. 258–263, 2014.
- [58] B. L. Ellis and L. F. Nazar, "Sodium and sodium-ion energy storage batteries," *Current Opinion in Solid State and Materials Science*, vol. 16, no. 4. pp. 168–177, 2012.
- [59] M. D. Slater, D. Kim, E. Lee, and C. S. Johnson, "Sodium-ion batteries," *Adv. Funct. Mater.*, vol. 23, no. 8, pp. 947–958, 2013.
- [60] N. Yabuuchi, K. Kubota, M. Dahbi, and S. Komaba, "Research Development on Sodium-Ion Batteries," *Chemical Reviews*, vol. 114, no. 23. pp. 11636–11682, 2014.
- [61] P. Barpanda, G. Oyama, S. I. Nishimura, S. C. Chung, and A. Yamada, "A 3.8-V earth-abundant sodium battery electrode," *Nat. Commun.*, vol. 5, 2014.
- [62] Y. Cao et al., "Sodium ion insertion in hollow carbon nanowires for battery applications," *Nano Lett.*, vol. 12, no. 7, pp. 3783–3787, 2012.
- [63] W. Luo, F. Shen, C. Bommier, H. Zhu, X. Ji, and L. Hu, "Na-Ion Battery Anodes: Materials and Electrochemistry," *Acc. Chem. Res.*, vol. 49, no. 2, pp. 231–240, 2016.
- [64] J. Sun et al., "A phosphorene-graphene hybrid material as a high-capacity anode for sodium-ion batteries," *Nat. Nanotechnol.*, vol. 10, no. 11, pp. 980–985, 2015.
- [65] J. Y. Hwang, S. T. Myung, and Y. K. Sun, "Sodium-ion batteries: Present and future," *Chemical Society Reviews*, vol. 46, no. 12. pp. 3529–3614, 2017.
- [66] A. Rudola, K. Saravanan, C. W. Mason, and P. Balaya, "Na₂Ti₃O₇: An intercalation based anode for sodium-ion battery applications," *J. Mater. Chem. A*, vol. 1, no. 7, pp. 2653–2662, 2013.
- [67] K. Shiva, P. Singh, W. Zhou, and J. B. Goodenough, "NaFe₂PO₄(SO₄)₂: A potential cathode for a Na-ion battery," *Energy Environ. Sci.*, vol. 9, no. 10, pp. 3103–3106, 2016.
- [68] R. B. Araujo, S. Chakraborty, P. Barpanda, and R. Ahuja, "Na₂M₂(SO₄)₃ (M = Fe, Mn, Co and Ni): towards high-voltage sodium battery applications," *Phys. Chem. Chem. Phys.*, vol. 18, no. 14, pp. 9658–9665, 2016.
- [69] L. Xue et al., "Low-Cost High-Energy Potassium Cathode," *J. Am. Chem. Soc.*, vol. 139, no. 6, pp. 2164–2167, 2017.
- [70] A. Ponrouch, C. Frontera, F. Bardé, and M. R. Palacín, "Towards a calcium-based rechargeable battery," *Nat. Mater.*, vol. 15, no. 2, pp. 169–172, 2016.
- [71] X. Zhang, Y. Tang, F. Zhang, and C.-S. Lee, "A Novel Aluminum-Graphite Dual-Ion Battery," *Adv. Energy Mater.*, vol. 6, no. 11, p. 1502588, 2016.
- [72] C. Xu, Y. Chen, S. Shi, J. Li, F. Kang, and D. Su, "Secondary batteries with multivalent ions for energy storage," *Sci. Rep.*, vol. 5, 2015.
- [73] D. T. Thieu et al., "CuF₂ as Reversible Cathode for Fluoride Ion Batteries," *Adv. Funct. Mater.*, vol. 27, no. 31, 2017.
- [74] C. Rongeat, M. Anji Reddy, T. Diemant, R. J. Behm, and M. Fichtner, "Development of new anode composite materials for fluoride ion batteries," *J. Mater. Chem. A*, vol. 2, no. 48, pp. 20861–20872, 2014.

- [75] M. A. Nowroozi, K. Wissel, J. Rohrer, A. R. Munnangi, and O. Clemens, "LaSrMnO₄: Reversible Electrochemical Intercalation of Fluoride Ions in the Context of Fluoride Ion Batteries," *Chem. Mater.*, vol. 29, no. 8, pp. 3441–3453, 2017.
- [76] A. Grenier et al., "Solid Fluoride Electrolytes and Their Composite with Carbon: Issues and Challenges for Rechargeable Solid State Fluoride-Ion Batteries," *J. Phys. Chem. C*, vol. 121, no. 45, pp. 24962–24970, 2017.
- [77] F. Gschwind et al., "Fluoride ion batteries: Theoretical performance, safety, toxicity, and a combinatorial screening of new electrodes," *Journal of Fluorine Chemistry*, vol. 182, pp. 76–90, 2016.
- [78] C. Rongeat, M. Anji Reddy, R. Witter, and M. Fichtner, "Solid electrolytes for fluoride ion batteries: Ionic conductivity in polycrystalline tysonite-type fluorides," *ACS Appl. Mater. Interfaces*, vol. 6, no. 3, pp. 2103–2110, 2014.
- [79] H. Bhatia et al., "Conductivity Optimization of Tysonite-type La_{1-x}Ba_xF_{3-x} Solid Electrolytes for Advanced Fluoride Ion Battery," *ACS Appl. Mater. Interfaces*, vol. 9, no. 28, pp. 23707–23715, 2017.
- [80] J. Chable et al., "Fluoride solid electrolytes: From microcrystalline to nanostructured tysonite-type La_{0.95}Ba_{0.05}F_{2.95}," *J. Alloys Compd.*, vol. 692, pp. 980–988, 2017.
- [81] M. M. Ahmad, Y. Yamane, and K. Yamada, "The ionic conductivity and dielectric properties of Ba_{1-x}Sn_xF₂ solid solutions prepared by mechanochemical milling," *Mater. Sci. Eng. B Solid-State Mater. Adv. Technol.*, vol. 178, no. 15, pp. 965–970, 2013.
- [82] B. M. Voronin and S. V. Volkov, "Ionic conductivity of fluorite type crystals CaF₂, SrF₂, BaF₂, and SrCl₂ at high temperatures," *J. Phys. Chem. Solids*, vol. 62, no. 7, pp. 1349–1358, 2001.
- [83] P. P. Fedorov, T. M. Turkina, B. P. Sobolev, E. Mariani, and M. Svantner, "Ionic conductivity in the single crystals of non-stoichiometric fluorite phases M_{1-x}R_xF_{2+x} (M=Ca, Sr, Ba; R=Y, La-Lu)," *Solid State Ionics*, vol. 6, no. 4, pp. 331–335, 1982.
- [84] B. P. Sobolev et al., "Mechanochemical synthesis of nonstoichiometric nanocrystals La_{1-y}Ca_yF_{3-y} with a tysonite structure and nanoceramic materials from CaF₂ and LaF₃ crystals," *Crystallogr. Reports*, vol. 53, no. 5, pp. 868–880, 2008.
- [85] B. Dieudonné et al., "Exploring the Sm_{1-x}Ca_xF_{3-x} Tysonite Solid Solution as a Solid-State Electrolyte: Relationships between Structural Features and F⁻ Ionic Conductivity," *J. Phys. Chem. C*, vol. 119, no. 45, pp. 25170–25179, 2015.
- [86] B. Dieudonné et al., "The key role of the composition and structural features in fluoride ion conductivity in tysonite Ce_{1-x}Sr_xF_{3-x} solid solutions," *Dalt. Trans.*, vol. 46, no. 11, pp. 3761–3769, 2017.
- [87] C. Suryanarayana, "Mechanical alloying and milling," *Progress in Materials Science*, vol. 46, no. 1–2, pp. 1–184, 2001.
- [88] M. A. Rahman, X. Wang, and C. Wen, "High Energy Density Metal-Air Batteries: A Review," *J. Electrochem. Soc.*, vol. 160, no. 10, pp. A1759–A1771, 2013.
- [89] R. Janot and D. Guérard, "Ball-milling in liquid media: Applications to the preparation of anodic materials for lithium-ion batteries," *Prog. Mater. Sci.*, vol. 50, no. 1, pp. 1–92, 2005.
- [90] A. Stolle, T. Szuppa, S. E. S. Leonhardt, and B. Ondruschka, "Ball milling in organic synthesis: Solutions and challenges," *Chemical Society Reviews*, vol. 40, no. 5, pp. 2317–2329, 2011.

- [91] M. Aziz and A. F. Ismail, "X-Ray Photoelectron Spectroscopy (XPS)," in *Membrane Characterization*, 2017, pp. 81–93.
- [92] S. Tanuma, C. J. Powell, and D. R. Penn, "Calculations of electron inelastic mean free paths. V. Data for 14 organic compounds over the 50–2000 eV range," *Surf. Interface Anal.*, vol. 21, no. 3, pp. 165–176, 1994.
- [93] F. Mansfeld, "Electrochemical impedance spectroscopy (EIS) as a new tool for investigating methods of corrosion protection," 1990.
- [94] S. Breuer and M. Wilkening, "Mismatch in cation size causes rapid anion dynamics in solid electrolytes: The role of the Arrhenius pre-factor," *Dalt. Trans.*, vol. 47, no. 12, pp. 4105–4117, 2018.
- [95] M. Abdellatif, M. Abele, M. Leoni, and P. Scardi, "Combined X-ray diffraction and solid-state ^{19}F magic angle spinning NMR analysis of lattice defects in nanocrystalline CaF_2 ," *J. Appl. Crystallogr.*, vol. 46, no. 4, pp. 1049–1057, 2013.
- [96] D. W. Chang, H. J. Choi, I. Y. Jeon, J. M. Seo, L. Dai, and J. B. Baek, "Solvent-free mechanochemical reduction of graphene oxide," *Carbon N. Y.*, vol. 77, pp. 501–507, 2014.
- [97] L. N. Patro and K. Hariharan, "Fast fluoride ion conducting materials in solid state ionics: An overview," *Solid State Ionics*, vol. 239, pp. 41–49, 2013.
- [98] A. Sakuda, A. Hayashi, and M. Tatsumisago, "Sulfide solid electrolyte with favorable mechanical property for all-solid-state lithium battery," *Sci. Rep.*, vol. 3, 2013.
- [99] R. Ramachandran, D. Johnson-Mcdaniel, and T. T. Salguero, "Formation and Scrolling Behavior of Metal Fluoride and Oxyfluoride Nanosheets," *Chem. Mater.*, vol. 28, no. 20, pp. 7257–7267, 2016.
- [100] M. Heise, G. Scholz, A. Düvel, P. Heitjans, and E. Kemnitz, "Mechanochemical synthesis, structure and properties of lead containing alkaline earth metal fluoride solid solutions $\text{M}_x\text{Pb}_{1-x}\text{F}_2$ (M = Ca, Sr, Ba)," *Solid State Sci.*, vol. 77, pp. 45–53, 2018.
- [101] M. Heise, G. Scholz, A. Düvel, P. Heitjans, and E. Kemnitz, "Mechanochemical synthesis, structure, and properties of solid solutions of alkaline earth metal fluorides: $\text{Ma}_{1-x}\text{Mb}_x\text{F}_2$ (M: Ca, Sr, Ba)," *Solid State Sci.*, vol. 60, pp. 65–74, 2016.
- [102] B. P. Sobolev, N. I. Sorokin, and N. B. Bolotina, "Nonstoichiometric Single Crystals $\text{M}_{1-x}\text{R}_x\text{F}_{2+x}$ and $\text{R}_{1-y}\text{M}_y\text{F}_{3-y}$ (M [Ca, Sr, Ba]: R [Rare Earth Elements]) as Fluorine-Ionic Conductive Solid Electrolytes," in *Photonic and Electronic Properties of Fluoride Materials: Progress in Fluorine Science Series*, 2016, pp. 465–491.
- [103] F. Gschwind and J. Bastien, "Parametric investigation of room-temperature fluoride-ion batteries: Assessment of electrolytes, Mg-based anodes, and BiF_3 -cathodes," *J. Mater. Chem. A*, vol. 3, no. 10, pp. 5628–5634, 2015.
- [104] N. I. Sorokin, E. A. Krivandina, Z. I. Zhmurova, B. P. Sobolev, M. V. Fominykh, and V. V. Fistul', "Superionic conductivity of the heterovalent solid solutions $\text{R}_{1-x}\text{M}_x\text{F}_{3-x}$ (R=REE, M=Ca, Ba) with tysonite-type structure," *Phys. Solid State*, vol. 41, no. 4, pp. 573–575, 2002.
- [105] B. Ruprecht, M. Wilkening, S. Steuernagel, and P. Heitjans, "Anion diffusivity in highly conductive nanocrystalline $\text{BaF}_2:\text{CaF}_2$ composites prepared by high-energy ball milling," *J. Mater. Chem.*, vol. 18, no. 44, pp. 5412–5416, 2008.
- [106] J. Chable et al., "Fluoride solid electrolytes: investigation of the tysonite-type solid solutions $\text{La}_{1-x}\text{Ba}_x\text{F}_{3-x}$ ($x < 0.15$)," *Dalt. Trans.*, vol. 44, no. 45, pp. 19625–19635, 2015.

- [107] A. Roos, F. C. M. van de Pol, R. Keim, and J. Schoonman, "Ionic conductivity in tysonite-type solid solutions $\text{La}_{1-x}\text{Ba}_x\text{F}_{3-x}$," *Solid State Ionics*, vol. 13, no. 3, pp. 191–203, 1984.
- [108] M. Hammad Fawey et al., "*In situ* TEM studies of micron-sized all-solid-state fluoride ion batteries: Preparation, prospects, and challenges," *Microsc. Res. Tech.*, vol. 79, no. 7, pp. 615–624, 2016.
- [109] W. Puin, S. Rodewald, R. Ramlau, P. Heitjans, and J. Maier, "Local and overall ionic conductivity in nanocrystalline CaF_2 ," *Solid State Ionics*, vol. 131, no. 1, pp. 159–164, 2000.
- [110] J. Portier, J. M. Reau, S. Matar, J. L. Soubeyroux, and P. Hagemuller, "Advances on fluorine ion conductors, basic and applied research," *Solid State Ionics*, vol. 11, no. 1, pp. 83–90, 1983.
- [111] M. A. Reddy and M. Fichtner, "Ionic Conductivity of Nanocrystalline Metal Fluorides," in *Photonic and Electronic Properties of Fluoride Materials: Progress in Fluorine Science Series*, 2016, pp. 449–463.
- [112] J. Janek, M. Martin, and K. D. Becker, "Physical chemistry of solids - The science behind materials engineering," *Phys. Chem. Chem. Phys.*, vol. 11, no. 17, p. 3010, 2009.
- [113] A. Grenier, A. G. Porras Gutierrez, H. Groult, and D. Dambournet, "Modified coin cells to evaluate the electrochemical properties of solid-state fluoride-ion batteries at 150 °C," *J. Fluor. Chem.*, vol. 191, pp. 23–28, 2016.
- [114] V. Y. Kavun et al., "NMR and impedance spectroscopy data on the ionic mobility and conductivity in PbSnF_4 doped with alkali metal fluoride," *J. Struct. Chem.*, vol. 53, no. 2, pp. 290–294, 2012.
- [115] M. Murakami, Y. Morita, and M. Mizuno, " $^{19}\text{F}/^{119}\text{Sn}/^{207}\text{Pb}$ NMR Studies on Ion Dynamics in Tetragonal PbSnF_4 : Spectroscopic Evidence for Defect-Driven Conductivity," *J. Phys. Chem. C*, vol. 121, no. 5, pp. 2627–2634, 2017.
- [116] R. Witter, I. Mohammad, P. Molaiyan, and S. Kumar, "A method for manufacturing a nanoparticle material and a fluoride ion battery.," 07-Mar-2019.
- [117] Z. Zhang et al., "New horizons for inorganic solid state ion conductors," *Energy and Environmental Science*, vol. 11, no. 8, pp. 1945–1976, 2018.
- [118] A. Roos and J. Schoonman, "Electronic conductivity in $\text{La}_{1-x}\text{Ba}_x\text{F}_{3-x}$ crystals," *Solid State Ionics*, vol. 13, no. 3, pp. 205–211, 1984.
- [119] F. Fujara, D. Kruk, O. Lips, A. F. Privalov, V. Sinitsyn, and H. Stork, "Fluorine dynamics in LaF_3 -type fast ionic conductors - Combined results of NMR and conductivity techniques," *Solid State Ionics*, vol. 179, no. 40, pp. 2350–2357, 2008.
- [120] B. P. Sobolev et al., "Mechanochemical synthesis of nonstoichiometric fluoride $\text{Ca}_{1-x}\text{La}_x\text{F}_{2+x}$ nanocrystals from CaF_2 and LaF_3 single crystals," *Crystallogr. Reports*, vol. 50, no. 3, pp. 478–485, 2005.
- [121] N. I. Sorokin and B. P. Sobolev, "Frequency response of the low-temperature ionic conductivity of single crystals $\text{R}_{1-y}\text{M}_y\text{F}_{3-y}$ (R = La-Er; M = Ca, Sr, Ba, Cd)," *Phys. Solid State*, vol. 50, no. 3, pp. 416–421, 2008.
- [122] V. Trnovcová, P. P. Fedorov, and I. Furár, "Fluoride solid electrolytes containing rare earth elements," *J. Rare Earths*, vol. 26, no. 2, pp. 225–232, 2008.
- [123] V. Trnovcová, P. P. Fedorov, and I. Furár, "Fluoride solid electrolytes," *Russ. J. Electrochem.*, vol. 45, no. 6, pp. 630–639, 2009.

- [124] B. P. Sobolev, A. M. Golubev, and P. Herrero, "Fluorite $M_{1-x}R_xF_{2+x}$ phases (M = Ca, Sr, Ba; R = rare earth elements) as nanostructured materials," *Crystallogr. Reports*, vol. 48, no. 1, pp. 141–161, 2003.
- [125] P. Molaiyan and R. Witter, "Surface defect-enhanced conductivity of calcium fluoride for electrochemical applications," *Mater. Des. Process. Commun.*, vol. 0, no. ja, p. e44, 2019.
- [126] P. Molaiyan and R. Witter, "Mechanochemical synthesis of solid-state electrolyte $Sm_{1-x}Ca_xF_{3-x}$ for batteries and other electrochemical devices," *Mater. Lett.*, vol. 244, pp. 22–26, 2019.
- [127] P. Molaiyan and R. Witter, "Crystal phase and surface defect driven synthesis of $Pb_{1-x}Sn_xF_2$ solid solution electrolyte for fluoride ion batteries," *J. Electroanal. Chem.* 2019, vol. 845, pp. 154–159.
- [128] P. Molaiyan and R. Witter; CaF_2 Solid-State Electrolytes Prepared by Vapor Pressure Exposure and Solid Synthesis for Defect and Ionic Conductivity Tuning. *Material Design and Processing Communications*. 2019, e76, <https://doi.org/10.1002/mdp2.76>.

Acknowledgments

I want to express my sincerest gratitude to the supervisor, Associate Professor Dr. Raiker Witter, and Co-Supervisor Prof. Ago Samoson for their guidance, support, and motivation throughout the years of doctoral study.

I want to thank Professor Kalju Meigas, Director of the School of Information Technologies: Department of Health Technologies, Tallinn University of Technology, Tallinn, Estonia, for giving me the possibility to carry out this doctoral thesis. I sincerely appreciate the learning opportunities and experimental support and apparatus provided by NMRI, Estonia.

I want to sincerely thank Professor Harry Hoster, Director of Energy research institute, Lancaster University, United Kingdom. For allowing me to carry out my research at the Solid State Chemistry group under the guidance of Dr. Nuria Tapia Ruiz for six months, I am very grateful. Also, I want to thank Ms. Cindy Soares, Mr. Christos Gouroyannis, and Mr. Alex Haslam, for their assistance at Lancaster University, UK.

I want to thank all my colleagues who took part in this study for sharing their time and ideas and for assisting me with the experiments. I have learned much through our conversations. In particular, I want to thank Mr. Irshad Mohammed, Mr. Meelis Rohtmäe, Mr. Andres Oss, Dr. Kalju Vanatalu, Ms. Steffi Witter and Mr. Rainer Nõlvak, Ms. Viia Roosaar for their assistance during my doctoral study.

I also thank my friends (too many to list here but you know who you are!) for providing support and friendship that I needed. I would like to especially thank Ms. Külli Kittus for providing support motivating and helping me all the time.

Last, but not least, my family had to grudgingly learn to accept my separation from them and support for every day, both emotionally and financially: my love and gratitude for them can hardly be expressed in words. My deepest gratitude goes to my family for their unconditional support and encouragement during my studies.

I want to acknowledge the Estonian Research Council through PUT126 (Smart spinning) and PUT 1534 (Structural Biology of Viscous Systems), The European Union through the European Regional Development Fund (Dora Plus Action 1), European Social Fund for project MTT68 (“Microwave and Scale enhanced NMR of Micro-Drops, -Leaflets, Cells and Nanoparticles”) which made the establishment and basic work of the battery laboratory facility possible, and TUT state stipend.

Abstract

Solid-State Electrolytes for Fluoride-ion Batteries

Secondary batteries that employ solid-state electrolytes are considered safer than conventional, liquid electrolyte batteries, and can be composed and synthesized in a context-aware (environment, cost) manner. We used extensively a high-energy ball-milling as a syntheses method, which generates high temperatures only locally, at the point of impact, and can be thus scaled to industrial level in an energy saving manner.

Calcium fluoride is well available and biocompatible material. We managed to prepare calcium fluoride nano-powder with crystallite/particle size of 12/50 nm, pertaining an underlying cubic structure. The defect structure was enhanced by the application of water vapor-pressure exposure. Bulk and boundary ion mobilities were measured in a complementary manner by NMR diffusion and EIS. The ionic conductivity of $1.9 \times 10^{-5} \text{ S}\cdot\text{cm}^{-1}$ at room temperature demonstrates an increase of two orders of magnitude compared to an untreated material. The conductivity relies on fluoride surface interstitial defects with an activation energy of 0.35 eV.

CaF_2 based conductivity was also investigated in the matrix of SmF_3 lattice as $\text{Sm}_{1-x}\text{Ca}_x\text{F}_{3-x}$ ($0 \leq x \leq 0.15$). The samples had a tysonite-type structure with a crystallite size of around 10-20 nm and a particle size of around 50 nm. A doping level of 5% provided the best ionic conductivity $2.8 \times 10^{-5} \text{ S}\cdot\text{cm}^{-1}$ with an activation energy of 0.40 eV the at room temperature. A proof-of-principle solid-state fluoride-ion battery (FIB) based on a $\text{CeF}_3/\text{Sm}_{0.95}\text{Ca}_{0.05}\text{F}_{2.95}/\text{Bi}$ system was successfully assembled and assessed.

Another promising class of materials in the context of fluoride conduction is a layered fluorite $\text{Pb}_{1-x}\text{Sn}_x\text{F}_2$. We have prepared solid solutions (with $x = 0.4 - 0.6$) of the β -type cubic crystal structures, with crystallite size in the range 17-18 nm. The ionic conductivity determined with impedance spectroscopy reached the maximum at $x = 0.45$, giving a value of $2.5 \times 10^{-3} \text{ S}\cdot\text{cm}^{-1}$ at room temperature with an activation energy of 0.30 eV. The material was dominantly in the β -type crystal structure with abundant surface defects. This electrolyte was applied for principal functional testing in a solid fluoride-ion battery assembly comprising a Bi-cathode and CeF_3 -anode.

Overall, the new information, consistent with recent findings from other groups, does encourage the development of batteries based on solid-state fluoride type electrolytes. Our work demonstrated a principal alternative to the high-performance energy storage, also new versatile composition choices offering possibly a better compliance with environmental considerations compared to the present Li-ion generation of batteries.

Lühikokkuvõte

Tahked elektrolüüdid fluoriidioon akudele

Akusid, milles on kasutusel tahked elektrolüüdid, peetakse turvalisemaks kui seda on tavalised vedelektrolüütidega akud. Käesoleval ajal pälvib suurt tähelepanu edu tahkete elektrolüütide ioonjuhtivuse paremaks muutmises.

Kaltsiumfluoriid on üks laiemalt uuritud aineid, mis sobiks tahkefaasiliseks materjaliks akudes, kuid mis leiab samuti rakendust elektroonikas ja optikas. Meil õnnestus valmistada suurendatud defektide struktuuriga kaltsiumfluoriidi nano-pulbrit, rakendades veeauru rõhku ja sellele järgnevat kuulveskis kõrgenergiaga jahvatamist. Aururõhu all töödeldud proovidel mõõdeti toatemperatuuril ioonjuhtivuseks $1.9 \times 10^{-5} \text{ S}\cdot\text{cm}^{-1}$, mis on kaks suurusjärku kõrgem töötlemata materjalidega võrreldes. Juhtivus põhineb fluoriidi interstitsiaalsetel pinnadefektidel aktivatsioonienergiaga 0.35 eV. Materjale on iseloomustatud erinevatel meetoditel. Kaltsiumfluoriidelektrolüüt muutub nano-pulbriliseks aineks kristalliidi/partikli suurustega 12/50 nm, kuid säilitab oma kuubilise baas-struktuuri. Defektide struktuurid on suurenenud, nagu see on nähtav ja detailselt uuritav NMR ja EPR abil. NMR difusiooni eksperimentidest tuletatud lähenemine osutus väga väärtuslikuks komplementaarseks meetodiks EIS-le ja võimaldas kogu- ja äärejuhtivuste dekonvolutsiooni.

Et juhtivust veelgi tõsta, me legeerisime CaF_2 samaariumiga lisades SmF_3 ilma mingi eeltöötluseta. $\text{Sm}_{1-x}\text{Ca}_x\text{F}_{3-x}$ ($0 \leq x \leq 0.15$) proovid valmistati planetaarset tüüpi mehhanokeemilisel (kuulveskis kõrgenergia jahvatamise) meetodil. Uuriti struktuuri, morfoloogiat ja ionset juhtivust. Röntgendifraktsiooni (XRD) ning kõrglahutusega väljaemissiooni skaneeriv elektronmikroskoopia (FESEM) uuringud tuvastasid, et proovidel oli pindmiselt tüsoniit-struktuur, mis vastab nominaalsele koostisele kristalliitide suurusega ligikaudu 10-20 nm ja partiklite suurusega ligikaudu 50 nm. Toatemperatuuril oli parimal elektrolüüdil – $\text{Sm}_{0.95}\text{Ca}_{0.05}\text{F}_{2.95}$ – ioonne juhtivus ligikaudu $2.8 \times 10^{-5} \text{ S}\cdot\text{cm}^{-1}$ aktivatsioonienergiaga 0.40 eV. Viimaks, tööpõhimõtte tõestuseks testiti fluoriidioon akusid (FIB) $\text{CeF}_3/\text{Sm}_{0.95}\text{Ca}_{0.05}\text{F}_{2.95}/\text{Bi}$ - põhinevas elektrookeemilises süsteemis.

Teine huvitav klass materjale F juhtivuse kontekstis on kihiline $\text{Pb}_{1-x}\text{Sn}_x\text{F}_2$. Kasutades kõrge energiaga planetaarset kuulveskis jahvatamist oleme valmistanud β -tüüpi kristalse struktuuriga $\text{Pb}_{1-x}\text{Sn}_x\text{F}_2$ ($x = 0.4 - 0.6$) tahked lahused kristalliitide mõõtmega suurusjärgus 17-18 nm. Impedants-spektroskoopiaga määratud ioonjuhtivused jõudsid maksimumvärtuseni $x = 0.45$ juures olles $2.5 \times 10^{-3} \text{ S}\cdot\text{cm}^{-1}$ toatemperatuuril aktivatsioonienergiaga 0.30 eV. Materjali uuriti XRD, FESEM, TEM ja NMR abil, millest me tuvastasime dominantse β -tüüpi struktuuri kristalli pinna defektidega. Seda elektrolüüti kasutati Bi-katoodist ning CeF_3 -anoodist koosneva tahkefaasilise fluoriidioon aku printsiipiaalse funktsionaalsuse testimisel.

Käesolev uus teave julgustab arendama tahketel fluoriid-tüüpi elektrolüütidel baseeruvaid akusid.

Appendix

Publication I

P. Molaiyan and R. Witter; Surface defect-enhanced conductivity of calcium fluoride for electrochemical applications. *Material Design & Processing Communications*. 2019, vol. 1, Issue no. 4, August 2019. e44.

<https://doi.org/10.1002/mdp2.44> (Reproduced from ref.[125] with permission from John Wiley and Sons Publishing Group)

Surface defect-enhanced conductivity of calcium fluoride for electrochemical applications

Palanivel Molaiyan¹  | Raiker Witter^{1,2,3} 

¹School of Information Technologies, Tallinn University of Technology (TUT), Tallinn, Estonia

²Institute of Nanotechnology, Karlsruhe Institute of Technology (KIT), Karlsruhe, Germany

³Institute of Quantum Optics, University Ulm, Ulm, Germany

Correspondence

Raiker Witter, School of Information Technologies, Tallinn University of Technology (TUT), Akadeemia tee 15A, Tallinn 12618, Estonia.
Email: raiker.witter@mail.com

Funding information

Tallinna Tehnikaülikool; National Institute of Chemical Physics and Biophysics (KBFI); Karlsruhe Nano Micro Facility (KNMF); Karlsruhe Institute of Technology (KIT); Estonian Science Foundation (ESF), Grant/Award Numbers: PUT126 and PUT1534; European Social Fund, Grant/Award Number: MTT68

Abstract

Calcium fluoride is widely investigated known to be a promising solid material for optics, electronics, and electrochemistry. In this work, we report the successful preparation of calcium fluoride with enhanced defect structure obtained by the application of vapor pressure followed by high-energy ball milling, creating CaF₂ nano-powder, achieving increased ionic conductivities in the order of $1.9 \cdot 10^{-5} \text{ S}\cdot\text{cm}^{-1}$ at room temperature relying on fluoride surface interstitial defect with an activation energy of 0.35 eV. The materials were characterized by X-ray diffraction (XRD), scanning electron microscopy (SEM), electrochemical impedance spectroscopy (EIS), X-ray photoelectron spectroscopy (XPS), nuclear magnetic resonance (NMR), and electron paramagnetic resonance (EPR). It is revealed that the calcium fluoride electrolyte keeps in its basic cubic structure, becomes nano-powdered material with crystallite/particle size of 12/30 nm. Surface defect structures are enhanced, which is visible with XPS, NMR, and EPR spectroscopy. The synthesized material provided considerable ionic conductivity enhancement introducing attraction for electrochemical testing for fluoride-ion batteries (FIB).

KEYWORDS

ball milling, calcium fluoride, fluoride-ion battery, fluoride shuttle sensors, ionic conductivity, NMR, solid-state electrolyte

1 | INTRODUCTION

Calcium fluoride has been extensively studied related to infrared optical properties, losses in optical fibers, lenses, filters, laser hosts, and resonators.¹⁻³ Relevant interest remains to recognize and understand proper defect formation.⁴⁻⁹ It is applied to chemical sensors¹⁰ and gains importance for electronic applications.^{11,12} However, sustaining demand for high-power and high-energy-density battery systems has spurred extensive research in developing novel electrode and electrolyte materials for next-generation battery systems.¹³ Fluoride-ion batteries (FIB) seem to be a promising kind of candidate to enhance energy storage performance.¹⁴ With evolving new concepts of fluoride electrolytes such as LaF₃ doped by BaF₂^{15,16} and other materials^{17,18} (eg, PbF₂ and PbSnF₄),¹⁹ further investigations toward FIB are gaining attraction. Promising trends in applying solid electrolytes are triggered by succeeding to improve the electrical and electrochemical properties in solid state.¹³ All solid-state batteries are considered to be safe, because of the fact of reduced leakage, volatilization, or flammability, as they employ solid inorganic electrolytes rather than liquid or gel-like electrolytes.²⁰ To realize solid-state batteries that operate at ambient and moderate temperatures,²¹ improved F⁻-ion conductivities and close contact with active electrode materials are indispensable.²² Moreover, a reduction of the interparticle

resistance of electrolytes without high-temperature sintering or circumvention of layer thickness reduction by thin-film techniques was recommended for large-scale considerations.^{23,24} However, only a few highly conductive electrolytes suitable for room temperature operation of batteries have been reported.^{25,26}

Since FIBs are mostly based on metal fluorides, related materials have been actively investigated as candidates for solid electrolytes: alkaline-earth fluorides (fluorite-type structure),^{14,27} rare-earth fluorides (tysonite-type structure),²⁸ or lead-based fluorides¹⁹ are under investigation.²⁹ Creation of defect structures had been tested as for rare-earth (R = La – Lu, Sm)^{30,31} and alkaline-earth (M = Ca, Sr, Ba)³² metal fluorides to form $R_{1-x}M_xF_{3-x}$ introducing a stabilization of fluoride vacancies.²⁸ Different ionic radii of the alkaline earth cations ($Ba^{2+} > Sr^{2+} > Ca^{2+}$) as well as the rare-earth cations ($La^{3+} > \dots > Lu^{3+}$) influence the local environments of fluorine atoms and, consequently, their mobility.³³ Finally, lead-based fluorides possess suitable high conductivities but suffer under limited electrochemical stability.³⁴

In the case of fluorides, an increase of the anionic conductivity has been reported for nanocrystalline CaF_2 ³⁵ or CaF_2/BaF_2 nano-layers.³³ The preparation of nanocrystalline materials by ball milling has also lead to an improvement of the ionic conductivity of BaF_2 , CaF_2 , or SnF_2/PbF_2 composites.³⁶ In all cases, the conductivity increased, when the crystallite size decreased pointing at a conduction mechanism along the grain boundaries.³⁷ The improvement of the conductivity of CaF_2 has also been demonstrated by activating the grain boundaries using Lewis acids.³⁸ The conductivity of CaF_2 and BaF_2 could also be improved by mixing them with an insulator;³⁹ the doping of alkaline-earth fluorides by monovalent cations (Na, K) creating vacancies and trivalent cations (rare earth) creating interstitials has been reported.²⁰ The fluorite structure is somewhat open and can accommodate a relatively large amount of dopant.⁴⁰

Here, we present fluoride-type CaF_2 with surfaces stabilizing defect structure because of vapor-pressure treatment and high-energy ball milling.

2 | MATERIALS AND METHODS

2.1 | Sample preparation

CaF_2 (99%), KCl (99.9%), BiF_3 (99%), Mg powder (99%), and carbon black (99.9%) were purchased from Sigma-Aldrich. High-energy mechanical milling was used to synthesize nano-structured CaF_2 . Before milling, the CaF_2 powder was exposed to water vapor for 24 hours. The vapor was created by heating a saturated solution of KCl salt (50-mL distilled H_2O , 86% RH). The humidified CaF_2 was further ball milled for 18 hours at 600 rpm under vacuum. The ball-to-powder weight ratio was kept at 18:1. Silicon nitride jar (volume of 50 mL) and silicon nitride balls (5, 2, and 1 mm in diameter) were used. The ball milling was carried out using a planetary-type device (Tanchen powder, China).

The anode composite was prepared by milling Mg (40%), as prepared electrolyte CaF_2 (50%) and carbon black (10%). For the preparation of the cathode composite, BiF_3 (30%), as-prepared electrolyte CaF_2 (60%) and carbon black (10%), were used. For the preparation of electrodes, ball-to-powder weight ratio was fixed to 12:1.

2.2 | Structural and morphology characterization

The as-prepared samples were characterized by X-ray diffraction (XRD) using an AXS Bruker D5005 Advance instrument with Cu K α radiation ($\lambda_1 = 1.54056 \text{ \AA}$, $\lambda_2 = 1.544390 \text{ \AA}$) of variable slit. Profile-matching refinements were performed on the XRD patterns for cell parameters determination, using the Rietveld refinement method with the FullProf software.^{17,41} The microstructure of a cross section of the electrolyte and pressed pellet was investigated by a scanning electron microscope (SEM: JEOL, JSM-6610A) and a field emission SEM (FESEM: Carl Zeiss Ultra 55) with 4 kV of electron high tension (EHT) voltage and a width of 4 mm (magnification depth and backscattered electron [BSE] imaging performed at a short working distance [WD]: 1-mm WD).

2.3 | Electrochemical impedance spectroscopy

The as-prepared CaF_2 electrolyte was pressed applying a pellet press (Across International) under air atmosphere. Pellet thicknesses of around 1 mm at a diameter of 10 mm were obtained. They were gold coated on both sides using sputtering (JEOL, sputter coater) and were further investigated by impedance measurements with an Agilent 4192A

LF impedance analyzer within a frequency range from 5 Hz to 13 MHz with a voltage amplitude of 10 mV. The measured data were fitted by EC lab software with a common equivalent circuit.^{16,28}

2.4 | X-ray photoelectron spectroscopy

The X-ray photoelectron spectroscopy (XPS) measurements were performed using a K-Alpha+ XPS spectrometer (Thermo Fisher Scientific, East Grinstead, UK), and data acquisition and processing using the Thermo Advantage software which is described elsewhere.⁴² All samples were analyzed using a microfocused, monochromatic Al K α X-ray source (30- to 400- μ m spot size). The spectra were fitted with one or more Voigt profiles. For sharp peaks and peaks evidenced by the peak shape, the binding energy uncertainty was around ± 0.1 eV. In the case of weak peaks and no direct justification by the peak shape, the uncertainty was set to ± 0.2 eV. The analyzer transmission function, Scofield sensitivity factors,⁴³ and effective attenuation lengths (EALs) for photoelectrons were applied for quantification for the compounds analyzed. EALs were calculated using the standard TPP-2M formalism.⁴⁴ All spectra were referred to the C1s peak of hydrocarbon at 285.0 eV binding energy and controlled using the well-known photoelectron peaks of metallic Cu, Ag, and Au.

2.5 | Nuclear magnetic resonance and electron paramagnetic resonance

Samples were investigated by nuclear magnetic resonance (NMR) under magic-angle spinning (MAS). Powders were filled into 1.8 mm rotors and measured with a home-build NMR probe under 40 kHz MAS at room temperature. The experiments were performed with a Bruker Avance spectrometer. Resonance frequencies, transmitter powers, corresponding B_1 field strengths, and pulse lengths were adjusted for ^{19}F -NMR: 338 MHz with $90^\circ/180^\circ$ pulses of 1.2/2.4 μ s for a Hahn-echo experiment. Spectra were referenced to NaF (aqueous solution). Relevant investigations on CaF_2 nanoparticles for comparison had been reported.^{45,46} Electron paramagnetic resonance (EPR) experiments were carried out at 77 K sample temperature on an X-band system with output power of 100 mW and 100 kHz magnetic field modulation. For each measurement, around 1 mg material was placed into a 4-mm-diameter tube situated in a liquid nitrogen dewar within the system's resonator cavity.

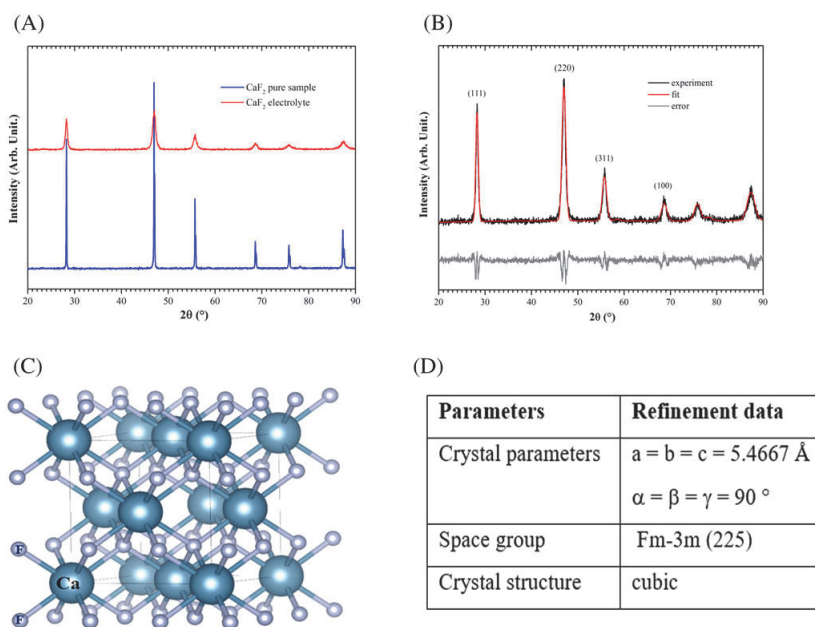


FIGURE 1 Experimental data of the untreated sample (blue line) and the electrolyte (red line) are shown: A, X-ray diffraction (XRD), B, crystallographic refinement for the fluorite-type structure of the electrolyte, C, crystallographic model of CaF_2 . The blue balls represent Ca^{2+} , while the grey balls represent F^- ions. In D, the corresponding refinement data are given

3 | RESULTS AND DISCUSSION

3.1 | XRD, XPS, NMR, and EPR characterization of CaF₂

The XRD patterns of pure CaF₂ and treated samples (see Figure 1A) can be identified to be fluorite-type structures with a space group of Fm-3 m (225); ie, the basic cubic structure for the core of the particles persists stable. The dimension of the unit cells is slightly changing influenced by the effective ionic radii of Ca²⁺ ranging from 5.4690 and 5.4673 to 5.4626 Å of pure, ball milled only and synthesized CaF₂ samples. Rietveld refinement was performed (Figure 1B)^{17,47} to extract crystal parameters. The particle sizes alter from 7.3 μm to 30 nm and crystallite size from (D) 106.7 to 12.5 nm. Earlier reports indicate that ball-milling durations affect the crystallite size: 4, 8, and 16 hours introduced a change in the range from 25 to 30 nm. Results are listed in Table 1.

From ¹⁹F-MAS-NMR experiments (Figure 2C), it becomes evident that a shift of the main peak (from -109 to -111 ppm) and a line broadening are introduced by the influence of vapor pressure and high-energy ball milling. Reasons are the change in the unit cell, particles size/shape, and different packing (also related to an altered shape/packing parameter distribution), which additionally influences the intrinsic susceptibility of the powder. Also, the introduction of defects and unit-cell distortions, geometry frustration at grain boundaries of different crystallites,⁴⁸ is reflected in an increase of line broadening.⁴⁶ An additional small peak at -132 ppm can be assigned to mobile interstitial defect structures with large concentration at the surface with formation energies^{39,45} around 0.25 eV.

During material exposure to vapor pressure, water molecules get in contact with the particle surfaces.⁴ It is known that H₂O molecules are adsorbed at CaF₂(111) introducing negative surface hydroxyl groups⁷ and positively charged hydrogen, which can occupy Ca²⁺ sites as point defects.⁶ Ca²⁺ vacancies favor V_F centers, (F₂)⁻, which are further promoted by high-energy milling under an oxygen atmosphere, introducing O²⁻ defects: fluoride vacancies (F centers, i.e., fluoride vacancies occupied by electrons) and further interstitials (H centers, i.e., fluoride ions related to vacancies, small) are created.⁴⁷ From XPS measurements, see Figure 2B, OH⁻ and O²⁻ sites had been identified: the O1s peaks could be deconvoluted into four peaks, which are related to hydroxide, ionic oxygen, and oxygen bonded to carbon (C—O and C=O).⁴⁹ Related C1s spectra (not shown) provide relevant two peaks, which are known to originate from background source and are applied for referencing.⁵⁰

The increase of paramagnetic defects due to O²⁻ can be observed with EPR (Figure 2D): the pure sample provided a low, the prepared electrolyte showed a strong powder-averaged signal of several lines. For F₂ centers, the dominating zz principal component has been identified to be around 900 Gauss.⁹ The broad lines suggest that defect structure complexes and higher-order shell influences are present.

TABLE 1 Summary of XRD, SEM and EIS results

CaF ₂ compound	Pure CaF ₂ from Supplier	Ball-milled CaF ₂	Electrolyte
Source of vapor pressure	-	-	Saturated KCl solution
Condition	-	-	24 h at 50°C
Ball-milling time, h	-	18	18
Cell parameter a = b = c, Å	5.4690	5.4673	5.4626
Space group		Fm-3 m (225)	
Crystallite size, nm	106.7	15.6	12.5
Particle size, nm	7320	50	30
Resistance, kΩ	-	439.65	4.633
Pellet diameter, mm		10 (d)	10 (d)
Pellet thickness, mm		1 (t)	1 (t)
Ionic conductivity at room temperature, S·cm ⁻¹	7·10 ⁻¹¹ (Patro et al ³⁴)	1.98·10 ⁻⁷ 1.6·10 ⁻¹¹ (47)	1.88·10 ⁻⁵
Activation energy, eV	-	0.56 (0.78 (47))	0.35

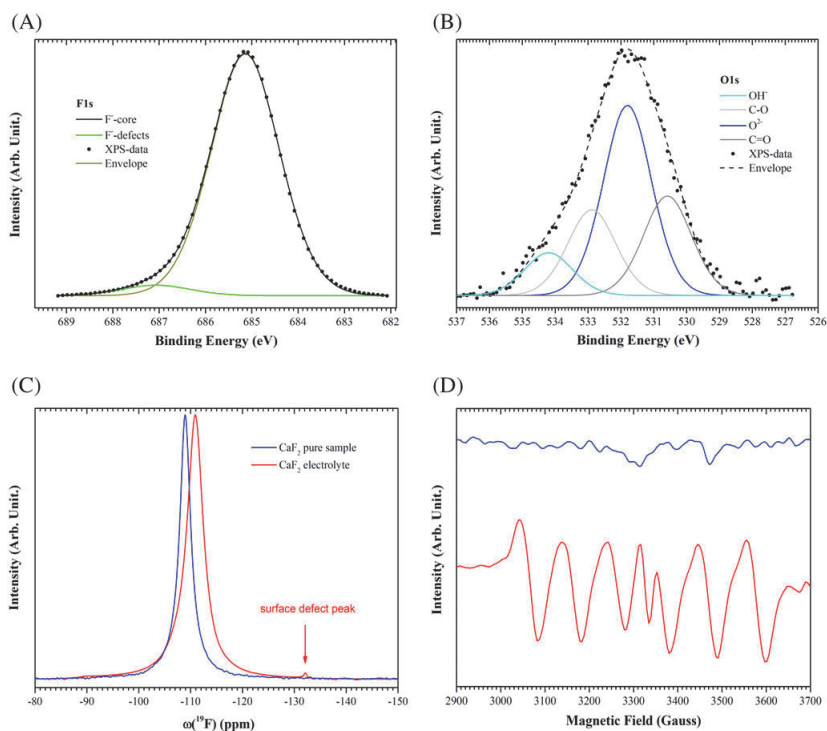


FIGURE 2 In A, and B, X-ray photoelectron spectroscopy (XPS) spectra of the CaF_2 electrolyte are given: F1s bulk and defect signals of the nano-material and O1s peaks of OH^- (534.4 eV), C—O (533.0 eV), O^{2-} (531.8 eV), and C=O (530.5 eV) are shown. Further experimental data of the pure sample (blue lines) and the electrolyte (red lines) are provided: C, ^{19}F -nuclear magnetic resonance (NMR) and D, electron paramagnetic resonance (EPR)

3.2 | SEM and FESEM investigations

SEM and FESEM were carried out to illustrate the morphology of the commercial and prepared samples from which, for the pure CaF_2 sample, a particle size of 7.26 μm had been obtained, shown in Figure 3A,B, and for the electrolyte powder, grain size of 30 nm had been extracted, see Figure 3C,D. The structural features were analyzed for different observation windows.⁷ Agglomerates of CaF_2 of size ranging from a few dozens to several 10 nm are typically observed. Cubic particles are typically related to pristine materials and are explicitly recognized in the product of ball-milled samples.

FESEM of electrolyte pellets was imaged to observe the cross-sectional morphology,³⁷ see Figure 3E,F, indicating that the pellet consists of uniformly aligned and packed CaF_2 electrolyte nano-powder. The surface layer of the CaF_2 pellet consists of Au with a layer thickness of 50 nm.

3.3 | Electrochemical impedance spectroscopy measurement and electrochemical cell testing

Impedance spectroscopy is commonly used to measure the ionic conductivity of a compound in pellet form placed between two electrodes.^{36,37} The impedances within a critical frequency range were obtained for the pure CaF_2 and the electrolyte at different temperatures up to +100°C, see Figure 4A,B. Such spectra consist of a semicircle at high and a straight line at low frequencies. The latter is representing the charging of ionic species at the electrolyte-electrode interface (Au) as ion blockage.^{18,33} The resistance of the system corresponds to the intersection of the complex impedance semicircle with the x-axis diminishing the reactance providing pure real contributions at lower frequencies. Fitting of the measured Nyquist plots had been carried out to obtain relevant material parameters.^{41,51,52} The applied

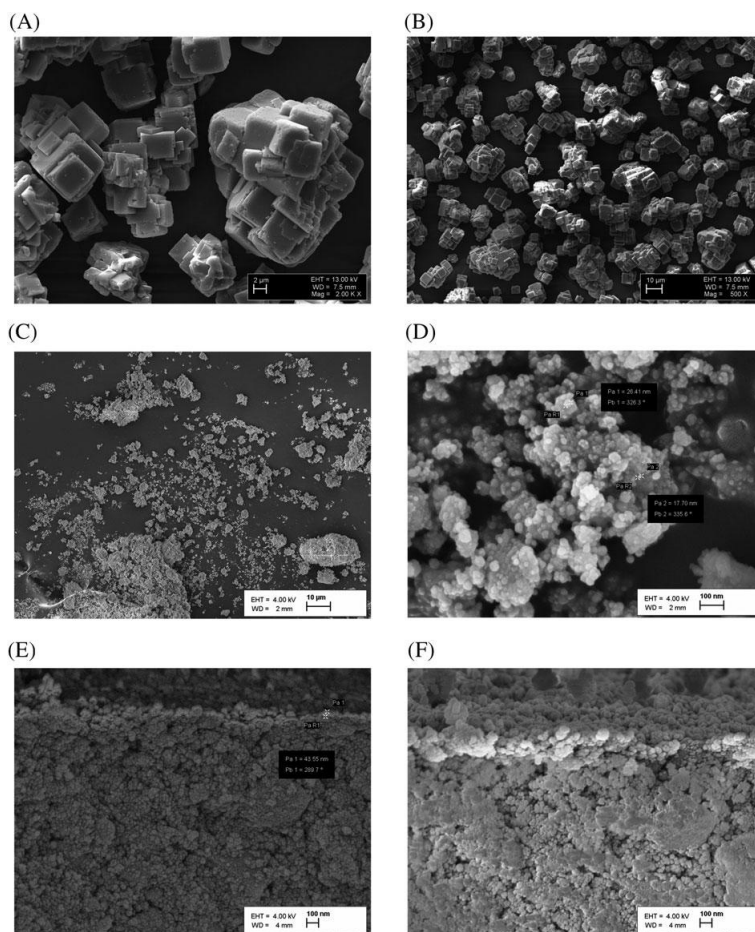


FIGURE 3 Scanning electron microscope (SEM) and field emission SEM (FESEM) images of CaF_2 materials are depicted: A,B, pure sample from the supplier and C,D, humidified/ball-milled CaF_2 electrolyte. Images of the humidified/ball-milled CaF_2 electrolyte pressed in pellet form show the cross-sectional morphology: E,F, different resolutions are recorded. An interface Au layer can be observed to be around 50 nm

equivalent circuit model for the electrolyte (inset in Figure 4B) composed of two constant phase elements (CPE1 and CPE2) and an ohmic resistor (R1).¹⁷ The capacitance values corresponding to the semicircle (CPE1) were identified to be roughly about 10^{-8} F. Fluorite-type compounds are known to be displayed only by one such semicircle representing combined bulk/grain boundaries phenomena⁴⁷ and the second capacitance corresponding to the straight line (CPE2) being in the range of 10^{-6} F reflecting the electrode interfaces phenomena.^{19,27} Finally, the resistor is related to the macroscopic ionic resistance.^{16,17} The related ionic conductivity of fluoride ions of solid electrolytes can be determined from the resistance (R), pellet thickness (t), and its surface area (A) by the equation: $\sigma = [t/(R \cdot A)]$.^{15,16} Applying this, we estimate a conductivity of $1.88 \cdot 10^{-5} \text{ S} \cdot \text{cm}^{-1}$ at room temperature. Considering the well-known temperature dependence attributed to an Arrhenius type of behavior, $\sigma_T = \sigma_0 \cdot \exp(-E_a/[k \cdot T])$, two parameters can be extracted by fitting data recorded at different temperature (T): σ_0 , the ionic conductivity at infinite temperature (for thoroughly excited/free ions sometimes even considered being temperature dependent itself), and E_a , the ion activation energy.¹⁶ It can be observed that the ionic conductivity of the electrolyte considerably improves from -10°C to room temperature by an order of magnitude and further increases at higher temperatures, up to $+40^\circ\text{C}$. At an even higher temperature, the conductivity promoting defect structure decomposes, and the ionic conductivity decreases.

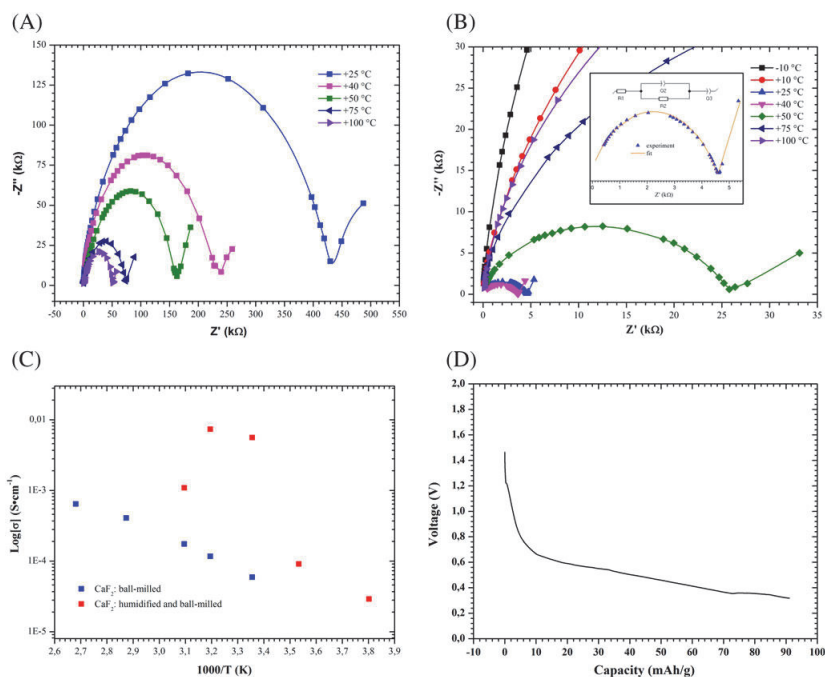


FIGURE 4 Nyquist plots of the CaF_2 pellets of pure CaF_2 ball-milled samples (RT to $+100^\circ\text{C}$) are shown in A. Similar results of the as-prepared electrolyte (CaF_2 humidified and ball milled) for different temperatures (-10°C to $+100^\circ\text{C}$) are represented in B. Also, the fit of the RT plot alongside the applied equivalent circuit is depicted in the inset. In C, extracted data applying for the Arrhenius fits $-\log(\sigma)$ vs $1/T$ of the temperature-dependent ionic conductivities are provided. The discharge curve of an $\text{Mg}/\text{CaF}_2/\text{BiF}_3$ electrochemical cell using the superionic electrolyte operated at RT is shown in (D)

For the electrolyte, the activation energy turned out to be 0.35 eV within the temperature range of -10°C to $+40^\circ\text{C}$. For the untreated but ball-milled CaF_2 powder, 0.56 eV was extracted, which is in the order of reported values (0.78 eV).¹⁶ The conductivity is increasing while the crystallite size reduces, suggesting a conduction mechanism along the grain boundaries. However, whether the conductivity is controlled by the motion of the fluoride vacancies or interstitials, ie, vacancy versus interstitial mechanism, remains speculative.^{30,53} A recent study³⁵ has shown that the ionic conductivity of nanocrystalline CaF_2 can be orders of magnitude higher than its microcrystalline counterpart. It has been suggested that such a difference may arise from the presence of a significant fraction of grain boundaries in the nanocrystalline sample. While there are numerous reports on the enhancement of ionic conductivity of nanocrystalline materials,⁵⁴ the exact mechanism of conduction, their defect chemistry, and the nature of the disorder are still relatively unknown³⁵; we can show in this study that crystal surface defects are strongly influenced overall bulk conductivities.

Such CaF_2 solid-state electrolytes are promising candidates for the application of fluoride-ion-shuttled electrochemical cells and other devices. The overall performance depends on the choice of active metal and metal fluoride and the related prepared electrode composites consisting also of binder and carbon black.

Since an ionic conductivity of around $2 \cdot 10^{-5} \text{ S}\cdot\text{cm}^{-1}$ was achieved, the synthesized material was selected as an electrolyte to test for FIB performance.^{14,54} As cathode material, a BiF_3 composite²⁶ and, for the anode, an Mg composite had been prepared. The galvanic discharge profile of $\text{Mg}/\text{CaF}_2/\text{BiF}_3$ cell operated at room temperature (RT) is shown in Figure 4D. The capacity of the battery referred to cathode was estimated by weight of active material. The BiF_3 composite electrode shows an achieved discharge capacity of $90 \text{ mA}\cdot\text{h}\cdot\text{g}^{-1}$, which is around 30% of the theoretical capacity ($302 \text{ mA}\cdot\text{h}\cdot\text{g}^{-1}$). Discharging by applying a current load, the voltage decayed sharply to 1.5 V, after specific discharge, a plateau at about 0.4 V had been reached. Despite delivering a significant amount of discharge capacity, charging was not possible because of declining electronic and ionic conductivity of discharge product (MgF_2 or Bi). Further investigations and improvements are recommended.

4 | CONCLUSION

Pure CaF_2 solid powder of basic fluorite-type crystal structure was exposed to defined salt H_2O vapor pressure and post-ball milled, which is a simple, scalable, and flexible synthesis technique. The obtained ionic conductivity of synthesized polycrystalline solid CaF_2 electrolyte had been obtained to be $1.9 \cdot 10^{-5} \text{ S}\cdot\text{cm}^{-1}$ at room temperature, which is several orders of magnitude higher than that of pure and ball-milled CaF_2 -reported values ($2 \cdot 10^{-7}$ to $1.6 \cdot 10^{-11} \text{ S}\cdot\text{cm}^{-1}$).⁴⁷ The apparent ion mobilization activation energy of the electrolyte was estimated to be 0.35 eV, which had been reported to be related to the surface formation of interstitial fluoride sites with suggested formation energies^{39,45} of around 0.25 eV. Such activation energy makes the material more attractive as an ion conductor for fluoride shuttle applications. The structure and morphology were studied: a cubic structure with crystallite and particle size of 12.5 and 30 nm had been obtained. NMR, EPR, and XPS investigations support the morphological and defect formation findings at the surface. The CaF_2 electrolyte had been successfully tested in a fluoride-ion battery setup. The findings provide substantial insight and potential for future usage in fluoride shuttle applications and other technologies.

ACKNOWLEDGEMENTS

Authors thank the European Social Fund, Estonia Science Foundation (ESF), and Tallinn University of Technology for funding projects MTT68, PUT126, and PUT1534. Infrastructural support from Karlsruhe Institute of Technology (KIT), Karlsruhe Nano Micro Facility (KNMF), and the National Institute of Chemical Physics and Biophysics (KBFI) is acknowledged.

CONFLICT OF INTEREST

There is no conflict of interest.

ORCID

Palanivel Molaiyan  <https://orcid.org/0000-0001-6039-8426>

Raiker Witter  <https://orcid.org/0000-0002-7085-2490>

REFERENCES

1. Grudinin IS, Matsko AB, Maleki L. Brillouin lasing with a CaF_2 whispering gallery mode resonator. *Phys Rev Lett*. 2009. <https://doi.org/10.1103/PhysRevLett.102.043902>;102(4).
2. Senguttuvan N, Aoshima M, Sumiya K, Ishibashi H. Oriented growth of large size calcium fluoride single crystals for optical lithography. *J Cryst Growth*. 2005. <https://doi.org/10.1016/j.jcrysgro.2005.03.085>;280(3-4):462-466.
3. Akila R, Jacob KT. The mobility of oxygen ions in CaF_2 . *J Appl Electrochem*. 1990. <https://doi.org/10.1007/BF01033608>;20(2):294-300.
4. Cardellach M, Verdager A, Fraxedas J. Defect-induced wetting on $\text{BaF}_2(111)$ and $\text{CaF}_2(111)$ at ambient conditions. *Surf Sci*. 2011. <https://doi.org/10.1016/j.susc.2011.07.003>;605(23-24):1929-1933.
5. Stevenson AJ, Serier-Braut H, Gredin P, Mortier M. Fluoride materials for optical applications: single crystals, ceramics, glasses, and glass-ceramics. *J Fluor Chem*. 2011. <https://doi.org/10.1016/j.jfluchem.2011.07.017>;132(12):1165-1173.
6. Fujii S, Fujihira M. Atomic contrast on a point defect on $\text{CaF}_2(111)$ imaged by non-contact atomic force microscopy. *Nanotechnology*. 2007. <https://doi.org/10.1088/0957-4484/18/8/084011>;18(8):084011.
7. Reichling M, Barth C. Scanning force imaging of atomic size defects on the $\text{CaF}_2(111)$ surface. *Phys Rev Lett*. 1999. <https://doi.org/10.1103/PhysRevLett.83.768>;83(4):768-771.
8. Ribes M, Barrau B, Souquet JL. Sulfide glasses: glass forming region, structure and ionic conduction of glasses in $\text{Na}_2\text{S}_x\text{S}_2(\text{XSi}; \text{Ge})$, $\text{Na}_2\text{SP}_2\text{S}_5$ and Li_2SGeS_2 systems. *J Non Cryst Solids*. 1980. [https://doi.org/10.1016/0022-3093\(80\)90430-5](https://doi.org/10.1016/0022-3093(80)90430-5);38-39:271-276.
9. Susman S, Boehm L, Volin KJ, Delbecq CJ. A new method for the preparation of fast-conducting, reactive glass systems. *Solid State Ion*. 1981. [https://doi.org/10.1016/0167-2738\(81\)90342-8](https://doi.org/10.1016/0167-2738(81)90342-8);5:667-669.
10. Fergus JW. The application of solid fluoride electrolytes in chemical sensors. *Sens Actuators B*. 1997. [https://doi.org/10.1016/S0925-4005\(97\)00193-7](https://doi.org/10.1016/S0925-4005(97)00193-7);42(2):119-130.
11. Sang L, Ren B, Liao M, Koide Y, Sumiya M. Suppression in the electrical hysteresis by using CaF_2 dielectric layer for p-GaN MIS capacitors. *J Appl Phys*. 2018. <https://doi.org/10.1063/1.5010952>;123(16):161423.

12. Illarionov YY, Vexler MI, Fedorov VV, Suturin SM, Sokolov NS. Electrical and optical characterization of Au/CaF₂/p-Si(111) tunnel-injection diodes. *J Appl Phys*. 2014. <https://doi.org/10.1063/1.4882375>;115(22):223706.
13. Armand M, Tarascon JM. 10.1126/Science.1198591 Building better batteries. *Nature*. 2008. <https://doi.org/10.1038/451652a>; 451(7179):652-657.
14. Anji Reddy M, Fichtner M. Batteries based on fluoride shuttle. *J Mater Chem*. 2011;21(43):17059. <https://doi.org/10.1039/c1jm13535j>
15. Rongeat C, Reddy MA, Witter R, Fichtner M. Nanostructured fluorite-type fluorides as electrolytes for fluoride ion batteries. *J Phys Chem C*. 2013;117(10):4943-4950. <https://doi.org/10.1021/jp3117825>
16. Rongeat C, Anji Reddy M, Witter R, Fichtner M. Solid electrolytes for fluorides ion batteries: ionic conductivity in polycrystalline tysonite-type fluorides. *ACS Appl Mater Interfaces*. 2014;6(3):2103-2110. <https://doi.org/10.1021/am4052188>
17. Dieudonné B, Chable J, Mauvy F, et al. Exploring the Sm_{1-x}Ca_xF_{3-x} tysonite solid solution as a solid-state electrolyte: relationships between structural features and F⁻ ionic conductivity. *J Phys Chem C*. 2015;119(45):25170-25179. <https://doi.org/10.1021/acs.jpcc.5b05016>
18. Sorokin NI, Krivandina EA, Zhmurova ZI, Sobolev BP, Fominykh MV, Fistul VV. Superionic conductivity of the heterovalent solid solutions R_{1-x}M_xF_{3-x} (R = REE, M = Ca, Ba) with tysonite-type structure. *Phys Solid State*. 1999;41(4):573-575.
19. Heise M, Scholz G, Düvel A, Heitjans P, Kemnitz E. Mechanochemical synthesis, structure and properties of lead containing alkaline earth metal fluoride solid solutions M_xPb_{1-x}F₂ (M = Ca, Sr, Ba). *Solid State Sci*. 2018. <https://doi.org/10.1016/J.SOLIDSTATESCIENCES.2018.01.007>;77:45-53.
20. Tarascon JM, Armand M. Issues and challenges facing rechargeable lithium batteries. *Nature*. 2001;414(6861):359-367. <https://doi.org/10.1038/35104644>
21. Kamaya N, Homma K, Yamakawa Y, et al. A lithium superionic conductor. *Nat Mater*. 2011;10(9):682-686. <https://doi.org/10.1038/nmat3066>
22. Hammad Fawey M, Chakravadhanula VSK, Reddy MA, et al. In situ TEM studies of micron-sized all-solid-state fluoride ion batteries: preparation, prospects, and challenges. *Microsc Res Tech*. 2016. <https://doi.org/10.1002/jemt.22675>;79(7):615-624.
23. Zhang L, Anji Reddy M, Fichtner M. Development of tysonite-type fluoride conducting thin film electrolytes for fluoride ion batteries. *Solid State Ion*. 2015;272:39-44. <https://doi.org/10.1016/j.ssi.2014.12.010>
24. Zhang L, Anji Reddy M, Gao P, Fichtner M. Development of dense solid state thin-film electrolyte for fluoride ion batteries. *J Alloys Compd*. 2016;684:733-738. <https://doi.org/10.1016/j.jallcom.2016.04.196>
25. Gschwind F, Rodriguez-Garcia G, Sandbeck DJS, et al. Fluoride ion batteries: theoretical performance, safety, toxicity, and a combinatorial screening of new electrodes. *J Fluor Chem*. 2016;182:76-90. <https://doi.org/10.1016/j.jfluchem.2015.12.002>.
26. Gschwind F, Bastien J. Parametric investigation of room-temperature fluoride-ion batteries: assessment of electrolytes, Mg-based anodes, and BiF₃-cathodes. *J Mater Chem A*. 2015. <https://doi.org/10.1039/c4ta06625a>;3(10):5628-5634.
27. Heise M, Scholz G, Düvel A, Heitjans P, Kemnitz E. Mechanochemical synthesis, structure, and properties of solid solutions of alkaline earth metal fluorides: Ma_{1-x}Mb_xF₂ (M:Ca,Sr,Ba). *Solid State Sci*. 2016;60:65-74. <https://doi.org/10.1016/j.solidstatesciences.2016.08.004>
28. Sobolev BP, Sviridov IA, Fadeeva VI, et al. Mechanochemical synthesis of nonstoichiometric nanocrystals La_{1-y}Ca_yF_{3-y} with a tysonite structure and nanoceramic materials from CaF₂ and LaF₃ crystals. *Crystallogr Reports*. 2008;53(5):868-880. <https://doi.org/10.1134/S1063774508050234>
29. Bhatia H, Thieu DT, Pohl AH, et al. Conductivity optimization of tysonite-type La_{1-x}Ba_xF_{3-x} solid electrolytes for advanced fluoride ion battery. *ACS Appl Mater Interfaces*. 2017;9(28):23707-23715. <https://doi.org/10.1021/acsami.7b04936>
30. Aalders AF, Arts AFM, de Wijn HW. The fluorine ionic motion in tysonite-structured solid solutions. *Solid State Ion*. 1985. [https://doi.org/10.1016/0167-2738\(85\)90146-8](https://doi.org/10.1016/0167-2738(85)90146-8);17(3):241-250.
31. Vijayakumar M, Selvasekarapandian S, Gnanasekaran T, Fujihara S, Koji S. Structural and impedance studies on LaF₃ thin films prepared by vacuum evaporation. *J Fluor Chem*. 2004;125(7):1119-1125. <https://doi.org/10.1016/j.jfluchem.2004.02.001>
32. Mu X, Sigle W, Bach A, Fischer D, Jansen M, Van Aken PA. Influence of a second cation (M = Ca²⁺, Mg²⁺) on the phase evolution of (Ba_xM_{1-x})F₂ starting from amorphous deposits. *Zeitschrift für Anorg und Allg Chemie*. 2014. <https://doi.org/10.1002/zaac.201400099>; 640(10):1868-1875.
33. Ruprecht B, Wilkening M, Steuernagel S, Heitjans P. Anion diffusivity in highly conductive nanocrystalline BaF₂:CaF₂ composites prepared by high-energy ball milling. *J Mater Chem*. 2008;18(44):5412-5416. <https://doi.org/10.1039/b811453f>
34. Patro LNN, Hariharan K. Fast fluoride ion conducting materials in solid state ionics: an overview. *Solid State Ion*. 2013;239:41-49. <https://doi.org/10.1016/j.ssi.2013.03.009>
35. Scholz G, Dörfel I, Heidemann D, Feist M, Stösser R. Nanocrystalline CaF₂ particles obtained by high-energy ball milling. *J Solid State Chem*. 2006. <https://doi.org/10.1016/j.jssc.2005.12.035>;179(4):1119-1128.
36. Hagenmuller P, Réau JM, Lucat C, Matar S, Villeneuve G. Ionic conductivity of fluorite-type fluorides. *Solid State Ion*. 1981. [https://doi.org/10.1016/0167-2738\(81\)90110-7](https://doi.org/10.1016/0167-2738(81)90110-7);3-4:341-345.
37. Hayashi A, Noi K, Sakuda A, Tatsumisago M. Superionic glass-ceramic electrolytes for room-temperature rechargeable sodium batteries. *Nat Commun*. 2012;3(1):856. <https://doi.org/10.1038/ncomms1843>.

38. Ghosh S. Comment on "enhancement of ionic conduction in CaF_2 and BaF_2 by dispersion of Al_2O_3 ." *J Mater Sci Lett*. 1990. <https://doi.org/10.1007/BF00721625>;9(12):1488.
39. Ibraheem AM, Khalafalla MAH, Eisa MH. First principle calculation of accurate native defect levels in CaF_2 . *Eur Phys J B*. 2017. <https://doi.org/10.1140/epjb/e2017-70591-0>;90(3).
40. Pui W, Rodewald S, Ramlau R, Heitjans P, Maier J. Local and overall ionic conductivity in nanocrystalline CaF_2 . *Solid State Ion*. 2000;131(1):159-164. [https://doi.org/10.1016/S0167-2738\(00\)00630-5](https://doi.org/10.1016/S0167-2738(00)00630-5)
41. Chable J, Martin AG, Bourdin A, et al. Fluoride solid electrolytes: from microcrystalline to nanostructured tysonite-type $\text{La}_{0.95}\text{Ba}_{0.05}\text{F}_{2.95}$. *J Alloys Compd*. 2017;692:980-988. <https://doi.org/10.1016/j.jallcom.2016.09.135>
42. Aziz M, Ismail AF. X-ray photoelectron spectroscopy (XPS). In: *Membrane Characterization*. Elsevier; 2017 <https://doi.org/10.1016/B978-0-444-63776-5.00005-X>.
43. Scofield JH. Hartree-Slater subshell photoionization cross-sections at 1254 and 1487 eV. *J Electron Spectros Relat Phenomena*. 1976. [https://doi.org/10.1016/0368-2048\(76\)80015-1](https://doi.org/10.1016/0368-2048(76)80015-1);8(2):129-137.
44. Tanuma S, Powell CJ, Penn DR. Calculations of electron inelastic mean free paths. V. Data for 14 organic compounds over the 50–2000 eV range. *Surf Interface Anal*. 1994. [https://doi.org/10.1002/sia.740210302;21\(3\):165-176](https://doi.org/10.1002/sia.740210302;21(3):165-176).
45. Jain P, Kim S, Youngman RE, Sen S. Direct observation of defect dynamics in nanocrystalline CaF_2 : results from ^{19}F MAS NMR spectroscopy. *J Phys Chem Lett*. 2010. [https://doi.org/10.1021/jz100152j;1\(7\):1126-1129](https://doi.org/10.1021/jz100152j;1(7):1126-1129).
46. Witter R, Roming M, Feldmann C, Ulrich AS. Multilayered core-shell structure of polyol-stabilized calcium fluoride nanoparticles characterized by NMR. *J Colloid Interface Sci*. 2013;390(1):250-257. <https://doi.org/10.1016/j.jcis.2012.09.001>
47. Breuer S, Wilkening M. Mismatch in cation size causes rapid anion dynamics in solid electrolytes: the role of the Arrhenius pre-factor. *Dalton Trans*. 2018. [https://doi.org/10.1039/c7dt04487a;47\(12\):4105-4117](https://doi.org/10.1039/c7dt04487a;47(12):4105-4117).
48. Kwoka M, Ottaviano L, Passacantando M, Santucci S, Czempik G, Szuber J. XPS study of the surface chemistry of L-CVD SnO_2 thin films after oxidation. *Thin Solid Films*. 2005. [https://doi.org/10.1016/j.tsf.2005.04.014;490\(1\):36-42](https://doi.org/10.1016/j.tsf.2005.04.014;490(1):36-42).
49. Chang DW, Choi HJ, Jeon IY, Seo JM, Dai L, Baek JB. Solvent-free mechanochemical reduction of graphene oxide. *Carbon N Y*. 2014. <https://doi.org/10.1016/j.carbon.2014.05.055;77:501-507>.
50. Zhang L, Reddy MA, Fichtner M. Electrochemical performance of all solid-state fluoride-ion batteries based on thin-film electrolyte using alternative conductive additives and anodes. *J Solid State Electrochem*. 2018. [https://doi.org/10.1007/s10008-017-3838-2;22\(4\):997-1006](https://doi.org/10.1007/s10008-017-3838-2;22(4):997-1006).
51. Sakuda A, Hayashi A, Tatsumisago M. Sulfide solid electrolyte with favorable mechanical property for all-solid-state lithium battery. *Sci Rep*. 2013. [https://doi.org/10.1038/srep02261;3\(1\)](https://doi.org/10.1038/srep02261;3(1)).
52. Ramachandran R, Johnson-Mcdaniel D, Salguero TT. Formation and scrolling behavior of metal fluoride and oxyfluoride nanosheets. *Chem Mater*. 2016. [https://doi.org/10.1021/acs.chemmater.6b02061;28\(20\):7257-7267](https://doi.org/10.1021/acs.chemmater.6b02061;28(20):7257-7267).
53. Lukatskaya MR, Dunn B, Gogotsi Y. Multidimensional materials and device architectures for future hybrid energy storage. *Nat Commun*. 2016;7(1):12647. <https://doi.org/10.1038/ncomms12647>.
54. Sobolev BP, Sorokin NI, Bolotina NB. Nonstoichiometric single crystals $\text{M}_{1-x}\text{R}_x\text{F}_{2+x}$ and $\text{R}_{1-y}\text{M}_y\text{F}_{3-y}$ (M Ca, Sr, Ba; R rare earth elements) as fluorine-ionic conductive solid electrolytes. In: *Photonic and Electronic Properties of Fluoride Materials: Progress in Fluorine Science Series*. Elsevier; 2016 <https://doi.org/10.1016/B978-0-12-801639-8.00021-0>.

How to cite this article: Molaiyan P, Witter R. Surface defect-enhanced conductivity of calcium fluoride for electrochemical applications. *Mat Design Process Comm*. 2019;1–10. <https://doi.org/10.1002/mdp2.44>

Publication II

P. Molaiyan and R. Witter; Mechanochemical synthesis of solid-state electrolyte $\text{Sm}_{1-x}\text{Ca}_x\text{F}_{3-x}$ for batteries and other electrochemical devices. *Materials Letters*. 2019, vol. 244, pp. 22–26.

<https://doi.org/10.1016/j.jelechem.2019.04.063> (Reproduced from ref.[126] with permission from Elsevier Publishing Group)



Mechanochemical synthesis of solid-state electrolyte $\text{Sm}_{1-x}\text{Ca}_x\text{F}_{3-x}$ for batteries and other electrochemical devices

Palanivel Molaiyan^a, Raiker Witter^{a,b,c,*}

^aSchool of Information Technologies, Tallinn University of Technology (TUT), Akadeemia tee 15A, 12618 Tallinn, Estonia

^bInstitute of Nanotechnology, Karlsruhe Institute of Technology (KIT), POB 3640, 76021 Karlsruhe, Germany

^cInstitute of Quantum Optics, University Ulm, Albert-Einstein-Allee 11, 89081 Ulm, Germany



ARTICLE INFO

Article history:

Received 31 December 2018

Received in revised form 3 February 2019

Accepted 4 February 2019

Available online 13 February 2019

Keywords:

Solid-state fluoride electrolyte

Ball-milling

Ionic conductivity

¹⁹F NMR

Fluoride shuttle sensors

Fluoride ion battery

ABSTRACT

Solid-state secondary batteries employing solid electrolytes provide the advantage to be potentially more stable than conventional batteries and hence are safer. At present, investigations of related ionic conductivities of solid ion conductors are attracting attention. In this work, we have prepared SmF_3 with CaF_2 doped materials. Different $\text{Sm}_{1-x}\text{Ca}_x\text{F}_{3-x}$ compositions which are dependent on the stoichiometric ratio ($0 \leq x \leq 0.15$) had been obtained by planetary high-energy mechanochemical milling. Structural, morphology and ionic conductivities of the synthesized $\text{Sm}_{1-x}\text{Ca}_x\text{F}_{3-x}$ electrolytes were examined. From X-ray diffraction (XRD) and Field Emission Scanning Electron Microscopy (FESEM), it was revealed that $\text{Sm}_{1-x}\text{Ca}_x\text{F}_{3-x}$ constitutes in a tysonite-type structure with a crystallite size of around 10–20 nm and an average particle size of 50 nm. At room temperature, the highest ionic conductivity was achieved for $\text{Sm}_{0.95}\text{Ca}_{0.05}\text{F}_{2.95}$ of $2.8 \cdot 10^{-5} \text{ S cm}^{-1}$. The corresponding activation energy was extracted to be 0.40 eV. Finally, a proof-of-principle solid-state Fluoride Ion Battery (FIB) had been tested based on a $\text{CeF}_3/\text{Sm}_{0.95}\text{Ca}_{0.05}\text{F}_{2.95}/\text{Bi}$ electrochemical system.

© 2019 Published by Elsevier B.V.

1. Introduction

The trend for developing next-generation battery systems [1,2] has recently set all-solid-state batteries into focus [3] for which solid electrolytes are a critical component, and high ionic conductivities are essential [4]. Despite the significant usage of lithium-ion based systems, alternatives as fluoride ion driven applications for sensors and energy storage system has been identified [5,6]. Improved solid electrolytes such as LaF_3 doped with BaF_2 have been recently reported that exhibit high ionic conductivities [7–9]. Related to that the topic of secondary batteries based on fluoride shuttle has gained of importance [10,11].

Solid-state electrolyte combinations of rare earth ($R = \text{La} - \text{Lu}$, Sm) and alkaline earth ($M = \text{Ca}$, Sr, Ba) metal fluorides have been explored to form $R_{1-x}M_xF_{3-x}$ with the stabilization of fluoride vacancies [12–14]. The different ionic radii of the alkaline earth cations ($\text{Ba}^{2+} > \text{Sr}^{2+} > \text{Ca}^{2+}$) as well as of earth cations ($\text{La}^{3+} > \dots > \text{Lu}^{3+}$) influence the local environments of fluoride and conse-

quently, their mobility [15,16]. Promising reported ionic conductivities on single crystals had been obtained with La, Ce, Nd, and Sm in combination with Ca, Ba and Sr [17]: varying from 10^{-3} to $10^{-6} \text{ S cm}^{-1}$ at room temperature (RT) and up to $10^{-2} - 10^{-3} \text{ S cm}^{-1}$ at $150 \text{ }^\circ\text{C}$ [16].

For the SmF_3 system, different structural types depending on the synthesis method are known: the orthorhombic YF_3 -type structure (Pnma, $Z = 4$) and the LaF_3 tysonite-type structure (P3c1, $Z = 6$). Considerable high ionic conductivity had been achieved by a small amount of Ca^{2+} doping, stabilizing the tysonite-type network [9,18]. Recent investigations on this system reported the synthesis by high temperature treatment [19–21]. In this work, we prepared $\text{Sm}_{1-x}\text{Ca}_x\text{F}_{3-x}$ ($0 \leq x \leq 0.15$) solid solutions by solid synthesis at RT applying a high energy ball-milling method without any material pre- or post-processing. From X-ray diffraction (XRD) it became evident that the electrolytes consist of the desired tysonite type (trigonal) phase structure. The prepared samples were analyzed with electrochemical impedance spectroscopy (EIS) which provided fluoride-ion conductivities of $2.8 \cdot 10^{-5} \text{ S cm}^{-1}$ at RT and $5.8 \cdot 10^{-4} \text{ S cm}^{-1}$ at $100 \text{ }^\circ\text{C}$ for $\text{Sm}_{0.95}\text{Ca}_{0.05}\text{F}_{2.95}$. Since BiF_3 showed good reversibility in solid-state FIBs [10] we tested this electrolyte in a solid-state battery based on $\text{CeF}_3/\text{Sm}_{0.95}\text{Ca}_{0.05}\text{F}_{2.95}/\text{Bi}$ [11].

* Corresponding author at: School of Information Technologies, Tallinn University of Technology (TUT), Akadeemia tee 15A, 12618 Tallinn, Estonia.

E-mail address: raiker.witter@mail.com (R. Witter).

2. Experimental section

2.1. Preparation of $\text{Sm}_{1-x}\text{Ca}_x\text{F}_{3-x}$ ($0 \leq x \leq 0.15$) electrolyte by solid synthesis

The pure CaF_2 sample was purchased from Alfa Aaser (99%) and SmF_3 (REO) anhydrous from Alfa Aaser (99.9%). The stoichiometric compositions of $\text{Sm}_{1-x}\text{Ca}_x\text{F}_{3-x}$ ($0 \leq x \leq 0.15$) were synthesized by a high-energy mechanochemical technique using a planetary ball-mill (Tanchen powder). The materials were placed into silicon nitride vial (internal volume of 50 ml) locked in vacuum sealed containers together with silicon nitride balls of a ball to powder ratio of 18:1. The mechanochemical reaction was performed for 18 h at a fixed rotation speed of the base disc of 600 rpm to form nanopowders.

2.2. Structural and morphology characterization

X-ray diffraction (XRD) using an AXS Bruker D5005 Advance instrument with $\text{Cu K}\alpha$ radiation ($\lambda_1=1.54056 \text{ \AA}$, $\lambda_2=1.544390 \text{ \AA}$) with variable slit. The microstructure of a cross-section of the electrolytes was observed by Field Emission Scanning Electron Microscope (FESEM) (Carl Zeiss Ultra 55). Fluorine Nuclear Magnetic Resonance (^{19}F NMR) experiments were performed on a Bruker Avance 800 MHz spectrometer, using a high spinning speed probe. The pulse length of 90° was set to $0.9 \mu\text{s}$ at roughly 60 W. Experiments were carried out at RT. High-Resolution Transmission Electron Microscopy (HRTEM) was carried out with aberration-corrected (image-corrected) FEI Probe Titan G2 80-200 operated at 200 kV.

2.3. Electrochemical impedance spectroscopy (EIS)

The as-prepared electrolyte samples were pressed applying a pellet press (Across international) under air atmosphere. Pellet thicknesses of around 1 mm at a diameter of 10 mm were

obtained. They were gold coated on both sides using sputtering (JEOL, sputter coater) and were further investigated by impedance measurements with an Agilent 4192A LF impedance analyzer within a frequency range from 5 Hz to 13 MHz with a voltage amplitude of 10 mV. The measurements were carried out at different temperature from RT to 100°C at air atmosphere.

2.4. Electrochemical cell testing

The electrochemical studies had been conducted on composite electrodes which were prepared by ball-milling: the cathode from 50% Bi-metal powder, 10% carbon black (99.0%, Alfa Aaser), 10% Polyvinylidene fluoride (PVDF, 99.0%, Alfa Aaser) and 30% $\text{Sm}_{0.95}\text{Ca}_{0.05}\text{F}_{2.95}$ electrolyte; and the anode from 80% Cerium Fluoride powder, 10% carbon black (99.0%, Alfa Aaser), 10% PVDF (99.0%, Alfa Aaser). All solid-state fluoride ion battery cell was fabricated by pressing anode composite (CeF_3 composite), electrolyte ($\text{Sm}_{0.95}\text{Ca}_{0.05}\text{F}_{2.95}$) and cathode (Bi composite) together into a 10 mm diameter pellet using a desktop press (Across International) under argon atmosphere. The pellet was sealed within a coin cell CR2023 case. Electrochemical testing of the cell was performed at 75°C applying a Keysight N6705B (DC power analyzer) battery tester. The cell was charged/discharged with a current density of $1 \mu\text{A cm}^{-2}$ within a voltage interval of 0.01–0.90 V.

3. Results and discussions

3.1. XRD and NMR structural characterization

XRD diffraction patterns of $\text{Sm}_{0.95}\text{Ca}_{0.05}\text{F}_{2.95}$ and ^{19}F NMR spectra are shown in Fig. 1 indicates that the sample exhibits tysonite type trigonal structure with space group P3c1 and exchanging crystal fluoride lattice sites F₁, F₂, and F₃. A recent study of a temperature driven synthesis applying up to 1000°C reported that

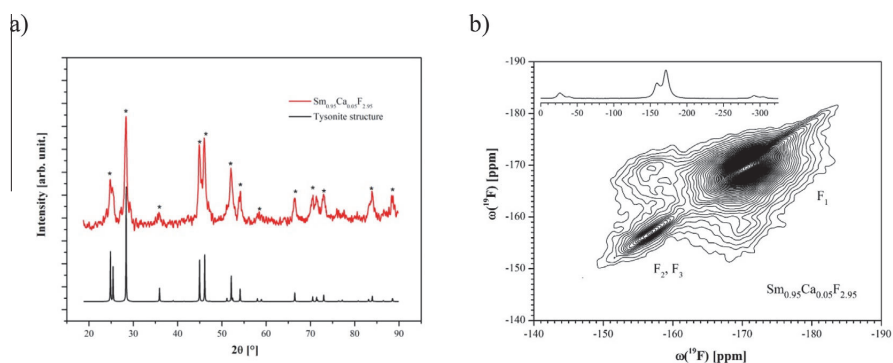


Fig. 1. X-ray diffraction pattern of $\text{Sm}_{0.95}\text{Ca}_{0.05}\text{F}_{2.95}$ providing evidence of a tysonite-type structure (trigonal, simulated black line) are shown in a). In b) ^{19}F 2D high-resolution MAS exchange and 1D experiments (measured at RT) also support the presence of trigonal structure, indicating three lattice sites (F₁, F₂, and F₃) which is consistent with the literature.

Table 1

Collected data of the $\text{Sm}_{1-x}\text{Ca}_x\text{F}_{3-x}$ ($0 \leq x \leq 0.15$) solid electrolytes are provided. (The standard deviation of the extracted ionic conductivities was less than 10%.)

Parameters	$\text{Sm}_{1-x}\text{Ca}_x\text{F}_{3-x}$ ($0 \leq x \leq 0.15$)			
	x = 0	x = 0.05	x = 0.10	x = 0.15
Cell dimension a (Å)	6.96	6.95	6.95	6.95
Cell dimension c (Å)	7.12	7.13	7.14	7.13
Crystallite Size (nm)	10.4	12.9	13.9	18.0
Ionic Conductivity at RT (S cm^{-1})	$1.1 \cdot 10^{-6}$ (0.1)	$2.8 \cdot 10^{-5}$ (0.1)	$1.6 \cdot 10^{-5}$ (0.1)	$4.0 \cdot 10^{-6}$ (0.1)
Ionic Conductivity at 100°C (S cm^{-1})	$4.9 \cdot 10^{-4}$	$5.8 \cdot 10^{-4}$	$3.5 \cdot 10^{-4}$	$2.4 \cdot 10^{-4}$
E_a (eV)	0.55 (0.04)	0.40 (0.05)	0.42 (0.04)	0.53 (0.07)

obtained $\text{Sm}_{1-x}\text{Ca}_x\text{F}_{3-x}$ consisted of tysonite- and YF_3 -type structures [9,16]. Our pure phase provided an average crystallite size from (D) = 10 to 18 nm increasing with Ca^{2+} content [22].

For increasing stoichiometric parameter $x > 0$, the unit cell parameter (lattice parameter a) decreases, whereas the c parameter increases with Ca^{2+} doping (Table 1). The resulting volume change of the unit cell is mostly dependent on the ionic radii of Sm^{3+} and Ca^{2+} (1.27 and 1.32 Å) [2,23], which should imply an

expansion of the unit cell parameters [2]. Still, at a specific content of anionic vacancies which decreases the cationic coordination, i.e., a preferential stabilization of fluoride vacancies in the vicinity of Ca^{2+} ions is reached, the net volume reduces [24,25]. The decrease of the ionic conductivity and the increase of the activation energy versus Ca concentration can be explained by the vacancies around the calcium sites. The results are listed in Table 1. Slight introduction of Schottky defects (vacancies) during high-energy ball-

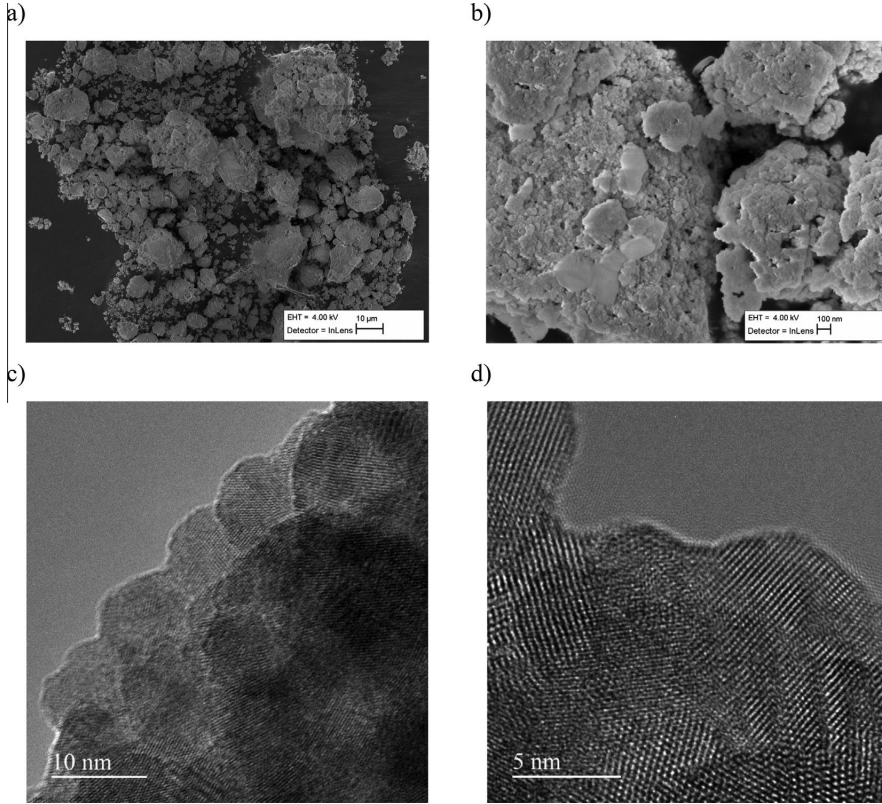


Fig. 2. FESEM morphology of $\text{Sm}_{0.95}\text{Ca}_{0.05}\text{F}_{2.95}$ is provided in a) and b) with different resolutions (scale bars of 10 μm and 100 nm). HRTEM images of the same material are given in c) and d); bars of 10 nm and 5 nm.

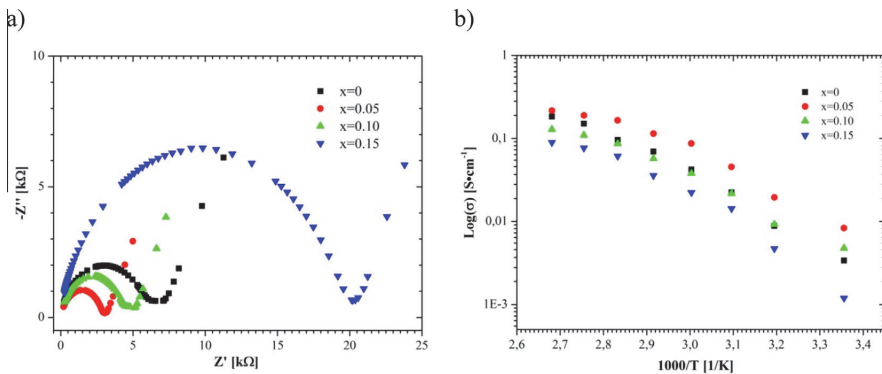


Fig. 3. In a) impedance measurements on $\text{Sm}_{1-x}\text{Ca}_x\text{F}_{3-x}$ ($0 \leq x \leq 0.15$) at RT are shown, in b) ionic conductivities from RT to 100 °C are represented.

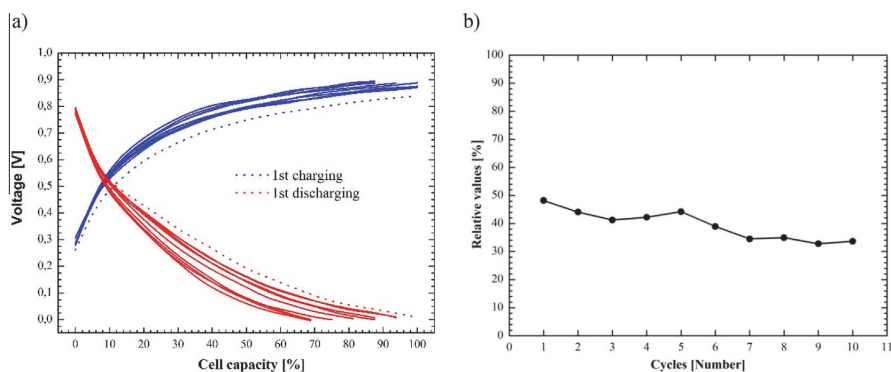


Fig. 4. (a) shows charge/discharge profiles of the CeF_3/Bi -cell (1st–10th cycle from inside to outside) at 75 °C. In (b) the behavior of related coulombic efficiency for 10 cycles is depicted.

milling stabilizes the tysonite structure promoting an increase of crystallite size and provides a consistent parameter change dependent on the doping content. Related property of the pure sample without any Ca^{2+} influence is remarkable and had been reported for altered syntheses [9].

3.2. Morphology studies of $\text{Sm}_{0.95}\text{Ca}_{0.05}\text{F}_{2.95}$

FESEM and HRTEM were applied to investigate the morphology of $\text{Sm}_{0.95}\text{Ca}_{0.05}\text{F}_{2.95}$ illustrated in Fig. 2. From this, an average particle size around 50 nm was extracted. The sample consists of an agglomeration of poly-crystalline nanoparticles as can be seen from the electron microscopes images [26]. From EDX element analysis we were able to confirm the stoichiometry within an error of 0.01.

3.3. EIS investigations

Electrochemical impedance studies were applied to determine the ionic conductivities at different temperatures from 25 to 100 °C, see Fig. 3a. The spectra consist of a semi-circle at high frequency (MHz), and a straight line at low frequency (Hz), which represents the charging of ionic species at the electrolyte-electrode interface [17,27,28]. The resistance of the system corresponds to the real part of the complex impedance and is determined at the intercept of the measured spectra with the x-axis at low frequency [29]. Ionic conductivities and activation energies were determined the literature [3,9,13] accordingly, see Fig. 3b. The ionic conductivity of fluoride ions is determined for the electrolytes from resistance (R), thickness (t) and pellet surface (A) with the equation: $\sigma = [t/(R \cdot A)]$. From this, for instance, at room temperature, the conductivity of $2.8 \cdot 10^{-5} \text{ S cm}^{-1}$ was estimated. Furthermore, from the temperature dependence of ionic conductivities attributed to an Arrhenius-type of behavior, $\sigma_T = \sigma_0 \cdot \exp(-E_a/(k \cdot T))$, where σ_0 is the ionic conductivity, T the temperature, the ion activation energy E_a can be extracted. Notable, the activation energy increases with x (Table 1). The value of E_a for $\text{Sm}_{0.95}\text{Ca}_{0.05}\text{F}_{2.95}$ seems to be in the range of other tysonite-type structures ($\sim 0.4 \text{ eV}$). With higher x values, the activation energy increased up to 0.53 eV.

It was found that the highest conductivities of $2.8 \cdot 10^{-5} \text{ S cm}^{-1}$ at RT and $5.8 \cdot 10^{-4} \text{ S cm}^{-1}$ at 100 °C were obtained with $x = 0.05$ ($\text{Sm}_{0.95}\text{Ca}_{0.05}\text{F}_{2.95}$). This result is close to that of single crystals and previously reported values [9]. Due to relevant ionic conductivity with straightforward synthesis, it became interesting to test potential usage for solid-state Fluoride Ion Batteries (FIB) [10]. So

far, limited authors reported solid electrolytes such as $\text{La}_{0.9}\text{Ba}_{0.1}\text{F}_{2.9}$ with suitable conductivity of $2.8 \cdot 10^{-4} \text{ S cm}^{-1}$ at 160 °C and voltage stability [19].

3.4. Electrochemical cell testing

Based on the achieved conductivity of $\text{Sm}_{0.95}\text{Ca}_{0.05}\text{F}_{2.95}$ solid-state electrolyte, we have tested an electrochemical cell on well-known electrodes: $\text{CeF}_3/\text{Sm}_{0.95}\text{Ca}_{0.05}\text{F}_{2.95}/\text{Bi}$ (Fig. 4) [30]. Bi was chosen as the cathode material as it exhibits high ionic conductivity for fluoride at RT [11]. Also, CeF_3 showed good reversibility in solid-state FIBs [10,15]. The electrochemical cell in this work was charged/discharged with a current density of $1 \mu\text{A cm}^{-2}$ at 75 °C within a voltage interval of 0.01–0.90 V (theoretical voltage 2.8 V). This range is smaller than reported because we used the electrolyte as separator and additive of the cathode only. The overall coulombic efficiency of the active material was less than 50%, reduces during cycling as the active material itself constantly decreases, see Fig. 4. The practical energy density strongly depends on the active nanomaterial which has to be thoroughly investigated in future.

4. Conclusion

$\text{Sm}_{1-x}\text{Ca}_x\text{F}_{3-x}$ ($0 \leq x \leq 0.15$) solid-state electrolytes were successfully prepared via solid synthesis: high-energy ball-milling, a straight forward powder preparation method without pretreatment seems to be a scalable and flexible option for battery applications especially if compared to single crystal growth or other demanding synthesis methods [9,23,31]. Structural and morphology studies revealed that the materials possess the tysonite type structure with crystallite sizes around 10–20 nm and particle size around 50 nm. At room temperature, fluoride ionic conductivities of these materials were in the range of 10^{-5} – $10^{-6} \text{ S cm}^{-1}$ making them attractive for fluoride shuttle applications. Here, it was shown that the electrolyte might be considered as a candidate for secondary Fluoride Ion Battery applications, considered as a contribution to safety and electrochemical stability, supporting FIBs as a promising alternative as next-generation all-solid-state batteries.

Acknowledgements

Many thanks to the European Social Fund, Estonia Science Foundation (ESF), Tallinn University of Technology for the funding of project MTT68, PUT126, PUT1534 and infrastructural support from

Karlsruhe Institute of Technology (KIT), Karlsruhe Nano Micro Facility (KNMF) and the National Institute of Chemical Physics and Biophysics (KBFI).

Conflicts of interest

There is no conflict of interest.

References

- [1] M. Armand, J.-M. Tarascon, Building better batteries, *Nature* 451 (7179) (2008) 652–657, <https://doi.org/10.1038/451652a>.
- [2] J.M. Tarascon, M. Armand, Issues and challenges facing rechargeable lithium batteries, *Nature* 414 (2001) 359–367, <https://doi.org/10.1038/35104644>.
- [3] M.H. Braga, N.S. Grundish, A.J. Murchison, J.B. Goodenough, Alternative strategy for a safe rechargeable battery, *Energy Environ. Sci.* (2017), <https://doi.org/10.1039/c6ee02888h>.
- [4] L.N.N. Patro, K. Hariharan, Fast fluoride ion conducting materials in solid state ionics: an overview, *Solid State Ion.* 239 (2013) 41–49, <https://doi.org/10.1016/j.ssi.2013.03.009>.
- [5] F. Fujara, D. Kruk, O. Lips, A.F. Privalov, V. Sinitsyn, H. Stork, Fluorine dynamics in LaF₃-type fast ionic conductors – combined results of NMR and conductivity techniques, *Solid State Ion.* 179 (2008) 2350–2357, <https://doi.org/10.1016/j.ssi.2008.10.003>.
- [6] A.F. Aalders, A.F.M. Arts, H.W. de Wijn, The fluorine ionic motion in tysonite-structured solid solutions, *Solid State Ion.* (1985), [https://doi.org/10.1016/0167-2738\(85\)90146-8](https://doi.org/10.1016/0167-2738(85)90146-8).
- [7] C. Rongeat, M.A. Reddy, R. Witter, M. Fichtner, Nanostructured fluorite-type fluorides as electrolytes for fluoride ion batteries, *J. Phys. Chem. C* 117 (2013) 4943–4950, <https://doi.org/10.1021/jp3117825>.
- [8] L. Zhang, M. Anji Reddy, M. Fichtner, Development of tysonite-type fluoride conducting thin film electrolytes for fluoride ion batteries, *Solid State Ion.* 272 (2015) 39–44, <https://doi.org/10.1016/j.ssi.2014.12.010>.
- [9] B. Dieudonné, J. Chable, F. Mauvy, S. Fourcade, E. Durand, E. Lebraud, M. Leblanc, C. Legein, M. Body, V. Maisonneuve, A. Demourgues, Exploring the Sm_{1-x}Ca_xF_{3-x} tysonite solid solution as a solid-state electrolyte: relationships between structural features and F⁻ ionic conductivity, *J. Phys. Chem. C* 119 (2015) 25170–25179, <https://doi.org/10.1021/acs.jpcc.5b05016>.
- [10] M. Anji Reddy, M. Fichtner, Batteries based on fluoride shuttle, *J. Mater. Chem.* 21 (2011) 17059, <https://doi.org/10.1039/c1jm13535j>.
- [11] C. Rongeat, M. Anji Reddy, T. Diemant, R.J. Behm, M. Fichtner, Development of new anode composite materials for fluoride ion batteries, *J. Mater. Chem. A* 2 (48) (2014) 20861–20872, <https://doi.org/10.1039/C4TA02840F>.
- [12] B. Ruprecht, M. Wilkening, S. Steuernagel, P. Heitjans, Anion diffusivity in highly conductive nanocrystalline BaF₂:CaF₂ composites prepared by high-energy ball milling, *J. Mater. Chem.* 18 (2008) 5412–5416, <https://doi.org/10.1039/b811453f>.
- [13] B.P. Sobolev, N.I. Sorokin, N.B. Bolotina, Nonstoichiometric single crystals M_{1-x}R_xF_{2+x} and R_{1-y}M_yF_{3-y} (M [Ca, Sr, Ba; R [Rare Earth Elements) as fluoride-ionic conductive solid electrolytes, in: *Photonic Electron. Prop. Fluoride Mater. Prog. Fluor. Sci. Ser.*, 2016, <https://doi.org/10.1016/B978-0-12-801639-8.00021-0>.
- [14] K.E.D. Wapenaar, J.L. Van Koesveld, J. Schoonman, Conductivity enhancement in fluorite-structured Ba_{1-x}La_xF_{2+x} solid solutions, *Solid State Ion.* 2 (1981) 145–154, [https://doi.org/10.1016/0167-2738\(81\)90172-7](https://doi.org/10.1016/0167-2738(81)90172-7).
- [15] H. Bhatia, D.T. Thieu, A.H. Pohl, V.S.K. Chakravadhanula, M.H. Fawey, C. Kübel, M. Fichtner, Conductivity optimization of tysonite-type La_{1-x}Ba_xF_{3-x} solid electrolytes for advanced fluoride ion battery, *ACS Appl. Mater. Interfaces* 9 (2017) 23707–23715, <https://doi.org/10.1021/acsami.7b04936>.
- [16] B. Dieudonné, J. Chable, M. Body, C. Legein, E. Durand, F. Mauvy, S. Fourcade, M. Leblanc, V. Maisonneuve, A. Demourgues, The key role of the composition and structural features in fluoride ion conductivity in tysonite Ce_{1-x}Sr_xF_{3-x} solid solutions, *Dalt. Trans.* (2017), <https://doi.org/10.1039/c6dt04714a>.
- [17] M. Heise, G. Scholz, A. Düvel, P. Heitjans, E. Kemnitz, Mechanochemical synthesis, structure, and properties of solid solutions of alkaline earth metal fluorides: M_{1-x}Mb_xF₂ (M: Ca, Sr, Ba), *Solid State Sci.* 60 (2016) 65–74, <https://doi.org/10.1016/j.solidstatesciences.2016.08.004>.
- [18] J. Chable, A.G. Martin, A. Bourdin, M. Body, C. Legein, A. Jouanneaux, M.P. Crosnier-Lopez, C. Galven, B. Dieudonné, M. Leblanc, A. Demourgues, V. Maisonneuve, Fluoride solid electrolytes: from microcrystalline to nanostructured tysonite-type La_{0.95}Ba_{0.05}F_{2.95}, *J. Alloys Compd.* 692 (2017) 980–988, <https://doi.org/10.1016/j.jallcom.2016.09.135>.
- [19] C. Rongeat, M. Anji Reddy, R. Witter, M. Fichtner, Solid electrolytes for fluorides ion batteries: ionic conductivity in polycrystalline tysonite-type fluorides, *ACS Appl. Mater. Interfaces.* 6 (2014) 2103–2110, <https://doi.org/10.1021/am4052188>.
- [20] B.P. Sobolev, I.A. Sviridov, V.I. Fadeeva, S.N. Sul'yanov, N.I. Sorokin, Z.I. Zhmurova, I.I. Khodos, A.S. Avilov, M.A. Zaporozhets, Mechanochemical synthesis of nonstoichiometric nanocrystals La_{1-y}Ca_yF_{3-y} with a tysonite structure and nanoceramic materials from CaF₂ and LaF₃ crystals, *Crystallogr. Rep.* 53 (2008) 868–880, <https://doi.org/10.1134/S1063774508050234>.
- [21] P.P. Fedorov, T.M. Turkina, B.P. Sobolev, E. Mariani, M. Svantner, Ionic conductivity in the single crystals of non-stoichiometric fluorite phases M_{1-x}R_xF_{2+x} (M=Ca, Sr, Ba; R=Y, La-Lu), *Solid State Ion.* 6 (1982) 331–335, [https://doi.org/10.1016/0167-2738\(82\)90018-2](https://doi.org/10.1016/0167-2738(82)90018-2).
- [22] N.I. Sorokin, E.A. Krivandina, Z.I. Zhmurova, B.P. Sobolev, M.V. Fominykh, V.V. Fistul, Superionic conductivity of the heterovalent solid solutions R_{1-x}M_xF_{3-x} (R=REE, M=Ca, Ba) with tysonite-type structure, *Phys. Solid State.* 41 (1999) 573–575.
- [23] F. Gschwind, G. Rodriguez-Garcia, D.J.S. Sandbeck, A. Gross, M. Weil, M. Fichtner, N. Hörmann, Fluoride ion batteries: theoretical performance, safety, toxicity, and a combinatorial screening of new electrodes, *J. Fluor. Chem.* 182 (2016) 76–90, <https://doi.org/10.1016/j.jfluchem.2015.12.002>.
- [24] J. Chable, B. Dieudonné, M. Body, C. Legein, M.-P. Crosnier-Lopez, C. Galven, F. Mauvy, E. Durand, S. Fourcade, D. Sheptyakov, M. Leblanc, V. Maisonneuve, A. Demourgues, Fluoride solid electrolytes: investigation of the tysonite-type solid solutions La_{1-x}Ba_xF_{3-x} (x; 0.15), *Dalt. Trans.* 44 (2015) 19625–19635, <https://doi.org/10.1039/C5DT02321A>.
- [25] A. Roos, J. Schoonman, Electronic conductivity in La_{1-x}Ba_xF_{3-x} crystals, *Solid State Ion.* 13 (1984) 205–211, [https://doi.org/10.1016/0167-2738\(84\)90031-6](https://doi.org/10.1016/0167-2738(84)90031-6).
- [26] Mohammed Hammad Fawey, Venkata Sai Kiran Chakravadhanula, Munnangi Anji Reddy, Carine Rongeat, Torsten Scherer, Horst Hahn, Maximilian Fichtner, Christian Kübel, In situ TEM studies of micron-sized all-solid-state fluoride ion batteries: preparation, prospects, and challenges: micron-sized all-solid-state fluoride ion batteries, *Microsc. Res. Tech.* 79 (7) (2016) 615–624, <https://doi.org/10.1002/jemt.22675>.
- [27] W. Puin, S. Rodewald, R. Ramlau, P. Heitjans, J. Maier, Local and overall ionic conductivity in nanocrystalline CaF₂, *Solid State Ion.* 131 (2000) 159–164, [https://doi.org/10.1016/S0167-2738\(00\)00630-5](https://doi.org/10.1016/S0167-2738(00)00630-5).
- [28] J. Portier, J.M. Reau, S. Matar, J.L. Soubeyroux, P. Hagenmuller, Advances on fluorine ion conductors, basic and applied research, *Solid State Ion.* 11 (1983) 83–90, [https://doi.org/10.1016/0167-2738\(83\)90067-X](https://doi.org/10.1016/0167-2738(83)90067-X).
- [29] M.A. Reddy, M. Fichtner, Ionic Conductivity of Nanocrystalline Metal Fluorides, in: *Photonic Electron. Prop. Fluoride Mater. Prog. Fluor. Sci. Ser.*, 2016, pp. 449–463, <https://doi.org/10.1016/B978-0-12-801639-8.00020-9>.
- [30] A. Grenier, A.G. Porras Gutierrez, H. Groult, D. Dambournet, Modified coin cells to evaluate the electrochemical properties of solid-state fluoride-ion batteries at 150 °C, *J. Fluor. Chem.* (2016), <https://doi.org/10.1016/j.jfluchem.2016.09.006>.
- [31] B. Ruprecht, M. Wilkening, A. Feldhoff, S. Steuernagel, P. Heitjans, High anion conductivity in a ternary non-equilibrium phase of BaF₂ and CaF₂ with mixed cations, *Phys. Chem. Chem. Phys.* 11 (2009) 3071–3081, <https://doi.org/10.1039/b905911n>.

Publication III

P. Molaiyan and R. Witter; Crystal phase and surface defect driven synthesis of $\text{Pb}_{1-x}\text{Sn}_x\text{F}_2$ solid solution electrolyte for fluoride ion batteries. *Journal of Electroanalytical Chemistry*. 2019, vol. 845, pp. 154–159.

<https://doi.org/10.1016/j.matlet.2019.02.034> (Reproduced from ref.[127] with permission from Elsevier Publishing Group)



Contents lists available at ScienceDirect

Journal of Electroanalytical Chemistry

journal homepage: www.elsevier.com/locate/jelechem

Crystal phase and surface defect driven synthesis of $\text{Pb}_{1-x}\text{Sn}_x\text{F}_2$ solid solution electrolyte for fluoride ion batteries

Palanivel Molaiyan^a, Raiker Witter^{a,b,c,*}^a School of Information Technologies, Tallinn University of Technology (TUT), Akadeemia tee 15A, 12618 Tallinn, Estonia^b Institute of Nanotechnology, Karlsruhe Institute of Technology (KIT), POB 3640, 76021 Karlsruhe, Germany^c Institute of Quantum Optics, University Ulm, Albert-Einstein-Allee 11, 89081 Ulm, Germany

ARTICLE INFO

Keywords:

Lead fluoride
Solid-state electrolyte
Ball-milling
Ionic conductivity
Fluoride ion battery

ABSTRACT

$\text{Pb}_{1-x}\text{Sn}_x\text{F}_2$ layered fluoride super-ionic conductors have become of increased interest for its potential use for all-solid-state secondary fluoride-ion based batteries. By planetary high-energy ball-milling, we have prepared solid-solutions for different stoichiometries: $x = 0.4\text{--}0.6$. These materials were investigated by X-ray Diffraction (XRD), Electrochemical Impedance Spectroscopy (EIS), Field Emission Scanning Electron Microscope (FESEM), High-Resolution Transmission Electron Microscope (HRTEM) and Nuclear Magnetic Resonance (NMR) from which a dominant γ -phase (β - PbF_2 form) cubic structure with crystal and surface defects have been revealed. Crystallite sizes of around 17 nm were achieved. The ionic conductivity of the materials provided a maximum for $x = 0.45$ reaching a value of $2.5 \cdot 10^{-3} \text{ S cm}^{-1}$ at room temperature, with an activation energy of 0.30 eV. This solid-state fluorite type electrolyte was applied for testing a solid fluoride ion battery assembly consisting of Bi-cathode and CeF_3 -anode.

1. Introduction

Increasing interest in the development of next-generation all-solid-state battery systems [1,2] has been promoted due to improvements of solid electrolytes, which are considered as one of the most critical components [3]. Superionic materials and solid solutions applied as functional materials for various electrochemical devices such as batteries, fuel cells, sensors, and electrochemical displays are extensively investigated and characterized by high ionic conductivity [4,5]. Relevant ionic conductors have been studied for enhanced anionic and cationic dynamics, structural disorder, defects, lattice mismatches, and size effects. Among fluoride shuttle systems, crystalline halide materials with the fluorite crystal structure, such as CaF_2 [6] and PbF_2 [7,8], are found to be a promising class of materials with superionic properties. They are investigated for the rapid and continuous increase of fluoride conductivity dependent on altered synthesis methods [9], such as sintering or annealing [10,11].

Binary and ternary systems based on PbF_2 are of particular interest since they provide high fluoride conductivity in the range $10^{-2}\text{--}10^{-3} \text{ S cm}^{-1}$ above 400 K [12,13]. The ionic conductivity of PbF_2 , for instance, is enhanced by the introduction of aliovalent cations due to the formation of an altered electron density compensated by vacancies and interstitials of an extensive dynamic Frenkel disorder

within the anion sublattice [14]. Compounds like MeSnF_4 (Me = Pb, Ba, Sr) incorporating tin into the lattice structure provided high ionic conductivity at room temperature (RT) [8,15]. The hybridized lone electron pair of Sn^{2+} introduces lattice distortions and further promotes anionic conduction. From PbSnF_4 it is for instance known that it possesses fluoride conductivity in the order of $10^{-3} \text{ S cm}^{-1}$ at RT. This system had been studied related to structure, phase transitions, electrical properties, defect formation, mechanisms of ionic transport and ionic conductivity, etc. [16].

Secondary rechargeable electrochemical systems based on solid electrolytes such as $\text{La}_{1-x}\text{Ba}_x\text{F}_{3-x}$ with suitable ionic conductivity and stability have been developed for fluoride ion based battery (FIB) applications [10]. Nanocrystalline $\text{La}_{0.9}\text{Ba}_{0.1}\text{F}_{2.9}$ was prepared by ball-milling and displayed an ionic conductivity of $2.8 \cdot 10^{-4} \text{ S cm}^{-1}$ at 160 °C, which is still lower than for the single crystal [11]. The best ionic conductivities on single crystals obtained with La, Ce, Nd, and Sm in composition with Ca, Ba and Sr vary around $10^{-3}\text{--}10^{-6} \text{ S cm}^{-1}$ at RT to $10^{-2}\text{--}10^{-3} \text{ S cm}^{-1}$ at $T = 150 \text{ °C}$ ¹⁰. Other approaches report materials as CeF_3 doped with SrF_2 or SmF_3 with CaF_2 , the latter for instance obtained by a high temperature (1000 °C) solid-state synthesis with fluorine gas pretreatment. Ionic conductivities of $\sim 10^{-4} \text{ S cm}^{-1}$ at RT for $\text{Ce}_{0.975}\text{Sr}_{0.025}\text{F}_{2.975}$ and $\text{Sm}_{0.94}\text{Ca}_{0.06}\text{F}_{2.94}$ were obtained [17,18]. Also, the preparation of $\text{Pb}_{1-x}\text{Sn}_x\text{F}_2$ electrolytes requires

* Corresponding author at: School of Information Technologies, Tallinn University of Technology (TUT), Akadeemia tee 15A, 12618 Tallinn, Estonia.
E-mail address: raiker.witter@mail.com (R. Witter).

<https://doi.org/10.1016/j.jelechem.2019.04.063>

Received 15 February 2019; Received in revised form 25 April 2019; Accepted 26 April 2019

Available online 26 April 2019

1572-6657/ © 2019 Elsevier B.V. All rights reserved.

elevated temperature treatment and usage of inactive metal containers filled with inert gas [19,20]. However, for fluoride materials' preparation, a straightforward mechano-chemical milling technique is very attractive [12] which is compared to single crystal growth, wet syntheses and heat-assisted reactions a considerable scalable, flexible and resource saving synthesis method. For the $\text{Sm}_{1-x}\text{Ca}_x\text{F}_{3-x}$ and $\text{Pb}_{1-x}\text{Sn}_x\text{F}_2$ systems, recent studies have shown that the mechano-chemical milling method represents a feasible alternative to achieve applicable fluoride conductivities at RT [12].

In this work, we report that the synthesis of $\text{Pb}_{1-x}\text{Sn}_x\text{F}_2$ ($x = 0.4\text{--}0.6$) solid solutions by RT mechano-chemical high-energy ball-milling without prior processing of initial materials, mainly drives the crystal structure into the $\gamma\text{-Pb}_{1-x}\text{Sn}_x\text{F}_2$ cubic ($\beta\text{-PbF}_2$ form) structure. Prepared electrolytes were analyzed with X-ray Diffraction (XRD), Electrochemical Impedance Spectroscopy (EIS), Field Emission Scanning Electron Microscopy (FESEM), High-Resolution Transmission Electron Microscopy (HRTEM) and Nuclear Magnetic Resonance (NMR). The synthesized materials provided considerable ionic conductivity enhancement attractive for electrochemical testing of fluoride-based electrode materials for fluoride ion shuttle energy storage applications.

2. Materials and methods

2.1. Solid-state electrolyte synthesis

Pure $\alpha\text{-PbF}_2$ powder (99%) and $\beta\text{-SnF}_2$ (REO) anhydrous (99%) were obtained from Alfa Aaser for stoichiometric compositions of $\text{Pb}_{1-x}\text{Sn}_x\text{F}_2$ ($x = 0.40\text{--}0.60$) which was synthesized by high-energy mechano-chemical ball-milling using a planetary high-energy system (Tanchen powder, China). The initial materials were placed into silicon nitride vials (internal volume of 50 ml) with silicon nitride balls of different size and a ball to powder ratio of 18:1 under vacuum conditions. The mechano-chemical reaction was performed for 18 h at a 600 rpm to form nano-powders. The products were not additionally pre- or post-treated.

2.2. Battery assembling and testing

For electrochemical testing, composite electrodes were prepared: for the cathode preparation, 40% Bi-metal powder, 10% carbon black (99.0%, Alfa Aaser), 10% polyvinylidene fluoride (PVDF, 99.0%, Alfa Aaser) and 40% solid-state electrolyte $\text{Pb}_{0.55}\text{Sn}_{0.45}\text{F}_2$ were mixed and ball-milled for 3 h at 300 rpm, using zirconia containers with zirconia balls under vacuum conditions; similarly, the anode material preparation of 80% CeF_3 , 10% carbon black (99.0%, Alfa Aaser), 10% polyvinylidene fluoride was carried out. All-solid-state fluoride ion battery pellets were fabricated by pressing cathode composite (Bi), solid-state electrolyte ($\text{Pb}_{0.55}\text{Sn}_{0.45}\text{F}_2$) and anode composite (CeF_3) together into 10 mm diameter pellets using a desktop press (Across International, USA) inside an argon-filled glove box. The final $\text{CeF}_3/\text{Pb}_{0.55}\text{Sn}_{0.45}\text{F}_2/\text{Bi}$ pellet was placed and sealed in an airtight CR2032 coin cell case. Constant current cycling was carried out using a Keysight N6705B (DC power analyzer) battery tester at 25 °C. The cell was charged/discharged within a voltage range of 0.01 and 1.5 V with a current density of 1 uA cm^{-2} .

2.3. Structural and morphology characterization

As prepared samples were analyzed by X-ray Diffraction (XRD) using an AXS Bruker D5005 Advance instrument with Cu K α radiation ($\lambda_1=1.54056 \text{ \AA}$, $\lambda_2=1.544390 \text{ \AA}$) with a variable slit. For XRD analysis the Bruker software (DIFFRAC.SUITE™) was applied. Lorentzian-shaped peaks were identified: peak angle positions (2θ) were extracted from which crystal cell parameters were obtained. Applying the Scherer

equation, the average crystallite sizes (D) were estimated, by taking into consideration the FWHMs (full width at half maxima: β), the angle between the surface of the sample and the incident X-ray beam (θ), the shape parameter for spherical crystallites ($K = 0.89$) and the average wavelength of the X-ray source (λ). For the Cu anode, $\lambda_{\text{CuK}\alpha}$ equals to 1.540 \AA (0.154 nm).

The microstructure of the electrolytes was observed by Field Emission Scanning Electron Microscope (FESEM) of a Carl Zeiss Ultra 55 system with an EDX detector for analyzing the material composition and obtaining particle sizes. A FEI probe-corrected Titan G2 80-200 High-Resolution Transmission Electron Microscope (HRTEM) for fast, precise and quantitative materials' characterization had been used by applying a high voltage range from 80 to 200 kV with a maximum achievable resolution of 0.09 nm.

2.4. Electrochemical Impedance Spectroscopy (EIS)

The $\text{Pb}_{1-x}\text{Sn}_x\text{F}_2$ electrolytes were fabricated applying pellet press (Across international) under an air atmosphere with thicknesses around 1 mm with a diameter of 10 mm. The pellets were gold coated on both sides using a sputter coater (JEOL, USA). Such prepared pellets were further investigated by EIS with an Agilent 4192A LF impedance analyzer to obtain the ionic conductivity of the materials. The applied frequency range was 5 Hz to 13 MHz with a voltage amplitude of 10 mV [21,14].

2.5. Nuclear Magnetic Resonance (NMR)

^{19}F Nuclear Magnetic Resonance (NMR) under Magic Angle Spinning (MAS) was used for sample investigations with 1.8 mm stator-system and related rotors which were filled with the material [6]. Experiments were carried out at a Bruker Avance spectrometer, and a home build NMR probe applying 40 kHz MAS at room temperature with a resonance frequency of 338 MHz, transmitter powers of 160 W, corresponding pulse lengths of 1.2/2.4 μs for 90°/180°-pulses applying 1D Hahn-echo and 2D exchange experiments. Spectra were referenced to NaF (aqueous solution).

3. Results and discussion

3.1. XRD and NMR characterization studies

The significant interest in $\text{Pb}_{1-x}\text{Sn}_x\text{F}_2$ and related materials is motivation by their potential application for solid-state batteries. It is known that the electrolyte can exist of different crystal structures, and composition properties strongly dependent on the preparation method and processing parameters [22]. It occurs in several types (α -, β -, γ - and $\gamma\text{-Pb}_{1-x}\text{Sn}_x\text{F}_2$) of the tetragonal, orthorhombic and cubic structure. In this study, the solid-solution was synthesized with x of 0.40, 0.45, 0.50, 0.55 and 0.60 by high-energy milling resulting in a phase mixture dominated by a phase transition into nano-crystalline $\gamma\text{-Pb}_{1-x}\text{Sn}_x\text{F}_2$ cubic ($\beta\text{-PbF}_2$ form) phase. From ^{19}F NMR it was revealed that mostly nano-crystalline and not a mixture of nano-crystalline/amorphous PbF_2 , and SnF_2 had been obtained, see Fig. 2.

XRD patterns of as-prepared $\text{Pb}_{1-x}\text{Sn}_x\text{F}_2$ ($x = 0.40\text{--}0.60$) were recorded which indicate that the samples mostly consist of cubic ($\gamma\text{-PbSnF}_4$, JCPDS: 06-0251) nano-crystalline structure with remaining amount of tetragonal ($\alpha\text{-PbSnF}_4$ like JCPDS:35-1085) contributions [7,8], see Fig. 1. Hence, it can be confirmed that doping PbF_2 with SnF_2 under high-energy ball-milling favors the cubic γ -phase ($\beta\text{-PbF}_2$ form) [12,23,24]. The resulting unit cell volume increases with rising x up to a value of 0.5 as maximum due to the influence of valence shell electron pairs of Sn, repelling one another and promoting fluoride vacancies [15,25]. For higher x , the influence of increasing number of Sn with a smaller atomic radius than Pb, becomes dominant, the volume of the unit cell and nano-particles decreases. Since the content of remaining

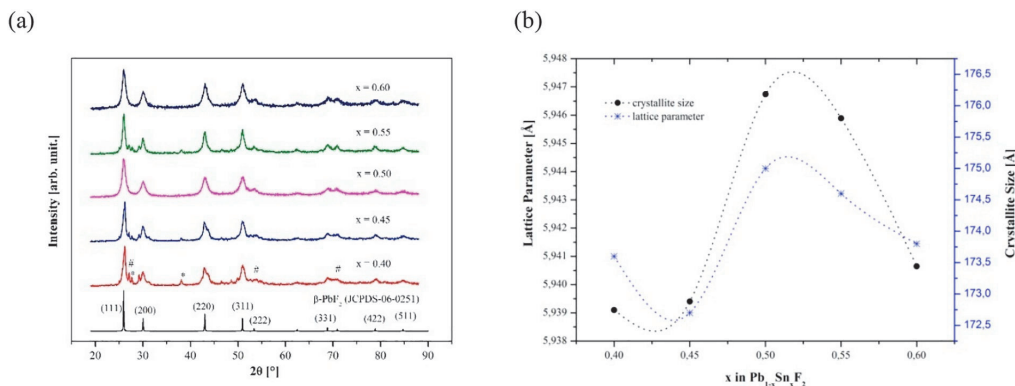


Fig. 1. (a) shows the XRD patterns of $\text{Pb}_{1-x}\text{Sn}_x\text{F}_2$ ($x = 0.40\text{--}0.60$) which indicates that mostly cubic fluorite-type $\gamma\text{-PbSnF}_4$ ($\beta\text{-PbF}_2$ form) like structure has been obtained. Symbols (#) present reflexes from $\alpha\text{-PbSnF}_4$. In (b) the dependency of crystallite size and lattice parameter vs. doping content of the γ -phase cubic structure are represented.

Table 1

Summary of obtained parameters for the synthesized superionic electrolyte $\text{Pb}_{1-x}\text{Sn}_x\text{F}_2$ ($x = 0.40\text{--}0.60$).

Parameters	$\text{Pb}_{1-x}\text{Sn}_x\text{F}_2$				
	$x = 0.40$	$x = 0.45$	$x = 0.50$	$x = 0.55$	$x = 0.60$
Cell Parameters ($\gamma\text{-PbSnF}_4$) (Å)	5.93910	5.93940	5.94674	5.94589	5.94065
Crystallite Size (nm)	17.46	17.27	17.50	17.46	17.38
Ionic Conductivity at RT (S cm^{-1})	$1.08 \cdot 10^{-3}$	$2.53 \cdot 10^{-3}$	$2.42 \cdot 10^{-3}$	$1.84 \cdot 10^{-3}$	$1.23 \cdot 10^{-3}$
Ionic Conductivity at 100 °C (S cm^{-1})	$1.16 \cdot 10^{-2}$	$1.84 \cdot 10^{-2}$	$4.73 \cdot 10^{-3}$	$1.52 \cdot 10^{-2}$	$4.56 \cdot 10^{-3}$
E_a (eV)	0.32 (0.05)	0.30 (0.05)	0.38 (0.04)	0.31 (0.07)	0.42 (0.04)

monoclinic phase is evident, additional crystal deformations induce variations in this considered volume/size dependency. Detailed results are listed in Table 1.

Estimated crystallite sizes were extracted to be roughly around 17 nm, providing a slight size dependency roughly proportional to the unit cell dimension alternation. This proposes an overall consistent crystallite formation of the nano-particles, i.e., the solid syntheses provided a reliable and stable performance for all values of x . From previous work, it has been considered that for $x = 0.5$ the highest conductivity [12] is obtained, despite that we deduce that slight phase mixing related to further unit cell deformations inducing geometry frustration at grain boundaries of different crystallites influence the ionic conductivity that we obtained a maximum value for $x = 0.45$ which is corresponding to the lowest activation energy of 0.3 eV.

From ^{19}F NMR MAS results we can also deduce that mechano-chemical high energy synthesis is driving the system mainly into cubic γ -phase ($\beta\text{-PbF}_2$ form) and introducing defects which naturally have higher surface density and exchanged with the nano-particle core [15,26,27]. This interaction also promotes conductivities at the crystallite and particle boundaries to make ion mobility more accessible at the macroscopic material level, see Fig. 2, which is evident due to achieved low activation energies and high ionic conductivities at RT. Such activation energies had been reported before but attributed to internal fluoride ion mobilities, not accessible to the bulk conductivities [26,24].

3.2. FESEM and HRTEM investigations

FESEM was applied to investigate the morphology of the electrolytes, see Fig. 3a and b, depicted with high-resolution images of 20 and $2 \mu\text{m}$ scale. The powder grain sizes were analyzed and estimated to be 75–100 nm. It also became evident that due to high-energy ball-milling particles perform an agglomeration in the micro-range [27]. The HRTEM of PbF_2 nano-particles are seen in Fig. 3c and d. The dominating β -phase

at (111) directions [28,29] can be observed. Performing EDX element analysis onto the electrolyte ($x = 0.45$), we obtained for lead 55 (2)% and tin 45 (2)%, confirming the purity of the synthesis.

3.3. Electrochemical Impedance Spectroscopy (EIS)

The ionic conductivities of solid electrolytes were investigated by impedance spectroscopy [30,31]. EIS is commonly used to extract the ionic conductivity of a compound by measuring the complex impedance of a device under test between two electrodes, as it has been determined for the electrolytes $\text{Pb}_{1-x}\text{Sn}_x\text{F}_2$ ($x = 0.40\text{--}0.60$) [32], see Fig. 4.

For the $\text{Pb}_{1-x}\text{Sn}_x\text{F}_2$ ($x = 0.40\text{--}0.60$) samples impedance spectra were obtained facilitating a temperature range from 25 to 100 °C, see Fig. 4a. The spectra consist of a semi-circle at high frequency (MHz), representing dependency of the grain boundary region and a straight line at low frequency (Hz), originated from the charging of ionic species at the electrolyte-electrode interface [33]. The physical resistance of the ionic conductor is represented by the real part of the complex impedance as the intercept at x-axis at low frequencies. The ionic conductivity of fluoride ions is determined for the electrolytes from current (I), resistance (R), thickness (t) and pellet surface (A) with the aid of the equation: $\sigma = [(It) / (RA)]$. Furthermore, the temperature dependence of ionic conductivities can be attributed to an Arrhenius-type of behavior: $\sigma_T = \sigma_0 \exp(-E_a / (kT))$, where (σ_0) is the ionic conductivity at an initial temperature, (T) the variable temperature and (E_a) the activation energy [10]. The highest ionic conductivity of $2.5 \cdot 10^{-3} \text{ S cm}^{-1}$ at RT and $1.9 \cdot 10^{-2} \text{ S cm}^{-1}$ at 100 °C with an activation energy of 0.30 eV was obtained for $x = 0.45$. This value is very close to that of single crystals and better than reported results in the literature for fluoride materials. The as-prepared PbSnF_2 like electrolytes synthesized by high-energy ball-milling provided a fluoride ion conductivity equal to that of the electrolytes synthesized using a melting method [34] and activation energies from 0.3 to 0.42 eV were obtained.

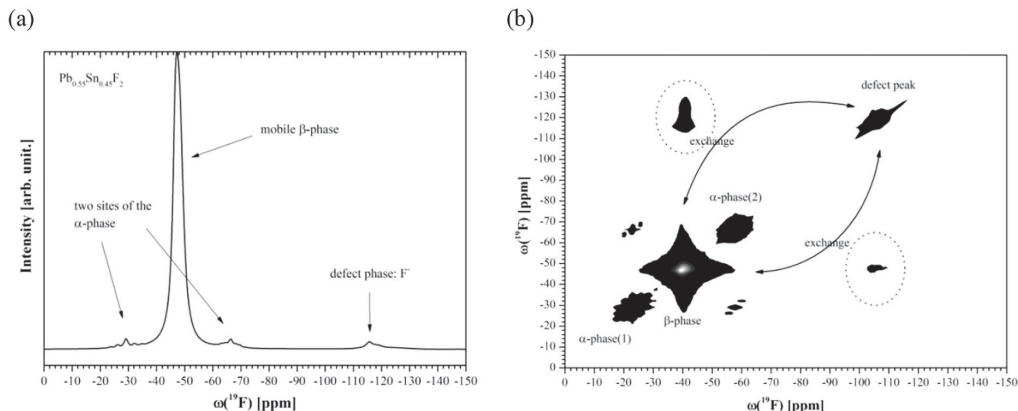


Fig. 2. ^{19}F NMR 1D (a) and 2D exchange (b) spectra are shown. The dominant cubic $\gamma\text{-Pb}_{0.55}\text{Sn}_{0.45}\text{F}_2$ ($\beta\text{-PbF}_2$ form) along remaining α -phase and surface defects are shown. Relevant ion exchange of the defects with the cubic β -form is observed.

3.4. Electrochemical cell testing

The relevant electrolyte conductivity of $\sigma_{RT} = 10^{-3} \text{ S cm}^{-1}$ bears the potential to improve the performance of fluoride ion battery applications [35]. We tested an electrochemical cell which was assembled from a bismuth metal composite cathode and Cerium(III)-fluoride

composite anode [36], and the solid electrolyte $\text{Pb}_{0.55}\text{Sn}_{0.45}\text{F}_2$ as a separator. The open circuit voltage was around 2.0 V. Charging and discharge curves were obtained within a voltage range of 0.01 and 1.3 V. The solid stated electrolyte $\text{Pb}_{0.55}\text{Sn}_{0.45}\text{F}_2$ was stacked between anode and cathode, pressed together to form a three-layer pellet. The obtained cycling behavior and coulomb efficiency are shown in Fig. 5: both, the

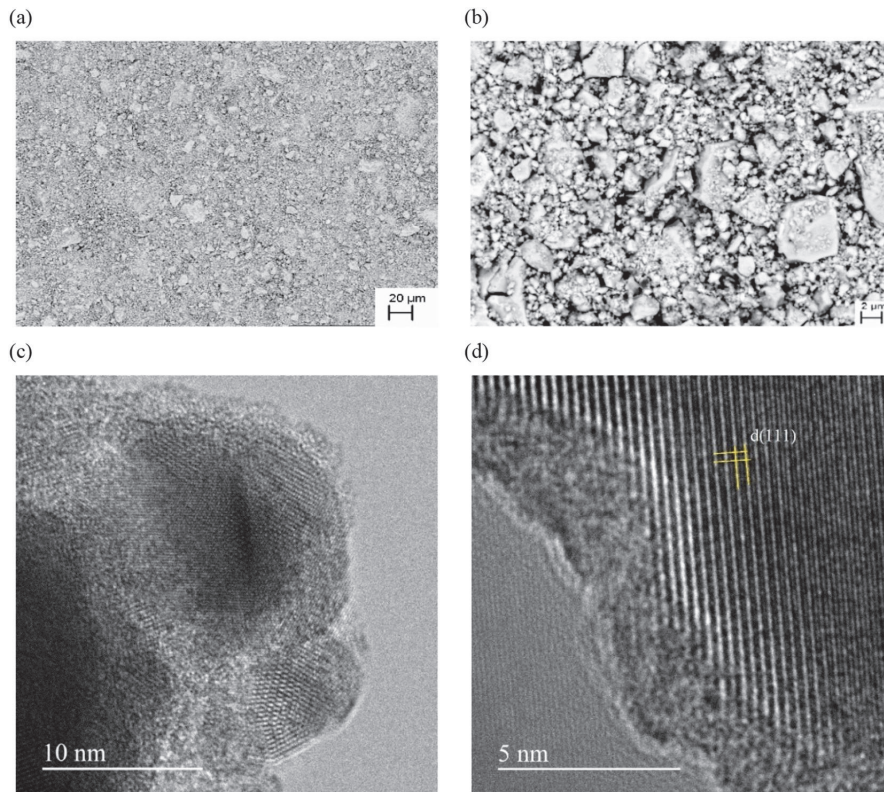


Fig. 3. In (a) and (b) the FESEM morphology of synthesized $\text{Pb}_{0.55}\text{Sn}_{0.45}\text{F}_2$ at different resolutions (20 μm and 2 μm scale) are shown. A significant level of agglomeration due to high-energy ball-milling can be observed. In (c) and (d) HRTEM images are given (10 and 5 nm scale) for a sample of ($x = 0$). PbF_2 nano-particles with the dominating cubic β -phase are visible.

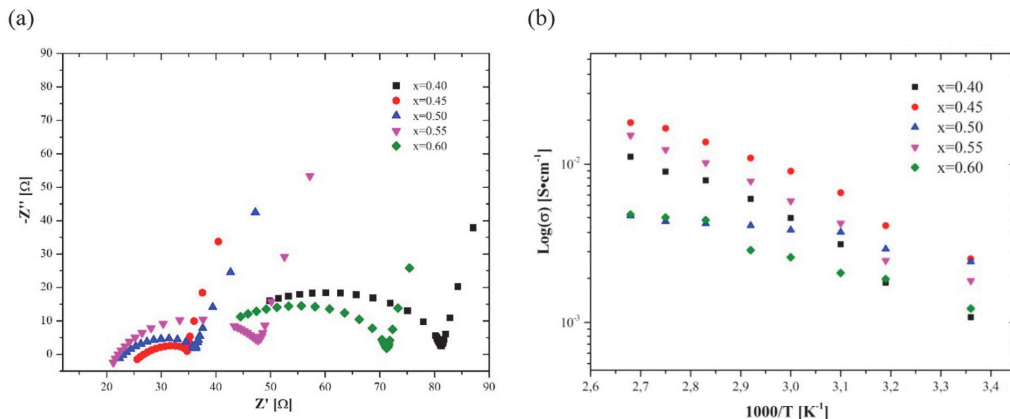


Fig. 4. EIS measurement of $\text{Pb}_{1-x}\text{Sn}_x\text{F}_2$ ($x = 0.40\text{--}0.60$): in (a) the Nyquist plots of the electrolytes at RT are depicted; (b) provides the ionic conductivities of the electrolytes (RT to 100°C) used for fitting the Arrhenius equation.

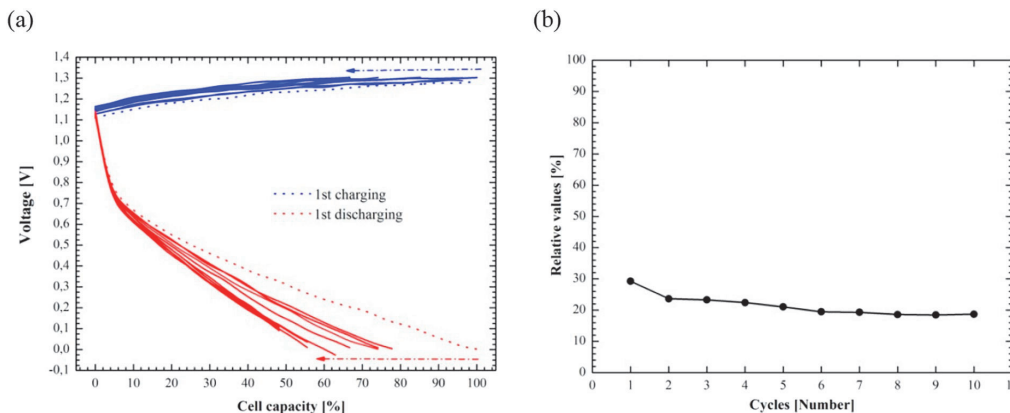


Fig. 5. Electrochemical charge/discharge performance of $\text{Bi}/\text{Pb}_{0.55}\text{Sn}_{0.45}\text{F}_2/\text{CeF}_3$ at RT is shown in a); arrows indicate increasing cycle numbers up to 10. Related coulomb efficiency is depicted in b). Cell capacity is related to the active material.

charge and discharge capacities reduced as the number of cycles increased. The CeF_3 anode composite reacts, and the number of active material decreases from the bismuth metal [37] which results in the formation of reduced active BiF_3 lowering voltage as well as reducing active material. Such issues maybe overcome by using improved composite electrodes of nano-sized active materials and improved conductive additives with stabilization effects.

4. Conclusions

High-energy planetary ball-milling is a robust and useful tool for synthesizing electrolytes for room temperature fluoride superionic conductors. Doping PbF_2 (mostly in α -phase) with β - SnF_2 is stabilizing the electrolytes with reduced crystallite sizes around 17 nm mostly to provide γ - $\text{Pb}_{1-x}\text{Sn}_x\text{F}_2$ ($x = 0.40\text{--}0.60$) cubic phase. Due to the repelling valence shell electron pairs' influence, the smaller atomic radius of Sn and exchanging surface defects – unit cell fluoride vacancies and further deformations due to remaining phase mixing creating additional defects – adding up different contributions, increases the macroscopic conductivity, reaching a maximum for $x = 0.45$ with $2.5 \cdot 10^{-3} \text{ S cm}^{-1}$ at room temperature and $10^{-2} \text{ S cm}^{-1}$ at 100°C . The performance of the electrolyte had been successfully tested for an electrochemical cell assembly of $\text{CeF}_3/\text{Pb}_{0.55}\text{Sn}_{0.45}\text{F}_2/\text{Bi}$ pellet placed and sealed within an

airtight CR2032 coin cell. This even may provide a gateway for recycling lead-based batteries by robust solid synthesis and assembling.

Acknowledgment

Many thanks to the European Social Fund, Estonia Science Foundation (ESF), Tallinna Tehnikaülikool for the funding of project MTT68, PUT126, PUT1534 and infrastructural support from Karlsruhe Institute of Technology (KIT), Karlsruhe Nano Micro Facility (KNMF) and the National Institute of Chemical Physics and Biophysics (KBFI).

References

- [1] L.N.N. Patro, K. Hariharan, Fast fluoride ion conducting materials in solid state ionics: an overview, *Solid State Ionics* 239 (2013) 41–49, <https://doi.org/10.1016/j.ssi.2013.03.009>.
- [2] M. Anji Reddy, M. Fichtner, Batteries based on fluoride shuttle, *J. Mater. Chem.* 21 (43) (2011) 17059, <https://doi.org/10.1039/c1jm13535j>.
- [3] J.M. Tarascon, M. Armand, Issues and challenges facing rechargeable lithium batteries, *Nature* 414 (6861) (2001) 359–367, <https://doi.org/10.1038/35104644>.
- [4] J. Portier, J.M. Reau, S. Matar, J.L. Soubeyroux, P. Hagenmuller, Advances on fluorine ion conductors, basic and applied research, *Solid State Ionics* 11 (1) (1983) 83–90, [https://doi.org/10.1016/0167-2738\(83\)90067-X](https://doi.org/10.1016/0167-2738(83)90067-X).
- [5] N. Kamaya, K. Homma, Y. Yamakawa, M. Hirayama, R. Kanno, M. Yonemura, T. Kamiyama, Y. Kato, S. Hama, K. Kawamoto, et al., A lithium superionic conductor, *Nat. Mater.* 10 (9) (2011) 682–686, <https://doi.org/10.1038/nmat3066>.

- [6] R. Witter, M. Roming, C. Feldmann, A.S. Ulrich, Multilayered core-shell structure of polyol-stabilized calcium fluoride nanoparticles characterized by NMR, *J. Colloid Interface Sci.* 390 (1) (2013) 250–257, <https://doi.org/10.1016/j.jcis.2012.09.001>.
- [7] M. Castiglione, P.A. Madden, P. Berastegui, S. Hull, The crystal structure of α - PbSnF_4 and its anion diffusion mechanism, *J. Phys. Condens. Matter* (2005), <https://doi.org/10.1088/0953-8984/17/6/006>.
- [8] F. Fujisaki, K. Mori, M. Yonemura, Y. Ishikawa, T. Kamiyama, T. Otomo, E. Matsubara, T. Fukunaga, Mechanical synthesis and structural properties of the fast fluoride-ion conductor PbSnF_4 , *J. Solid State Chem.* (2017), <https://doi.org/10.1016/j.jssc.2017.06.007>.
- [9] P. Molaiyan, R. Witter, Mechanochemical synthesis of solid-state electrolyte $\text{Sm}_{1-x}\text{Ca}_x\text{F}_{3-x}$ for batteries and other electrochemical devices, *Mater. Lett.* 244 (2019) 22–26, <https://doi.org/10.1016/j.matlet.2019.02.034>.
- [10] C. Rongeat, M. Anji Reddy, R. Witter, M. Fichtner, Solid electrolytes for fluoride ion batteries: ionic conductivity in polycrystalline tysonite-type fluorides, *ACS Appl. Mater. Interfaces* 6 (3) (2014) 2103–2110, <https://doi.org/10.1021/am4052188>.
- [11] C. Rongeat, M.A. Reddy, R. Witter, M. Fichtner, Nanostructured fluorite-type fluorides as electrolytes for fluoride ion batteries, *J. Phys. Chem. C* 117 (10) (2013) 4943–4950, <https://doi.org/10.1021/jp3117825>.
- [12] M. Uno, M. Onitsuka, Y. Ito, S. Yoshikado, Synthesis and evaluation of $\text{Pb}_{1-x}\text{Sn}_x\text{F}_2$ by mechanical milling, *Solid State Ionics*, 2005, <https://doi.org/10.1016/j.ssi.2005.06.028>.
- [13] S. Yoshikado, Y. Ito, J.M. Réau, Fluoride ion conduction in $\text{Pb}_{1-x}\text{Sn}_x\text{F}_2$ solid solution system, *Solid State Ionics* (2002), [https://doi.org/10.1016/S0167-2738\(02\)00489-7](https://doi.org/10.1016/S0167-2738(02)00489-7).
- [14] Molaiyan, P.; Witter, R. Surface defect enhanced conductivity of calcium fluoride for electrochemical applications. *Mater. Des. Process. Commun.* 0 (ja), e44. doi:<https://doi.org/10.1002/mdp.244>.
- [15] G. Dénès, G. Milova, M.C. Madamba, M. Perfliev, Structure and ionic transport of PbSnF_4 superionic conductor, *Solid State Ionics* (1996), [https://doi.org/10.1016/0167-2738\(96\)00094-X](https://doi.org/10.1016/0167-2738(96)00094-X).
- [16] F. Gschwind, G. Rodriguez-Garcia, D.J.S. Sandbeck, A. Gross, M. Weil, M. Fichtner, N. Hörmann, Fluoride ion batteries: theoretical performance, safety, toxicity, and a combinatorial screening of new electrodes, *J. Fluor. Chem.* (2016) 76–90, <https://doi.org/10.1016/j.jfluchem.2015.12.002>.
- [17] B. Dieudonné, J. Chable, M. Body, C. Legein, E. Durand, F. Mauvy, S. Fourcade, M. Leblanc, V. Maisonneuve, A. Demourges, The key role of the composition and structural features in fluoride ion conductivity in tysonite $\text{Ce}_{1-x}\text{Sr}_x\text{F}_{3-x}$ solid solutions, *Dalton Trans.* (2017), <https://doi.org/10.1039/c6dt04714a>.
- [18] B. Dieudonné, J. Chable, F. Mauvy, S. Fourcade, E. Durand, E. Lebraud, M. Leblanc, C. Legein, M. Body, V. Maisonneuve, et al., Exploring the $\text{Sm}_{1-x}\text{Ca}_x\text{F}_{3-x}$ tysonite solid solution as a solid-state electrolyte: relationships between structural features and F⁻ ionic conductivity, *J. Phys. Chem. C* 119 (45) (2015) 25170–25179, <https://doi.org/10.1021/acs.jpcc.5b05016>.
- [19] N.I. Sorokin, P.P. Fedorov, O.K. Nikol'skaya, O.A. Nikeeva, E.G. Rakov, E.I. Ardashnikova, Electrical properties of PbSnF_4 materials prepared by different methods, *Inorg. Mater.* (2001), <https://doi.org/10.1023/A:1012509528574>.
- [20] M.M. Ahmad, K. Yamada, T. Okuda, Conductivity spectra and comparative scaling studies of polycrystalline PbSnF_4 , *Solid State Ionics* (2004), <https://doi.org/10.1016/j.ssi.2003.09.002>.
- [21] M. Heise, G. Scholz, A. Düvel, P. Heitjans, E. Kemnitz, Mechanochemical synthesis, structure and properties of lead containing alkaline earth metal fluoride solid solutions $\text{M}_x\text{Pb}_{1-x}\text{F}_2$ (M = Ca, Sr, Ba), *Solid State Sci.* (2018), <https://doi.org/10.1016/J.SOLIDSTATESCIENCES.2018.01.007>.
- [22] G. Denes, D. Le Roux, M.M. Cecilia Madamba Juanita Parris, A. Salau, Understanding the phase transitions and texture in superionic PbSnF_4 the key to reproducible properties, *Int. J. Inorg. Mater.* (1999), [https://doi.org/10.1016/S1466-6049\(99\)00030-6](https://doi.org/10.1016/S1466-6049(99)00030-6).
- [23] S.F. Matar, J. Galy, Lone electron pair (E) role on the crystal structures and the mechanism of high ionic conductivity of PbSnF_4E_2 . Stereochemical and ab initio investigations, *Solid State Sci.* (2016), <https://doi.org/10.1016/j.solidstateciences.2015.11.011>.
- [24] M. Murakami, Y. Morita, M. Mizuno, $^{19}\text{F}/^{119}\text{Sn}/^{207}\text{Pb}$ NMR studies on ion dynamics in tetragonal PbSnF_4 : spectroscopic evidence for defect-driven conductivity, *J. Phys. Chem. C* (2017), <https://doi.org/10.1021/acs.jpcc.6b13053>.
- [25] F. Preishuber-Pflügl, M. Wilkening, Mechanochemically synthesized fluorides: local structures and ion transport, *Dalton Trans.* (2016), <https://doi.org/10.1039/c6dt00944a>.
- [26] E. Murray, D.F. Brougham, J. Stankovic, I. Abrahams, Conductivity and fluoride ion dynamics in α - PbSnF_4 : ^{19}F field-cycling NMR and diffraction studies, *J. Phys. Chem. C* (2008), <https://doi.org/10.1021/jp7108708>.
- [27] V.Y. Kavun, A.I. Ryabov, I.A. Telin, A.B. Podgorbunskii, S.L. Sinebryukhov, S.V. Gnednikov, V.K. Goncharuk, NMR and impedance spectroscopy data on the ionic mobility and conductivity in PbSnF_4 doped with alkali metal fluoride, *J. Struct. Chem.* (2012), <https://doi.org/10.1134/S0022476612020126>.
- [28] A. Sakuda, A. Hayashi, M. Tatsumisago, Sulfide solid electrolyte with favorable mechanical property for all-solid-state lithium battery, *Sci. Rep.* (2013), <https://doi.org/10.1038/srep02261>.
- [29] M. Hammad Fawey, V.S.K. Chakravadhanula, M.A. Reddy, C. Rongeat, T. Scherer, H. Hahn, M. Fichtner, C. Kübel, In situ TEM studies of micron-sized all-solid-state fluoride ion batteries: preparation, prospects, and challenges, *Microsc. Res. Tech.* (2016), <https://doi.org/10.1002/jemt.22675>.
- [30] M.M. Ahmad, Y. Yamane, K. Yamada, The ionic conductivity and dielectric properties of $\text{Ba}_{1-x}\text{Sn}_x\text{F}_2$ solid solutions prepared by mechanochemical milling, *Mater. Sci. Eng., B* (2013), <https://doi.org/10.1016/j.mseb.2013.05.011>.
- [31] P. Hagenmuller, J.M. Réau, C. Lucat, S. Matar, G. Villeneuve, Ionic conductivity of fluorite-type fluorides, *Solid State Ionics* (1981), [https://doi.org/10.1016/0167-2738\(81\)90110-7](https://doi.org/10.1016/0167-2738(81)90110-7).
- [32] A. Hayashi, K. Noi, A. Sakuda, M. Tatsumisago, Superionic glass-ceramic electrolytes for room-temperature rechargeable sodium batteries, *Nat. Commun.* 3 (2012) 856, <https://doi.org/10.1038/ncomms1843>.
- [33] W. Puin, S. Rodewald, R. Ramlau, P. Heitjans, J. Maier, Local and overall ionic conductivity in nanocrystalline CaF_2 , *Solid State Ionics* 131 (1) (2000) 159–164, [https://doi.org/10.1016/S0167-2738\(00\)00630-5](https://doi.org/10.1016/S0167-2738(00)00630-5).
- [34] P.A. Popov, Sidorov, Kul'chenkov, Anishchenko, I.C. Avetissov, N.I. Sorokin, P.P. Fedorov, Thermal conductivity and expansion of PbF_2 single crystals, *Ionics* (Kiel) 23 (1) (2017) 233–239, <https://doi.org/10.1007/s11581-016-1802-2>.
- [35] M.M. Ahmad, K. Yamada, T. Okuda, Fluoride ion diffusion of superionic PbSnF_4 studied by nuclear magnetic resonance and impedance spectroscopy, *J. Phys. Condens. Matter* (2002), <https://doi.org/10.1088/0953-8984/14/30/312>.
- [36] C. Rongeat, M. Anji Reddy, T. Diamant, R.J. Behm, M. Fichtner, Development of new anode composite materials for fluoride ion batteries, *J. Mater. Chem. A* 2 (48) (2014) 20861–20872, <https://doi.org/10.1039/C4TA02840F>.
- [37] A. Grenier, A.G. Porras Gutiérrez, H. Groult, D. Dambournet, Modified coin cells to evaluate the electrochemical properties of solid-state fluoride-ion batteries at 150 °C, *J. Fluor. Chem.* (2016), <https://doi.org/10.1016/j.jfluchem.2016.09.006>.

Curriculum vitae

Personal data

Name: Palanivel Molaiyan
Date of birth: 01.02.1987
Place of birth: Tamilnadu, India
Citizenship: Indian

Contact data

E-mail: palaniii_phys87@yahoo.in

Education

2014–2019 Tallinn University of Technology, Faculty of Science, Doctoral Study
2008–2010 PSG College of Technology, India - M.Sc. Materials Science
2005–2008 Sri Vasavi College, India - B.Sc. Physics

Language competence

Tamil Mother Tongue
English Very Good

Professional employment

2013–2014 Junior Researcher, Tallinn University of Technology, Tallinn, Estonia.
Technical and Applications, Hind High Vacuum Co Pvt LTD, Bangalore,
2010–2013 India

Award and Grant

- 1 Indian Government Agency Grant for M.Sc. Student project award: Tamilnadu State Council of Science and Technology (TNSCST)
- 2 Dora Plus (Short-term student mobility grant) - Kristjan Jaak scholarship for short study visits for the conference
- 3 Dora Plus 1.2 (long-term student mobility grant)- for visiting researcher at Lancaster University UK.

Elulookirjeldus

Isikuandmed

Nimi: Palanivel Molaiyan
Sünniaeg: 01.02.1987
Sünnikoht: Tamilnadu, India
Kodakondsus: India

Kontaktandmed

E-post: palanii_phys87@yahoo.in

Hariduskäik

2014–2019 Tallinna Tehnikaülikool, Loodusteaduskond, doktoriõpe
2008–2010 PSG tehnoloogiakolledž, India - M.Sc., materjaliteadus
2005–2008 Sri Vasavi kolledž, India – B.Sc., füüsika

Keelteoskus

Tamiili emakeel
Inglise Väga hea

Teenistuskäik

2013–2014 Nooremteadur, Tallinna Tehnikaülikool, Tallinn, Eesti.
2010–2013 Tehnik, Hind High Vacuum Co Pvt LTD, Bangalore, India.

Teaduspreemiad ja tunnustused

- 1 India valitsusasutuse Grant M.Sc. Student projekti auhinnale: Tamil naduteadus- ja tehnoloogia nõukogu (TNSCST)
- 2 Dora Plus (Lühiajaline üliõpilaste liikuvuse toetus) – Kristjan Jaagu stipendium lühikestele õpivisiitidele konverentsile
- 3 Dora Plus 1,2 (pikaajaline üliõpilaste liikuvuse toetus) – Lancasteri ülikooli küllastamiseks Ühendkuningriigis.

Original publications

- I **P. Molaiyan** and R. Witter; Surface defect-enhanced conductivity of calcium fluoride for electrochemical applications. *Material Design & Processing Communications*. 2019, vol. 1, Issue no. 4, August 2019. e44, <https://doi.org/10.1002/mdp2.44>.
- II **P. Molaiyan** and R. Witter; Mechanochemical synthesis of solid-state electrolyte $\text{Sm}_{1-x}\text{Ca}_x\text{F}_{3-x}$ for batteries and other electrochemical devices. *Materials Letters*. 2019, vol. 244, pp. 22–26, <https://doi.org/10.1016/j.jelechem.2019.04.063>.
- III **P. Molaiyan** and R. Witter; Crystal phase and surface defect driven synthesis of $\text{Pb}_{1-x}\text{Sn}_x\text{F}_2$ solid solution electrolyte for fluoride ion batteries. *Journal of Electroanalytical Chemistry*. 2019, vol. 845, pp. 154–159, <https://doi.org/10.1016/j.matlet.2019.02.034>.
- IV **P. Molaiyan** and R. Witter; CaF_2 Solid-State Electrolytes Prepared by Vapor Pressure Exposure and Solid Synthesis for Defect and Ionic Conductivity Tuning. *Material Design and Processing Communications*. 2019, e76, <https://doi.org/10.1002/mdp2.76>.